PACIFIC EARTHQUAKE ENGINEERING
RESEARCH CENTER

Experimental and Computational Evaluation of Current and Innovative In-Span Hinge Details in Reinforced Concrete Box-Girder Bridges

Part 2: Post-Test Analysis and Design Recommendations

Matias A. Hube
Khalid M. Mosalam

University of California, Berkeley

PEER 2009/107
DECEMBER 2009

Experimental and Computational Evaluation of Current and Innovative In-Span Hinge Details in Reinforced Concrete Box-Girder Bridges

Part 2: Post-Test Analysis and Design Recommendations

Matias A. Hube
Department of Civil and Environmental Engineering
University of California, Berkeley

Khalid M. Mosalam
Department of Civil and Environmental Engineering
University of California, Berkeley

PEER Report 2009/107
Pacific Earthquake Engineering Research Center
College of Engineering
University of California, Berkeley

December 2009

ABSTRACT

This report focuses on post-test finite element analysis (FEA) of and design recommendations for in-span hinges (ISHs) of reinforced concrete (RC) box-girder bridges when subjected to vertical loads through the bearings. ISHs are disturbed regions due to a complex three-dimensional (3D) stress state caused by the concentrated bearing loads and the possible existence of utility and maintenance openings. The common modeling practice for ISHs is the use of simplified two-dimensional (2D) modeling as short cantilevers, following standard procedures, e.g., those in ACI318. Such simplified analytical and design procedures lead to inefficient detailing because they do not take into account the expected failure modes of ISHs, where punching shear is one of these critical modes. For the post-test analysis, a 3D finite element analysis (FEA) is developed and validated against the results of five tested ISH specimens. This computational model considers the cracking behavior of concrete and the elastic-plastic behavior of the reinforcement. The reinforcing steel is modeled using an embedded reinforcement formulation assuming perfect bond between the concrete and the reinforcement. The concrete material is modeled using the total strain rotating crack method. The reduction of compressive strength due to perpendicular cracking is incorporated in the constitutive model. With the validated FEA, a parametric study is conducted to predict the behavior and the strength of ISHs with different detailing and geometrical characteristics. As a result of this study, detailed design recommendations and guidelines are presented for ISHs in RC box-girder bridges. These recommendations are aimed to obtain optimal designs with less congestion and improved structural behavior. The findings from this study revealed that the strength of the ISH should be estimated from five critical design criteria: (1) sliding shear friction, (2) bending moment, (3) 2D SAT, (4) one-dimensional shear, and (5) punching shear. Additionally, it is concluded that the strength of ISHs is improved most by increasing the amount of diagonal reinforcement of the seat.

ACKNOWLEDGMENTS

This study was made possible by funding from the California Department of Transportation under contract number 59A0508. We would like to thank Craig Whitten, Fadel Alameddine, and Steve Sahs for their technical participation during this research program. Additionally, we would like to thank Jeffrey Kress for guiding the visits at the construction site in San Rafael.

The support of the Pacific Earthquake Engineering Research Center (PEER) in publishing this report is gratefully acknowledged. The authors specifically thank Ms. Janine Hannel, Senior Publications Coordinator, for her editing of the report.

CONTENTS

LIST OF FIGURES

LIST OF TABLES

1 Introduction

This report presents the results of the post-test analysis of and the design recommendations for in-span-hinges (ISHs) of reinforced concrete (RC) box-girder bridges. The report focuses on ISHs of prestressed box-girder bridges when subjected to vertical loads through the bearings. ISHs are used mainly to transmit vertical loads between two adjacent parts of the bridge deck, and are classified as disturbed regions due to a complex three-dimensional (3D) stress state caused by the concentrated bearing loads and the possible existence of utility and maintenance openings. The common modeling practice for ISHs is the use of simplified two-dimensional (2D) modeling as short cantilevers, following standard procedures, e.g., those in ACI318 (ACI 2008; Caltrans 2004). Such simplified analytical and design procedures typically lead to congested reinforcement causing constructability concerns from practical and economical aspects. These inefficient detailing designs do not take into account the expected failure modes of ISHs. From the five tested specimens (Hube and Mosalam 2009), a combination of three failure modes of ISHs were identified: (1) one-dimensional (1D) shear, (2) 2D strut-and-tie (SAT) mechanism, and (3) punching shear.

1.1 MOTIVATION AND OBJECTIVES

The overall study program of ISHs is shown in Figure 1.1. The tasks shown in boxes 1 to 6 were addressed by Hube and Mosalam (2009). These tasks included the survey of California highway bridges, the definition of the prototype ISH to be used in the experimental program, the pre-test finite element analysis (FEA) to design and verify the test setup, the capacity estimation of the specimens using code-based analytical models, and the execution of the experimental program. For the experimental program, five 1/3-scale ISH specimens were tested in two phases. For phase I, two specimens were tested representing the as-built conditions of typical ISHs of RC box-girder bridges in California. Specimen S2 was detailed identical to specimen S1, but it contained utility openings to study the effects of such openings on the behavior and strength of ISHs. Based on the test results of phase I, three additional specimens were designed and tested in phase II. Specimen S3 was designed identical to specimen S2 but had a larger bearing plate to increase the punching shear capacity. Specimens S4 and S5 were designed with low reinforcement ratios aimed towards improving the performance and the constructability of ISHs; specimen S5 was detailed identical to specimen S4, but it contained utility openings.

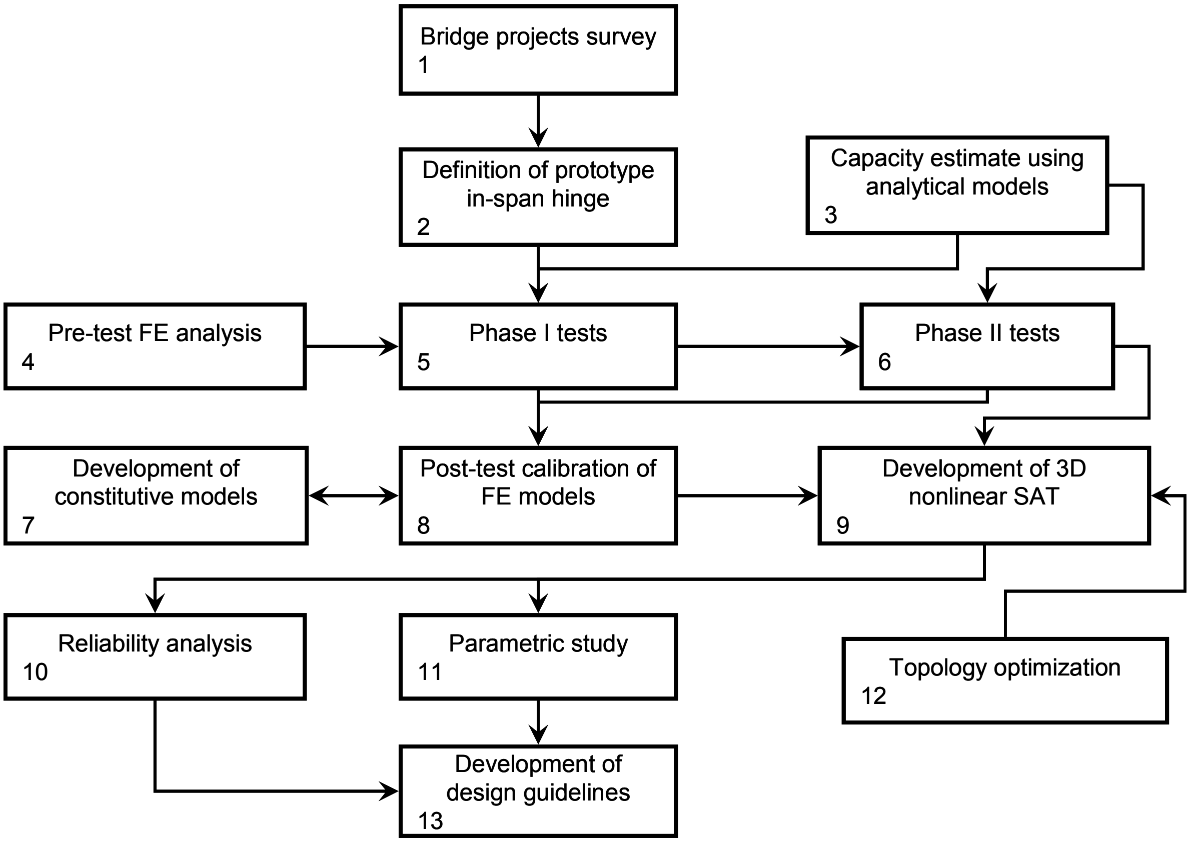

Fig. 1.1 Overview of ISHs study program.

This report focuses on the tasks shown in boxes 8, 11, and 13 of Figure 1.1. Other tasks in boxes 9, 10, and 12 are suggested for future studies on ISHs. The first objective of this report (box 8) is to calibrate the previously developed FE model to predict the behavior and the strength of the tested ISHs. Using this computational model, the second objective of this report (box 11) is to perform a parametric study of ISHs with different detailing and geometrical characteristics. Based on the parametric study and the experimental results, the final objective of this report (box 13) is to develop design recommendations and guidelines for ISHs. These recommendations are aimed to design ISHs with less reinforcing steel congestion, to improve structural behavior of

ISHs, and to provide a means for realistically estimating the strength of ISHs. This recommended strength prediction can be used for the design of new ISHs of RC box-girder bridges and also to evaluate existing ISHs. The characteristics of the ISHs used in this study correspond to configurations of bridges typically constructed in California. However, the final product of the entire study is general enough to be applicable for box-girder bridges in other places in the U.S. and worldwide.

The post-test FEA is conducted using a model validated based on the results of the experimental program. The computational model adopts nonlinear 3D FEA that considers the cracking behavior of concrete and the elastic-plastic behavior of the reinforcement. The nonlinear behavior of the concrete is modeled using the total strain rotating crack model, where the reduction of compressive strength due to perpendicular cracking is incorporated in the constitutive model. The reinforcing steel is modeled using embedded reinforcement formulation, assuming perfect bond between the concrete and the reinforcement, which is an adequate approximation for ISHs (Hube and Mosalam 2009).

The parametric study is intended to expand the findings of the experimental program, by considering these FE simulations as virtual experiments. To conduct the parametric study, a reference ISH is defined with nominal material properties and geometrical configurations commonly used in practice. Using the proposed 3D FEA, the behavior, yield load, strength, and mode of failure of these virtual specimens are compared with the reference ISH and with the tested specimens. The ISH variables analyzed in the parametric study are reinforcement steel ratios and detailing characteristics, size of the bearing area, aspect ratio of the seat, load eccentricity, and geometrical characteristics of the utility openings. The characteristics analyzed for the utility openings are the opening location, the opening size, and the reinforcement detailing near the openings.

Based on the parametric study and the results of the experimental program, design recommendations of the ISH are presented. First, a methodology to estimate the strength of ISHs is presented based on the critical of five modes of failures: (1) sliding shear friction, (2) bending moment, (3) 2D SAT, (4) 1D shear, and (5) punching shear. Subsequently, specific design recommendations for the reinforcement and geometrical detailing of the ISH are provided. Finally, design recommendations for the geometrical characteristics of utility openings and reinforcement detailing near the openings are presented.

1.2 ORGANIZATION OF REPORT

The present chapter, as discussed above, motivates this research project and complements the previously published first part of this study (Hube and Mosalam 2009). Chapter 2 describes the concrete behavior under tensile and compressive stress states, and how this behavior is incorporated in the FEA of RC using the total strain crack model. Additionally, Chapter 2 describes the effect of loading conditions and concrete material properties on the predicted behavior of ISHs.

The post-test FEA of the five tested specimens is described in Chapter 3. The predicted load versus displacement relationships, the damage propagation, and the reinforcement behavior are compared with the experimental findings reported in Hube and Mosalam (2009).

Chapter 4 describes the parametric study of ISHs using the proposed FEA. The reference ISH for the parametric study is defined and the behavior and strength of ISHs with varying detailing and geometrical characteristics are compared to the reference ISH.

Chapter 5 summarizes the design recommendations for ISHs, where the procedure to estimate the strength of the ISH is described. Specifically, reinforcement and geometric detailing recommendations are described in this chapter.

The conclusions of this research project are presented in Chapter 6. An outline of the proposed future research activities is also presented in this chapter.

Finally, Appendix A contains the detailed capacity estimates for the different modes of failure of the virtual specimens from the FEA. These virtual specimens are used in the parametric study.

2 Modeling of Reinforced Concrete in Finite Element Analysis

ISHs are subjected to complex 3D loading conditions due to the discrete bearing locations, the small aspect ratio of the seat, and the geometrical discontinuities when utility openings exist. Therefore, evaluation of existing ISHs and development of design requirements can be improved with 3D FEA that takes into account compatibility, equilibrium, and the constitutive relationships of concrete and steel.

The 3D modeling of RC using FEA was described in Hube and Mosalam (2009). The concrete is modeled using a standard FE displacement formulation with 8-node isoparametric brick elements. The nonlinear material behavior of the concrete is modeled with the total strain crack constitutive model. The reinforcing steel is introduced in the FEA using the embedded reinforcement formulation, which implies perfect bond between the steel and the concrete.

This chapter describes the tensile and the compressive behavior of concrete, and how to incorporate this behavior into the total strain crack model. The chapter concludes with a discussion of the effects of different concrete material parameters on the FEA prediction.

2.1 CONCRETE TENSILE BEHAVIOR

The tensile behavior of concrete is primarily controlled by the formation of micro-cracks (Evans and Marathe 1968; Reinhardt 1984; Rots et al. 1985). If the tensile stress reaches a certain tensile limit, the additional deformation will localize within a region called the fracture process zone. After the tensile limit is reached, the stress in the fracture process zone decreases as the strain increases, and unloading occurs in the uncracked concrete material located outside the fracture process zone. The tensile stress at the fracture process zone is resisted through bridging of aggregates at the micro-crack surface and through friction. When the stress reaches zero, a macro crack is formed in the fracture process zone. The phenomenon described in this paragraph is known as tension softening.

To describe the fracture process, two approaches are commonly used in fracture mechanics of quasi-brittle materials, e.g., concrete (Bažant and Planas 1998). The first approach, known as the cohesive crack model, assumes that the entire fracture process zone is localized in a discrete crack (Hillerborg et at. 1976). The fracture process inherent to this crack is modeled using a stress crack-width relationship, as shown in Figure 2.1a. To model this relationship, several authors have proposed tension-softening curves. Hillerborg et al. (1976) proposed a linear tension-softening curve, Peterson (1981) proposed a bi-linear curve, Cho et al. (1984) proposed a tri-linear curve, and Gopalaratnam and Shah (1985) and Cornelissen et al. (1986) proposed different exponential curves. The second approach to describe the fracture process, known as the crack band or smeared crack model, assumes that the inelastic deformation of the fracture process zone is distributed over a certain band width h (Bažant and Oh 1983, Rots et al. 1985), as shown in Figure 2.1b.

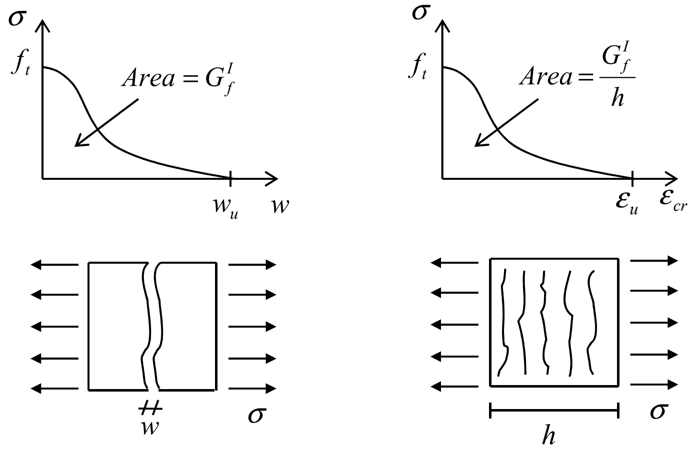

(a) Cohesive crack model (b) Smeared crack model

Fig. 2.1 Cohesive and smeared crack models.

In FEA, the tensile behavior of concrete is commonly incorporated using the smeared crack model. To produce results independent of the mesh size, i.e., objective solution, the stress-strain softening curve must be adjusted according to the element size (Bažant and Planas 1998; Maekawa et al. 2003). This property is known as mesh objectivity and is satisfied with the incorporation of the fracture energy in the constitutive model. The fracture energy G_f^I is assumed to be a material property and is defined as the amount of energy required to produce a crack of unit area (Hillerborg 1985). However, tests conducted by Zhao et al. (2008) have demonstrated that the value of the fracture energy increases with the specimen's size. From the stress-displacement relationship, the fracture energy is defined as (see the cohesive crack model in Figure 2.1a, where w_u is the smallest stress-free crack width)

$$G_f^I = \int_0^{w_u} \sigma \, dw \tag{2.1}$$

If a uniform crack strain ε_{cr} is assumed within the crack band width h in the smeared crack model, the crack width can be obtained as follows:

$$w = \varepsilon_{cr} h \tag{2.2}$$

Therefore, the tension-softening curves obtained for the cohesive crack model can be transformed into stress-strain relationships to be used in the smeared crack model noticing that

$$\int_0^{\varepsilon_u} \sigma \, d\varepsilon_{cr} = \frac{G_f^I}{h} \tag{2.3}$$

where ε_u is the smallest stress-free crack strain (see the smeared crack model in Fig. 2.1b).

The fracture energy is a material property that can be obtained experimentally following the recommendations of Rilem (1985). In the absence of test data, the CEB-FIP model code (Comité 1990) suggests a fracture energy value given by

$$G_f^I = \alpha \, f_{ck}^{0.7} \quad [\mathrm{J/m2}\,] \tag{2.4}$$

where f_{ck} is the characteristic strength [MPa], and α=4, 6, and 10 for maximum aggregate sizes of 8, 16, and 32 mm, respectively.

For the crack band width h, there is no consensus on the value that should be used in FEA. Its magnitude depends on the element size, element type, element geometry, crack orientation, amount of cracking, aggregate size, presence of reinforcement, crack inclination relative to reinforcing bar direction (if any), the integration scheme, and the particular problem considered (Rots et al. 1985; Bažant and Oh 1983; Mosalam and Paulino 1997; Maekawa et al. 2003). For 2D problems, Rots et al. (1985) suggested crack band width values depending on the strain distribution and crack orientation. For uniform strain and cracks parallel to the mesh, they recommended a crack band width as $h = \sqrt{A_e}$ where A_e is the area of the finite element. This crack band width is also recommended by Maekawa et al. (2003) for 2D problems of plain concrete. Bažant and Oh (1983) pointed out that the crack band width can be approximately identified from fracture tests of concrete specimens with different geometry, in which the cracking is localized to a different extent. Based on experimental results, Bažant and Oh (1983) concluded that a crack band width between two and five times the maximum aggregate size was adequate. Finally, Mosalam and Paulino (1997) suggested an evolutionary method that varies the crack band width during the FEA.

For the case of RC, the tensile behavior and fracture mechanism of concrete is different from that of plain concrete. For RC, the tensile strength of concrete is mainly resisted by bond stress transfer from the reinforcing bar, referred to as tension stiffening (Maekawa et al. 2003; Yankelevsky et al. 2008). Tension stiffening occurs mostly when a concrete crack is normal to the reinforcement due to the bond effect, whereas tension stiffening is negligible for a concrete crack parallel to the reinforcement. . Therefore, a crack in an arbitrary orientation with respect to the reinforcing bars, e.g., in densely RC structure such as the as-built ISH diaphragms, shows a combined stiffening/softening behavior (Maekawa et al. 2003). This combined behavior is incorporated by Maekawa et al. (1997) to obtain a tensile stress-strain relationship of RC in 3D. For each orthogonal direction in the 3D stress domain, a stress-strain curve and a normalized fracture energy ($G_f^* = G_f^I / f_t h$) are obtained. For a stress direction parallel to the reinforcement, i.e., cracks perpendicular to the reinforcement, a tension-stiffening curve independent of the element size is considered. For a stress direction perpendicular to the reinforcement, i.e., crack parallel to the reinforcement, a tension-softening curve based on the fracture energy and the element size (crack band width) is considered. From the normalized fracture energy of each direction, the 3D normalized fracture energy is obtained by interpolation, considering the angle between the concrete crack and each of the orthogonal directions. Finally, this interpolated fracture energy is used to obtain a stress-strain curve normal to the crack direction.

The negative modulus of the softening stress-strain curve can produce snap-back behavior when conducting FEA (Koeberl and William 1998; DIANA 2008). This snap-back behavior should be avoided for numerical stability in the FEA. When cracking is localized in one element of length $L = h + h_c$, the incremental elongation of a concrete member is composed of the elongation of the cracked region h and the elastic contraction of the uncracked region h_c, as shown in Figure 2.2. In some cases, the reduction of the stress $\Delta\sigma$ due to the localized cracking can produce a decrease in the total deformation of the element, referred to as a snap-back. The incremental strain for a reduction of stress $\Delta\sigma < 0$ is

$$\Delta\varepsilon = \frac{\Delta L}{L} = \frac{\Delta\sigma}{L}\left(\frac{h}{E_o} + \frac{h_c}{E_c}\right) = \Delta\sigma\left(\frac{1}{E_c} + \frac{h}{L}\left(\frac{1}{E_o} - \frac{1}{E_c}\right)\right) \tag{2.5}$$

where E_c is the elastic modulus of the uncracked concrete and E_o is the modulus of the cracked region, which is negative and assumed constant in the above formula, i.e., linear softening upon cracking. In this case, the required condition to obtain a positive strain is

$$\frac{1}{E_c} + \frac{h}{L}\left(\frac{1}{E_o} - \frac{1}{E_c}\right) < 0 \tag{2.6}$$

which can be written as

$$E_c > -E_o\left(\frac{L}{h} - 1\right) > 0 \tag{2.7}$$

For the special case of $L = 2h$, the required condition to prevent snap-back behavior becomes $E_c > -E_o$, which agrees with Koeberl and William (1998). For the particular case of linear tension softening,

$$E_o = -\frac{f_t^2 h}{2G_f^I} \tag{2.8}$$

Finally, the condition to prevent snap-back can be written as

$$G_f^I > \frac{f_t^2 (L-h)}{2E_c} \tag{2.9}$$

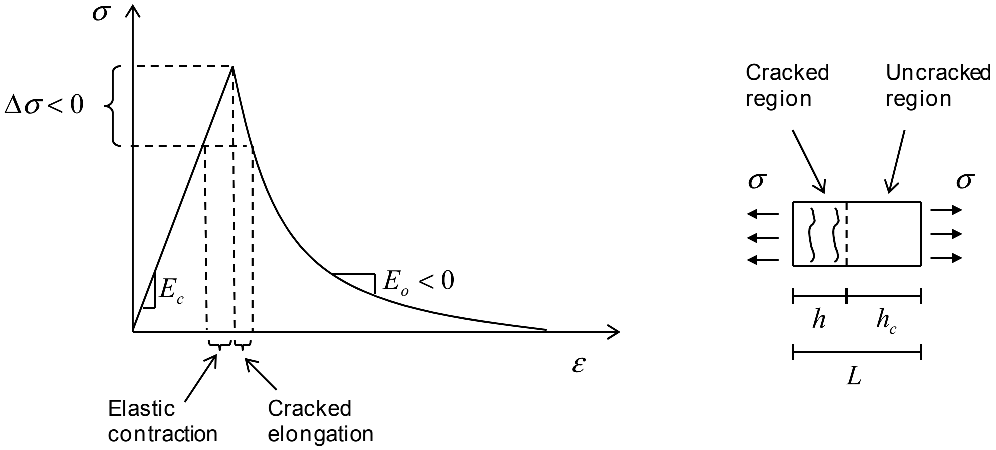

Fig. 2.2 Snap-back condition.

2.2 CONCRETE COMPRESSIVE BEHAVIOR

The uniaxial compressive behavior of concrete is measured by a standard compression test on a standard cylinder. The uniaxial stress-strain response is essentially linear elastic up to about 30% of the uniaxial strength f_c'. Above this level, nonlinearity is observed. When concrete is loaded beyond the compressive strength f_c', the uniaxial stress-strain curve exhibits strain softening, which is characterized by a descending branch.

When concrete is subjected to biaxial or triaxial loading, the compressive behavior, the strength, and the ductility vary significantly. When cracked concrete in tension is subjected to compression parallel to the crack direction, the compressive strength and stiffness are reduced (Vecchio and Collins 1993; Belarbi and Hsu 1991); whereas when concrete is subjected to biaxial or triaxial compressive stresses, the compressive strength increases due to the effect of confinement (Richart et al. 1928; Kupfer et al. 1969; Mills and Zimmerman 1970). For the case of ISH diaphragms, the concrete is subjected to a multiaxial state of stresses. Therefore, the multiaxial concrete behavior has to be incorporated in the constitutive model when conducting FEA of these disturbed regions.

2.2.1 Compression Softening

In cracked concrete, tensile strains perpendicular to the principal compressive direction reduces the compressive strength (Vecchio and Collins 1993). This reduction of strength is known as compression softening. The analytical models of compression softening typically consider a reduction factor β_σ that modifies the compressive strength, and another reduction factor β_ε that modifies the strain at peak strength ε_o, as shown in Figure 2.3. Based on tests of concrete panels subjected to biaxial stresses, several authors proposed expressions for these reduction factors (Shirai and Noguchi 1989; Belarbi and Hsu 1991; Vecchio and Collins 1993).

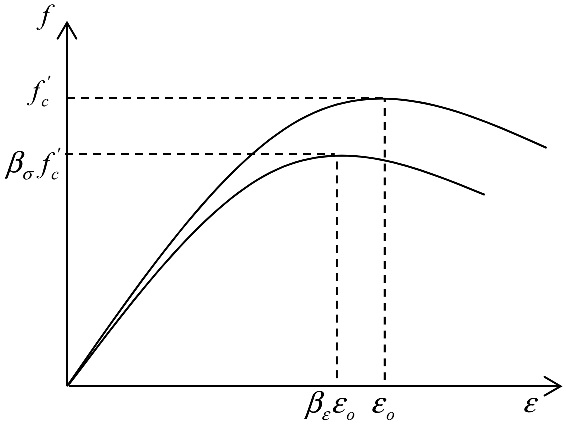

Fig. 2.3 Compression softening.

From the tests of 2D panels, Vecchio and Collins (1993) proposed a strain reduction factor $\beta_\varepsilon = 1$ and a strength reduction factor $\beta = \beta_\sigma$ given by

$$\beta = \frac{1}{1 + 0.27\left(\dfrac{\varepsilon_{lat}}{\varepsilon_o} - 0.37\right)} \leq 1 \tag{2.10}$$

This strength reduction factor is shown in Figure 2.4. The quotient $\varepsilon_{lat} / \varepsilon_o$ in Eq. 2.10 is a positive number, where ε_{lat} is the tensile strain in the lateral direction and ε_o is the compressive strain at peak strength (see Fig. 2.3). This reduction factor can be extrapolated to the 3D case (DIANA 2008) if the lateral strain ε_{lat} is computed as an average strain given by

$$\varepsilon_{lat} = \sqrt{\varepsilon_{l1}^2 + \varepsilon_{l2}^2} \tag{2.11}$$

where ε_{l1} and ε_{l2} represent the tensile strains in the principal lateral directions. To model the cyclic behavior of concrete, the value of ε_{lat} can be considered based on the maximum tensile strain achieved during the cyclic loading history in each principal lateral direction (DIANA 2008).

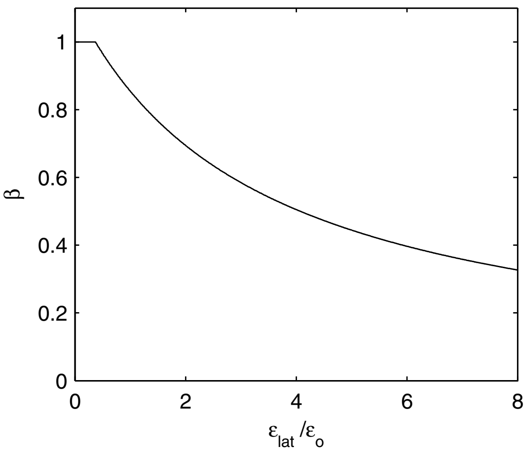

Fig. 2.4 Strength reduction factor β for compression softening (Vecchio and Collins 1993).

2.2.2 Effect of Confinement

When concrete is subjected to biaxial or triaxial loading conditions, the compressive strength and the post-peak behavior can vary significantly (Richart et al. 1928; Kupfer et al. 1969; Mills and Zimmerman 1970). From experimental results, Kupfer et al. (1969) concluded that the strength of concrete under biaxial compression was 16% larger than that under uniaxial compression. From triaxial compression test with constant lateral pressure $\sigma_2 = \sigma_3$ conducted by Richart et al. (1928), the suggested longitudinal stress at failure was observed to be

$$\sigma_1 = f_c' + 4.1\sigma_3 \tag{2.12}$$

To model the effect of multiaxial stresses on concrete strength, several authors proposed failure surfaces (Ottosen 1977; Gerstle 1981; Hsieh et al. 1982). Gerstle (1981) proposed an octahedral representation of the multiaxial stress-strain relationship for concrete, assuming isotropic and nonlinear behavior. Hsieh et al. (1982) proposed a stress-strain relationship with a failure surface defined by four parameters given by

$$A\frac{J_2}{\left(f_c'\right)^2} + B\frac{\sqrt{J_2}}{f_c'} + C\frac{\sigma_1}{f_c'} + D\frac{I_1}{f_c'} - 1 = 0 \tag{2.13}$$

where f_c' is the characteristic uniaxial compressive strength and σ_1 the maximum principal stress, with a positive stress value representing a tensile stress. In Eq. 2.13, I_1 is the first stress invariant and J_2 the second deviatoric stress invariant, which are computed from the principal stresses as follows

$$I_1 = \sigma_1 + \sigma_2 + \sigma_3 \tag{2.14}$$

$$J_2 = \frac{1}{6}\left[(\sigma_1 - \sigma_2)^2 + (\sigma_2 - \sigma_3)^2 + (\sigma_3 - \sigma_1)^2\right] \qquad (2.15)$$

The constants A, B, C, and D in Eq. 2.13 were evaluated to satisfy four failure stress conditions: (1) simple tension with $\sigma_1 = 0.1f_c'$, $\sigma_2 = \sigma_3 = 0$, (2) simple compression with $\sigma_1 = -f_c'$, $\sigma_2 = \sigma_3 = 0$, (3) biaxial compression with $\sigma_1 = \sigma_2 = -1.15f_c'$, $\sigma_3 = 0$, and (4) triaxial compression with $\sigma_1 = \sigma_2 = -0.8f_c'$, $\sigma_3 = -4.2f_c'$. Accordingly, the values of the constant are $A = 2.0108$, $B = 0.9714$, $C = 9.1412$, and $D = 2.2312$ (Hsieh et al. 1982).

2.3 TOTAL STRAIN CRACK MODEL

The total strain crack model was developed along the lines of the 2D modified compression field theory (Vecchio and Collins 1986) and extended to 3D by Selby and Vecchio (1993). To model the stress-strain relationship, two concepts are used: the rotating crack and the fixed crack. The main characteristics of the total strain crack model are described in Hube and Mosalam (2009).

The total strain crack model is used in this study with 8-node isoparametric brick elements using the typical trilinear interpolation (Hughes 2000). The use of enhanced strain formulations (Simo and Rifai 1990), typically available in FE programs, results in unexpected element behavior in nonlinear FEA. For a FE subjected to increasing nodal displacements, the principal strain at one integration point does not necessarily increase. This behavior was detected at some integration points in the pre-test FEA of the ISH specimens, which was conducted using the enhanced strain formulation (default formulation of program DIANA (2008)). This unexpected result agrees with DIANA (2008), which states that the combination of nonlinear materials with the enhanced strain formulation may be unstable for these nonlinear cases.

For the post-test analysis of the ISH specimens, the rotating crack concept is utilized. The fixed crack concept presented convergence problems for small values of the shear retention factor β_s. The shear retention factor is a non-dimensional parameter ($0 \leq \beta_s \leq 1$) that reduces the elastic shear modulus G_c of concrete after cracking to the constant value $\beta_s G_c$. The load-displacement relationships using the fixed crack concept for the bearings of specimen S1 are shown Figure 2.5. The computed responses, using different values of the shear retention factor, are compared to the experimental response (east and west bearings). From Figure 2.5, it is observed that as the value of β_s decreases, the predicted response approaches the experimental response. However, for a value of β_s=0.05 convergence problems occur at about 130 kip (578 kN) of the bearing load, and the model is not able to predict the experimental response anymore.

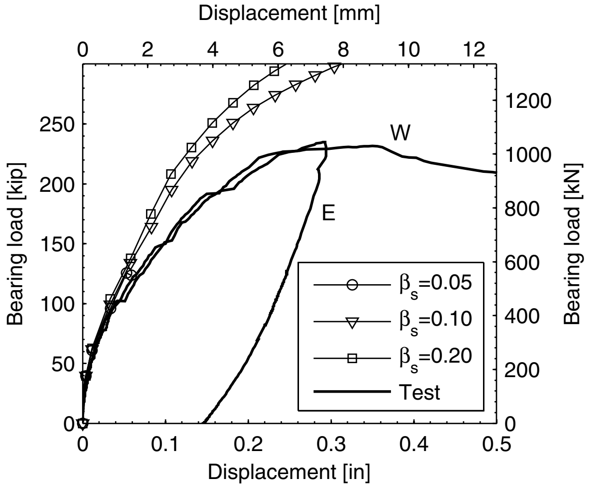

Fig. 2.5 Load-displacement of specimen S1 using fixed crack concept.

2.4 EFFECT OF CONCRETE MATERIAL PARAMETERS

The effects of the concrete material parameters of the total strain rotating crack model are discussed in this section. To study these effects, FEA with different concrete parameters are conducted for specimen S1. The predicted load-displacement relationships at the bearings are compared to the experimental results. On the local level, the predicted stresses of a diagonal bar located near the bearings are also compared to the experimental results. The concrete parameters discussed in this section are (1) the compression softening, (2) the compression confinement, (3) the compressive strength, (4) the tensile strength, (5) the crack band width, and (6) the shape of the tension-softening curve.

For the compressive uniaxial behavior of concrete, an elastic-perfectly plastic behavior is assumed with a modulus of elasticity of 3170 ksi (21.9 GPa) and a compressive strength of 6.3 ksi (43.4 MPa). These values correspond to the properties of concrete measured in the experimental program (Hube and Mosalam 2009). For the uniaxial tensile behavior, a linear tension-softening is considered with a tensile strength of $4\sqrt{f'_c}$=320 psi (2.21 MPa) and a fracture energy of G_f^I=0.32 lbf /in. (56 N/m). These values are consistent with code recommendations (ACI 2008; Comité 1990). The crack band width considered in the models is

$h = \kappa \sqrt[3]{V_e}$ where V_e is the volume of the FE and κ is a calibration parameter chosen as κ=2.0 in. this study.

The constitutive model of the reinforcing steel was obtained from the stress-strain tests conducted on the reinforcing bars and includes strain hardening (Hube and Mosalam 2009). For the steel material, the behavior in tension and compression is assumed identical.

2.4.1 Compression Softening and Confinement

The effects of compression softening and compression confinement are shown in Figure 2.6. The compression softening is incorporated in the FEA using the reduction factor of Eq. 2.10, proposed by Vecchio and Collins (1993). The compression confinement is incorporated using the failure surface of Eq. 2.13, proposed by Hsieh et al. (1982). Accordingly, when concrete is confined, the compressive strength is increased. The curve labeled normal, in Figure 2.6, corresponds to the response that ignores these two effects. When the compression softening is incorporated, it is observed that the load-displacement curve (Fig. 2.6a) reaches a peak strength and then it predicts a descending branch that is parallel to the descending branch observed from the test. It is to be noted that Figure 2.6a shows a negligible effect when the compression confinement is incorporated. This negligible effect is caused by the stress state of the concrete, where most of the concrete is cracked in tension before reaching the unconfined compression strength f_c'. Figure 2.6b shows that the effects of compression softening and compression confinement in the tensile stress of the diagonal bar are negligible for a bearing load lower than 150 kip (667 kN). For higher loads, as expected, the predicted stresses of the reinforcement are higher when compression softening is included.

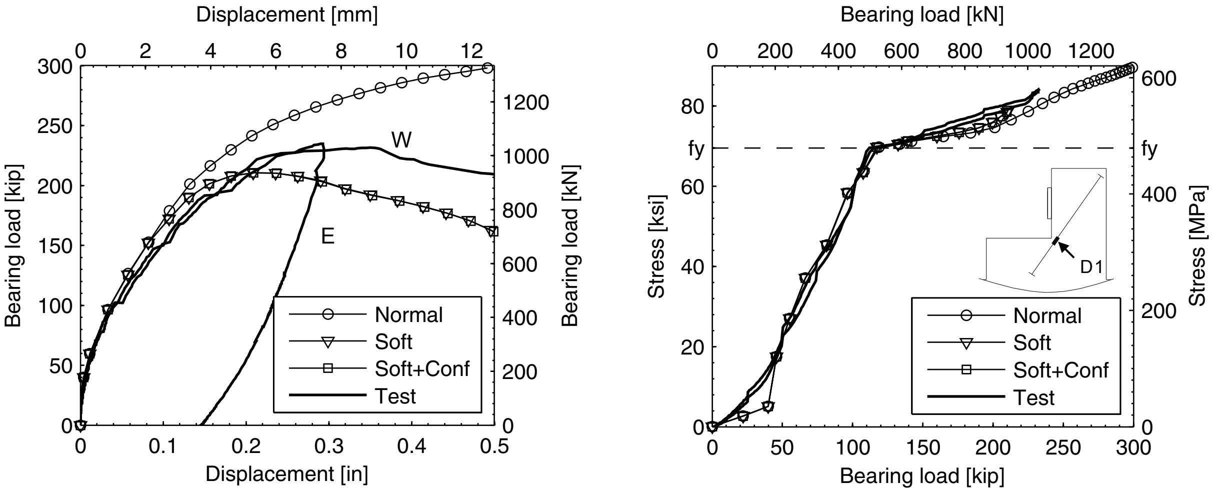

(a) Load-displacement

(b) Stress versus load at diagonal bar D1

Fig. 2.6 Effect of compression softening and compression confinement (east and west bearing shown for test result).

Based on the results of Figure 2.6 it is concluded that compression softening has to be included in the post-test analysis of ISHs. Additionally, it is concluded that the effect of confinement on the compressive strength is not relevant in the modeling of ISHs.

The predicted stress-strain response in a concrete element located at the seat near one of bearings for the case including compression softening is shown in Figure 2.7. This figure shows the stress-strain relationships in the three principal strain directions at an integration point of a FE. The location of the FE and the principal directions are shown in the insert of Figure 2.7. It can be observed that the compression response, principal direction 3, is reduced because of the compression softening, caused by the existence of tensile strains in the principal direction 1. On the other hand, a maximum tensile strain of 0.0084 is determined for the principal direction 2 (direction perpendicular to the insert of Fig. 2.7).

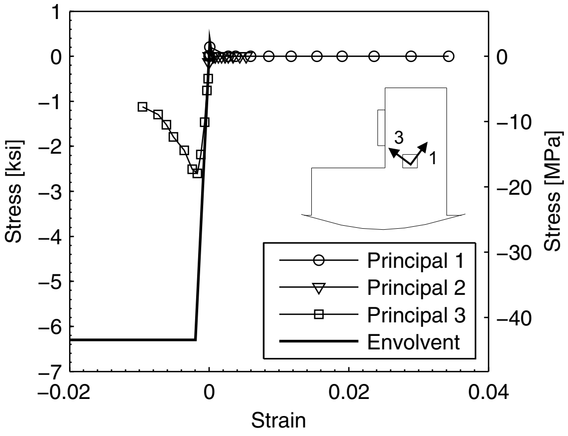

Fig. 2.7 Stress-strain relationships of concrete at an integration point in principal strain directions.

2.4.2 Compressive Strength

The effect of compressive strength of concrete is shown in Figure 2.8. The response is estimated with a compressive strength of 6.3 ksi (43.4 MPa), 6.6 ksi (45.5 MPa), and 7.0 ksi (48.3 MPa). Figure 2.8a shows that the predicted strength of the ISH increases as the compressive strength increases. The increase of the ISH strength corresponds to 3% and 7% for the cases of 6.6 ksi (45.5 MPa) and 7.0 ksi, respectively, compared with the case of 6.3 ksi (43.4 MPa). However, the slopes of the descending branches are similar for the three cases. Figure 2.8b shows that the effect of the compressive strength in the tensile stress of a diagonal bar is negligible.

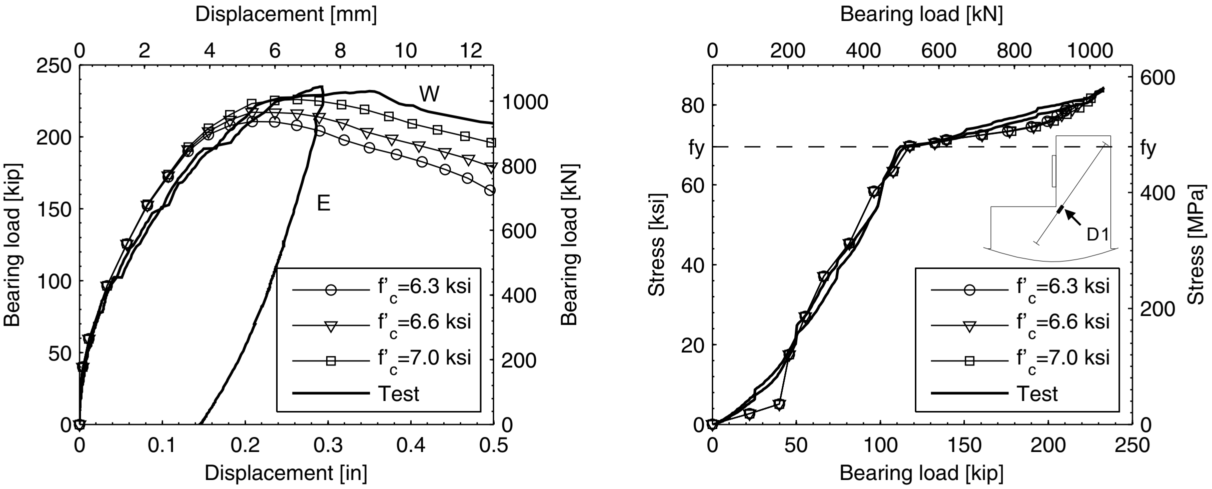

(a) Load-displacement (b) Stress versus load at diagonal bar D1

Fig. 2.8 Effect of compressive strength (east and west bearing shown for test results).

2.4.3 Tensile Strength

The effect of the tensile strength of concrete is shown in Figure 2.9. The response is estimated considering a tensile strength of $2\sqrt{f_c'}$, $4\sqrt{f_c'}$ and $6\sqrt{f_c'}$ (psi units). For specimen S1, these tensile strength values are equivalent to 0.16 ksi (1.1 MPa), 0.32 ksi (2.2 MPa), and 0.48 ksi (3.3 MPa), respectively. Figure 2.9a shows that the load-displacement curve is slightly affected by the tensile strength in the displacement range between 0.5 in. (12.7 mm) and 1.5 in. (38.1 mm). However, the peak strength and the descending branch are not affected by the tensile strength. Figure 2.9b shows that the reinforcement tensile stresses are affected by the tensile strength of concrete at low load levels. As the tensile strength increases, the initiation of cracking and the stress transfer to the reinforcement are delayed. Based on the results of Figure 2.9, it is concluded that a tensile strength of $4\sqrt{f_c'}$ (psi units) is adequate for the post-test analysis of ISHs.

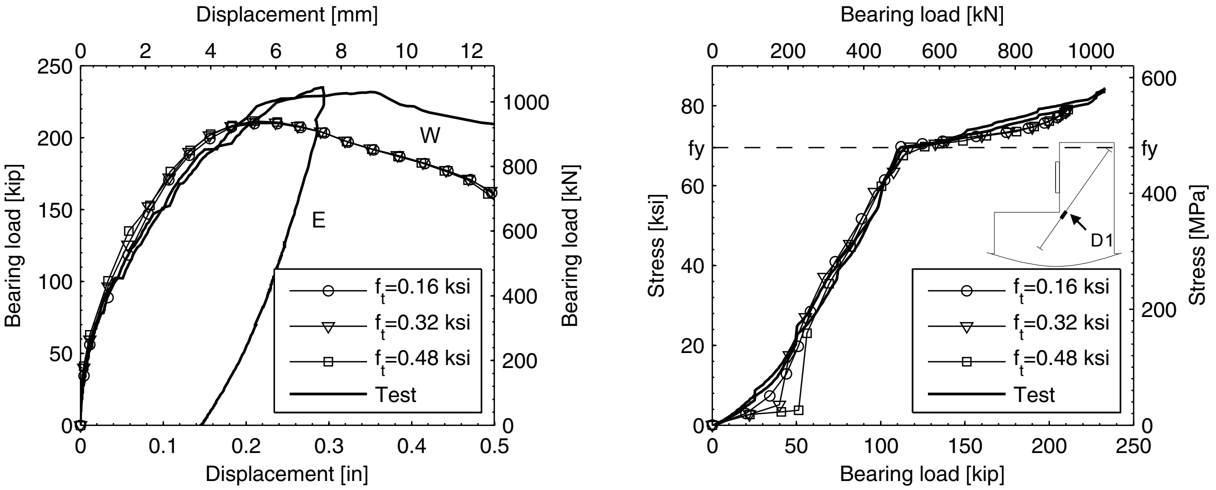

(a) Load-displacement (b) Stress versus load at diagonal bar D1

Fig. 2.9 Effect of tensile strength (east and west bearing shown for test results).

2.4.4 Crack Band Width

The crack band width is considered as $h = \kappa \sqrt[3]{V_e}$ where V_e is the volume of the FE and κ is a non-dimensional calibration parameter. Since the tension-softening relationship of concrete depends on the ratio G_f^I / h, increasing the crack band width h is equivalent to decreasing the fracture energy G_f^I. For the fracture energy, a value of G_f^I=0.32 lbf/in. (56 N/m) is considered, which is consistent with the CEB-FIP (Comité 1990) code. The effect of the crack band width is shown in Figure 2.10, where the response is estimated for κ=2.0, 1.0, and 0.5. Figure 2.10a shows that the predicted load-displacement curve and the peak strength of the ISH decrease as the crack band width increases (or fracture energy decreases). However, the slope of the descending branch is not affected by the crack band width. In contrast, Figure 2.10b shows that the predicted tensile stresses of the diagonal bar increase as the crack band width increases. For the case of κ=0.5, yielding of the reinforcing bar is delayed considerably when compared to the test results.

Based on the results of Figure 2.10, it is concluded that a value of κ=2.0 is adequate to estimate the crack band width in the post-test analysis of the ISHs. If the fracture energy measured for the concrete of specimen S1, i.e., G_f^I=0.60 lbf/in. (105 N/m), and the typical assumption of the crack band width of $h = \sqrt[3]{V_e}$ are considered, this results in an equivalent value of κ=0.53. Based on this parametric study, this latter value is judged to be inadequate to estimate the crack band width of the tested ISHs.

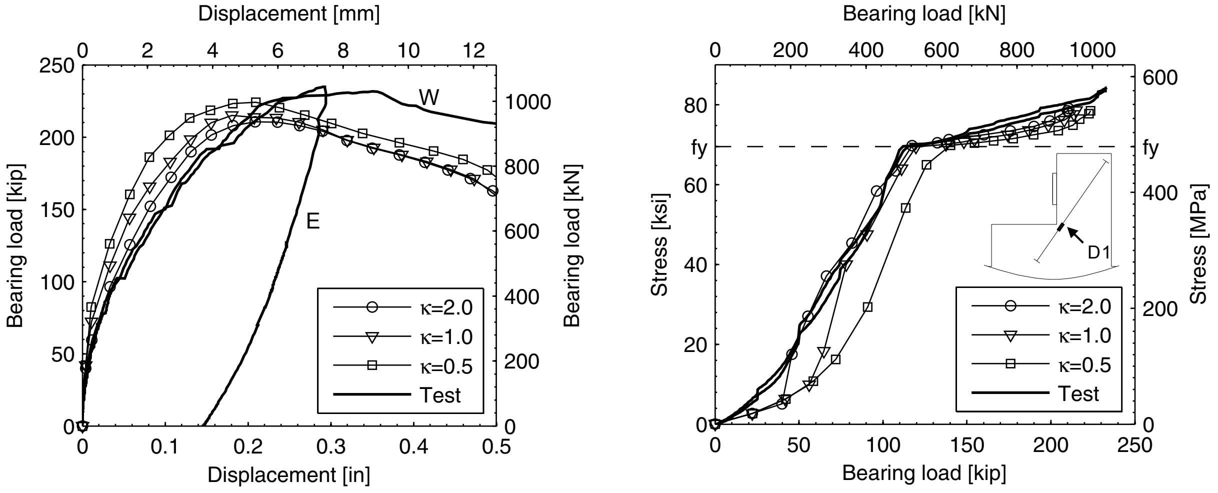

(a) Load-displacement (b) Stress versus load at diagonal bar D1

Fig. 2.10 Effect of crack band width (east and west bearing shown for test results).

2.4.5 Shape of Tension-Softening Curve

The effect of the shape of the tension-softening curve on the ISH response is discussed in this section. The shapes considered are a linear curve (Hillerborg et al. 1976) and two exponential curves (Cornelissen et al. 1986; Gopalaratnam and Shah 1985), shown in Figure 2.11. The stress-strain relationships for the exponential curves are given by

$$\frac{\sigma(\varepsilon_{cr})}{f_t} = \left(1+\left(c_1\frac{\varepsilon_{cr}}{\varepsilon_u}\right)^3\right)exp\left(-c_2\frac{\varepsilon_{cr}}{\varepsilon_u}\right)-\frac{\varepsilon_{cr}}{\varepsilon_u}\left(1+c_1^3\right)exp\left(-c_2\right) \quad \text{(Cornelissen et al. 1986)} \qquad (2.16)$$

$$\frac{\sigma(\varepsilon_{cr})}{f_t} = exp\left(-k\varepsilon_{cr}\right) \qquad \text{(Gopalaratnam and Shah 1985)} \qquad (2.17)$$

where c_1=3, c_2=6.93, and ε_u is the strain at σ=0. The values of ε_u and k are computed such that the area under the curve is equated to G_f^I / h, i.e., $\varepsilon_u = 5.14 G_f^I / f_t h$ and $k = f_t h / G_f^I$. The effect of the shape of the tension-softening curve in the FEA of specimen S1 is shown in Figure 2.12. Based on the results of this figure, it is concluded that the effect of the shape of the tension-softening curve is negligible in predicting the behavior of the ISHs.

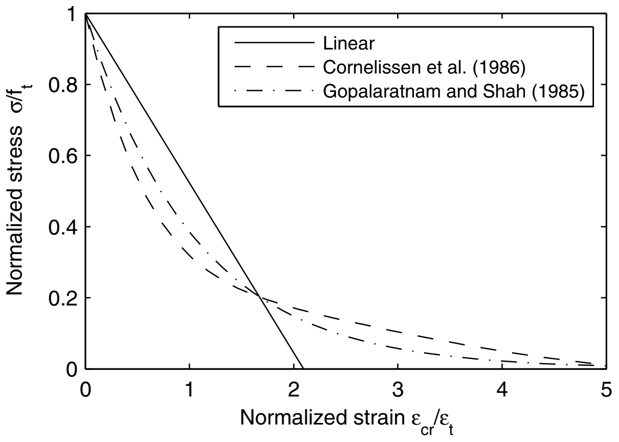

Fig. 2.11 Tension-softening curves.

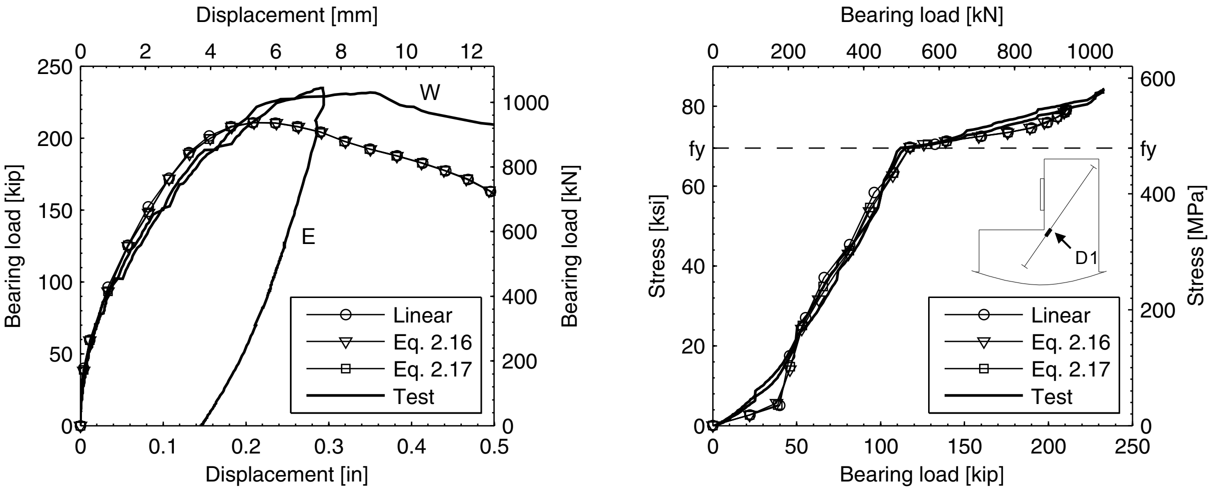

(a) Load-displacement

(b) Stress versus load at diagonal bar D1

Fig. 2.12 Effect of shape of tension-softening curve (east and west bearing shown for test results).

3 Post-Test Finite Element Analysis

This chapter describes the post-test FEA of the five ISH specimens tested in the experimental program (Hube and Mosalam 2009). These analyses were conducted using the general-purpose finite element program DIANA (2008).

3.1 MESH DEVELOPMENT

The five tested specimens (S1–S5) were discretized to match the geometry and the boundary conditions. Because of symmetry, only half of each specimen is considered in the FEA. The models include the ISH region, the concrete base, and one of the steel bearing plates. Specimens S1 and S4 have an identical geometry and are characterized by not having utility openings. The mesh of S1 and S4 was generated using 2505 nodes and 1894 brick elements, as shown in Figure 3.1a. This mesh results in an average element length of 3.2 in. (81 mm). Specimens S2 and S5 have identical geometry and are characterized by having utility openings. The mesh of S2 and S5, shown in Figure 3.1b, has fewer elements than the mesh of S1 due to the presence of these utility openings. The geometry of specimen S3 was identical to S2, but S3 was tested with larger bearing plates. Therefore, the mesh of S3 is identical to S2 but has additional nodes and brick elements to simulate the larger bearing plates. The mesh of specimen S3 is shown in Figure 3.1c.

The boundary conditions of the concrete base are assumed pinned along the three global axes, and the post-tension forces of 120 kip (534 kN) are applied externally at the top of the concrete base at the locations of the anchoring rod. For the rods located at the center of the specimens, half of the post-tension force is applied. The steel bearing plates are modeled with a higher modulus of elasticity (10 times higher than regular steel) to simulate the stiffness provided by the loading swivels that are located adjacent to the loading plates.

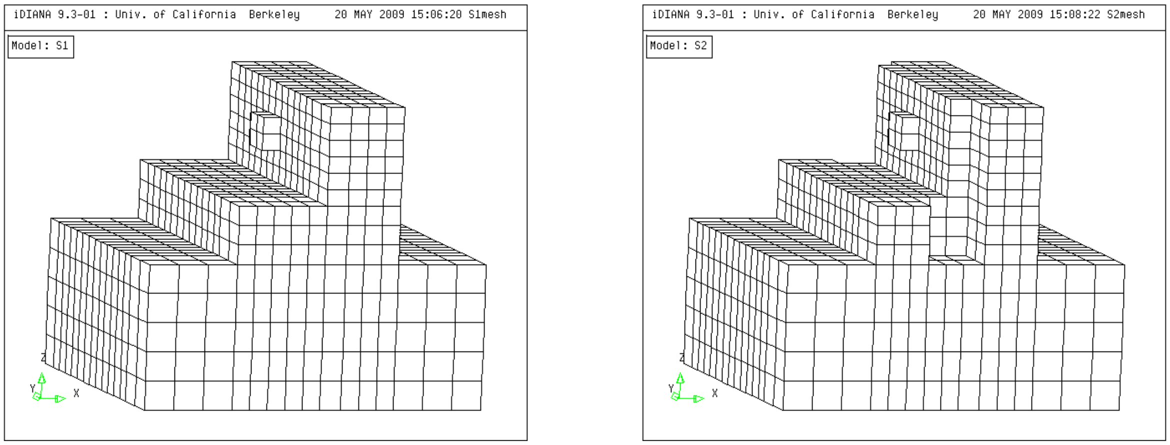

(a) S1 and S4 (b) S2 and S5

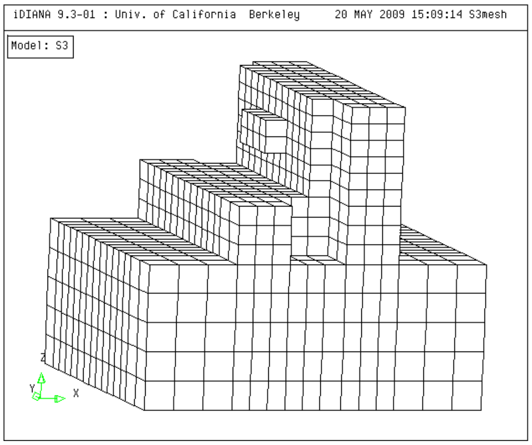

(c) S3

Fig. 3.1 Concrete mesh of tested specimens.

To model the reinforcing steel, an embedded reinforcement formulation is used in the ISH region and in the concrete base, which is an adequate approximation for ISHs (Hube and Mosalam 2009). The location of the reinforced steel was based on the as-built characteristics of the specimens. The embedded reinforcement of specimen S1 is shown in Figure 3.2a–b. This model contains a total of 350 bars located throughout the specimen. The embedded reinforcement of specimen S4, which was designed with lower reinforcement ratio, is shown in Figure 3.2c–d.

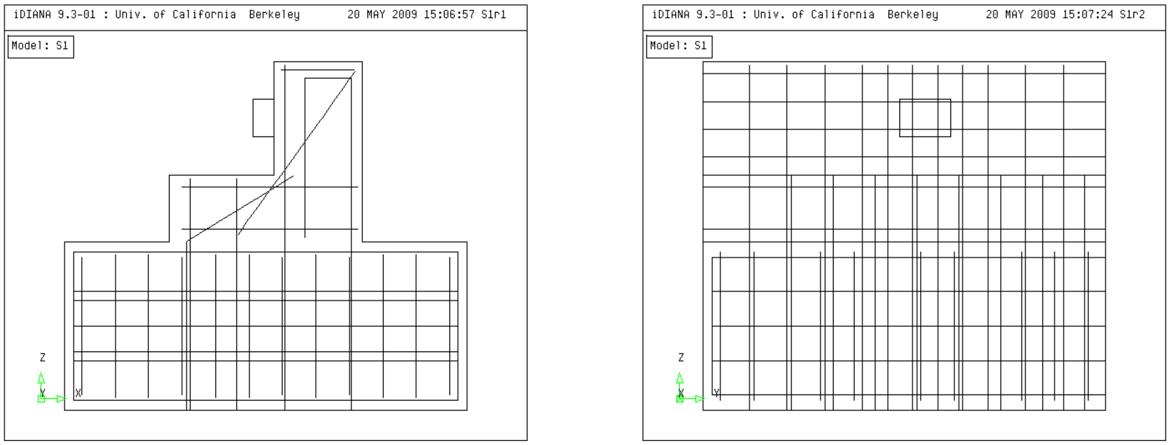

(a) Cross section of S1 (b) Elevation view of S1

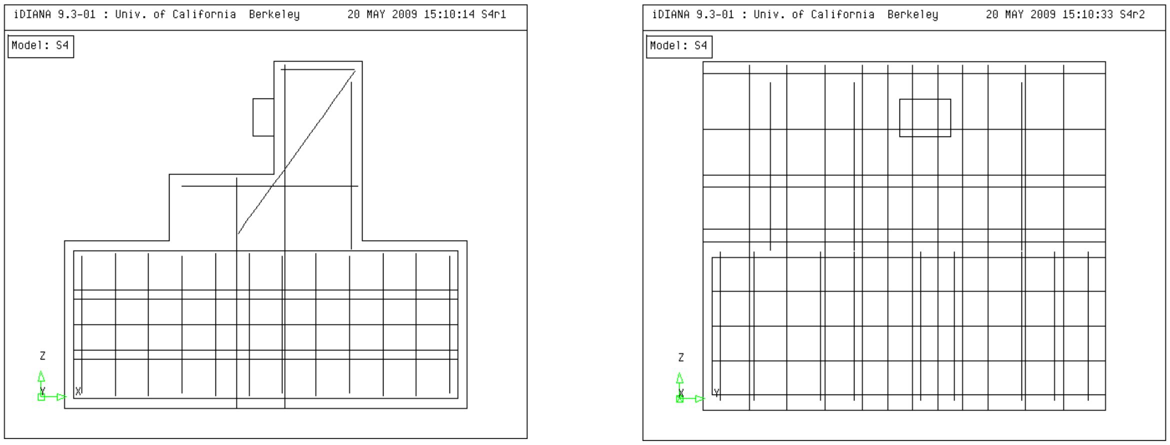

(c) Cross section of S4 (d) Elevation view of S4

Fig. 3.2 Embedded reinforcement of specimens S1 and S4.

3.1.1 Mesh Size Convergence Study

To validate the selected mesh size, a convergence study was conducted using meshes of 436, 1894, and 15100 elements, as shown in Figure 3.3. The resulting average element lengths are h=5.2 in. (132 mm), h=3.2 in. (81 mm), and h=1.6 in. (41 mm), respectively. For this convergence study, linear elastic behaviors were considered for both the steel and concrete. The models were loaded with a horizontal load of 100 kip (445 kN) located at the bearing plates.

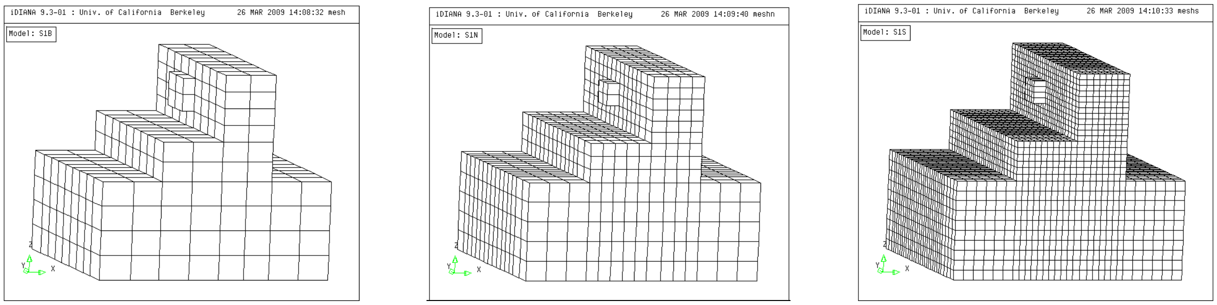

(a) h=5.2 in. (132 mm) (b) h=3.2 in. (81 mm) (c) h=1.6 in. (41 mm)

Fig. 3.3 Mesh sizes considered.

The comparison between the horizontal displacements of the concrete is shown in Figure 3.4a. The mesh with h=3.2 in. (81 mm), which was adopted in the post-test FEA, predicts a horizontal displacement of 0.0089 in. (0.23 mm), which is 6% lower than the displacement prediction for the mesh with h=1.6 in. (41 mm). The comparison between the horizontal strains at a concrete element is shown in Figure 3.4b. The strain is measured at an integration point of a concrete element located adjacent to the seat edge, at the bearing height, as shown by the insert in Figure 3.4b. The strain is measured in the direction normal to the insert of Figure 3.4b to measure the bending action of the seat about the longitudinal axis of the bridge. For this case, the mesh with h=3.2 in. (81 mm) predicts a tensile strain of 0.15%, which is 17% lower than the strain prediction for the mesh with h=1.6 in. (41 mm).

From the convergence study it is concluded that a mesh with h=3.2 in. (81 mm) presented reasonable results (Fig. 3.3b). The mesh with h=1.6 in. (41 mm) is more accurate, but the required time necessary to conduct a nonlinear analysis was considered prohibitive. The mesh size with h=5.2 in. (132 mm) showed significant error in the results to conduct the post-test analysis. Additionally, this coarser mesh presents problems to accurately model the bearing plate size and the utility openings geometry.

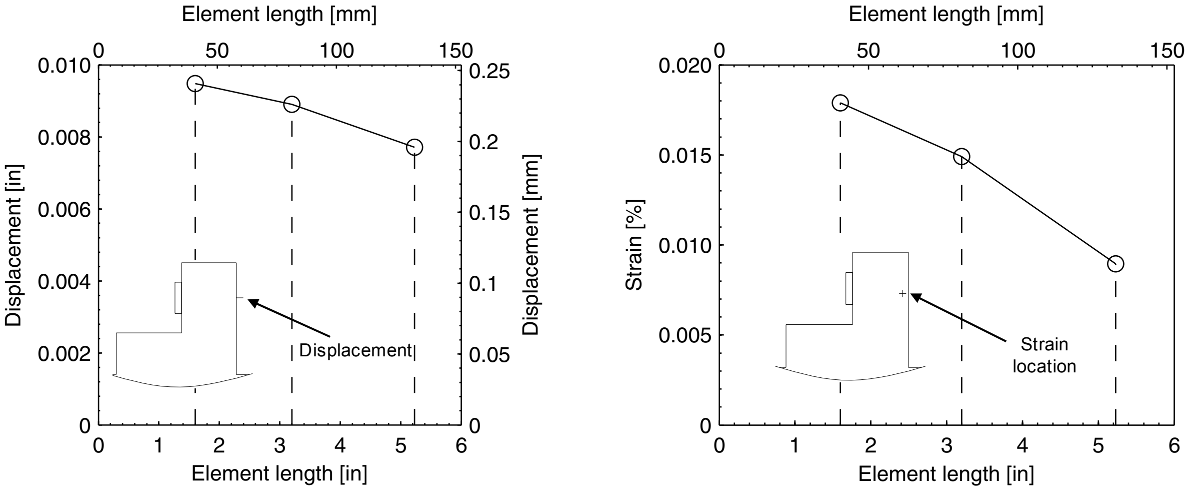

(a) Horizontal displacement

(b) Strain at concrete in direction longitudinal to the specimen

Fig. 3.4 Results for different mesh sizes.

3.2 MATERIAL BEHAVIOR

The concrete and reinforcing steel properties used in the post-test FEA are based on the results of the material tests conducted as part of the experimental program (Hube and Mosalam 2009). Additionally, for selecting the concrete properties, the results of Section 2.4 are considered.

The concrete material is modeled using the total strain rotating crack model with the properties summarized in Table 3.1. For the tensile behavior, linear tension softening is considered with a tensile strength of $4\sqrt{f_c'}$ (psi units) and a fracture energy based on the CEB-FIP (Comité 1990) code recommendations (Eq. 2.4). The crack band width considered is $h = \kappa\sqrt[3]{V_e}$ where V_e is the volume of the FE and κ is a calibration parameter chosen as κ=2.0.

For the compressive behavior, an elastic-perfectly plastic behavior is assumed, where the compressive strength and the modulus of elasticity were obtained from the material tests. The compression softening due to perpendicular cracking is incorporated using Equations (2.10) and (2.11). It is important to note that the elastic-perfectly plastic assumption for the compressive behavior is adequate to model the ISH behavior because the reduction of the compressive strength at high strain level was achieved due to the compression softening caused by orthogonal cracking. In fact, the locations where the compressive strains of concrete were larger than ε_o

(strain at peak concrete strength) were characterized by having large tensile strains in the perpendicular directions.

Table 3.1 Concrete properties.

Property	S1, S2	S3, S4 and S5
Compressive strength f_c' [ksi (MPa)]	6.30 (43.4)	6.87 (42.4)
Modulus of elasticity E_c [ksi (GPa)]	3170 (21.9)	2910 (20.0)
Tensile strength f_t [ksi (MPa)]	0.32 (2.2)	0.33 (2.3)
Fracture energy G_f^I [lbf/in. (N/m)]	0.32 (56)	0.34 (59)

The constitutive model of the reinforcing steel was obtained from the stress-strain tests conducted on the reinforcing bars, and includes strain hardening (Hube and Mosalam 2009). The constitutive models follows the Voce equation (Voce 1948), which is implemented in the FE software DIANA (2008). For the steel material, the behavior in tension and compression is assumed identical. The steel properties are summarized in Tables 5.3 and 6.3 in Hube and Mosalam (2009).

3.3 SOLUTION STRATEGY

The nonlinear FEA was conducted using the regular Newton-Raphson strategy. In this strategy, the tangent stiffness is calculated at every iteration. Because concrete is subjected to severe cracking and the material model uses a secant stiffness, the maximum number of iterations was set to 200 to assure convergence.

To stop the iteration process at each load increment, the force norm convergence criterion was used (Zienkiewicz and Taylor 2005). The norm of the applied load vector f_{ext} is compared with the norm of the out-of-balance force vector g_i at the i-th iteration. Convergence is achieved if,

$$\sqrt{g_i^T \bullet g_i} \leq \eta \sqrt{f_{ext}^T \bullet f_{ext}} \tag{3.1}$$

where η is the tolerance that was set to η=0.01, superscript T indicates a transpose, and $\bullet$ indicates the dot product.

The load at the ISHs is applied by imposing a monotonically increasing displacement at the center node of the bearing plate. To detect crack initiation, the ISHs were loaded initially with 6 displacement increments of 0.0025 in. (0.064 mm). Subsequently, the ISHs were loaded with displacement increments of 0.005 in. (0.127 mm).

3.4 SENSITIVITY ANALYSIS TO LOADING CONDITIONS

Because of the test setup characteristics, the specimens were subjected to different loading conditions. The objective of this sensitivity analysis is to determine the effect of the loading conditions in the FEA.

3.4.1 Bearing Plate Location

Specimen S1 was tested with the bearing plates located in a lower position (closer to the diaphragm). The bearing plates were not centered with respect to the seat length, resulting in an offset of approximately 0.75 in. (19 mm), as shown in Figure 3.5a.

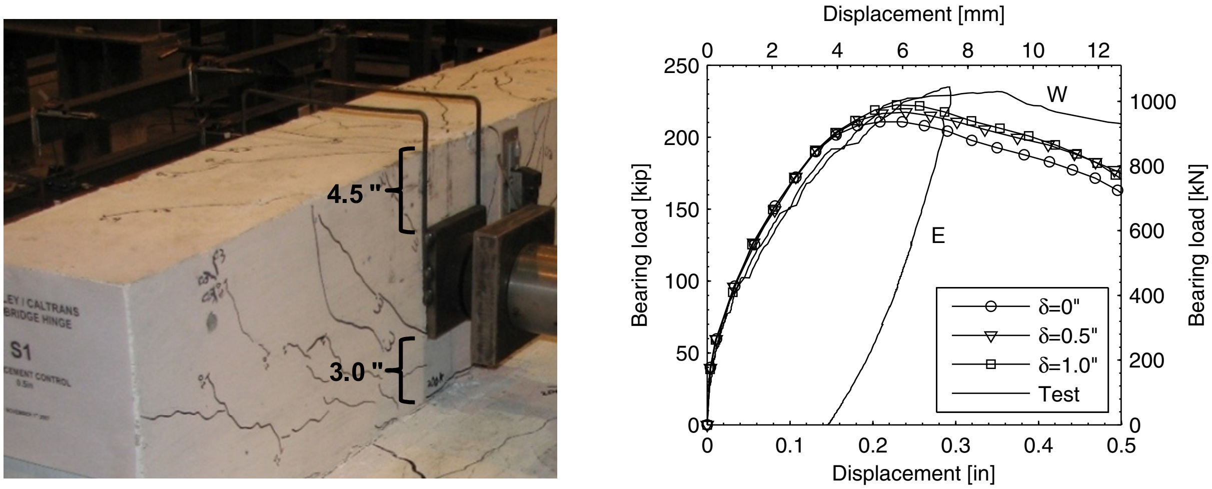

(a) West bearing plate location (b) Load-displacement

Fig. 3.5 Effect of bearing plate location in specimen S1.

The sensitivity analysis of the bearing plate location was studied using FEA. To modify the bearing plate location, the mesh of specimen S1 (Fig. 3.1a) was adjusted to obtain the desired offset. The load-displacement results for bearing plates offsets of δ =0 in., 0.5 in. (13 mm), and 1.0 in. (25 mm) are shown in Figure 3.5b. The figure shows that the predicted strength of the ISH increases when the bearing plate is located closer to the diaphragm (larger offset). Additionally, it is observed that the FEA response approaches the test result of specimen S1 when the offset is incorporated. It is concluded that the bearing plate offset of 0.75 in. (19 mm) has to be considered in the FEA of specimen S1.

3.4.2 Loading Point Location

Specimens S4 and S5 were tested with centered bearing plates, but with the tilt saddles not centered with respect to these bearing plates, as shown in Figure 3.6a for S4. This offset between the bearing plate and the applied load caused a premature localized bearing failure in both specimens, as shown in Figure 3.6a. The offset measured in both specimens was approximately 0.70 in. (18 mm).

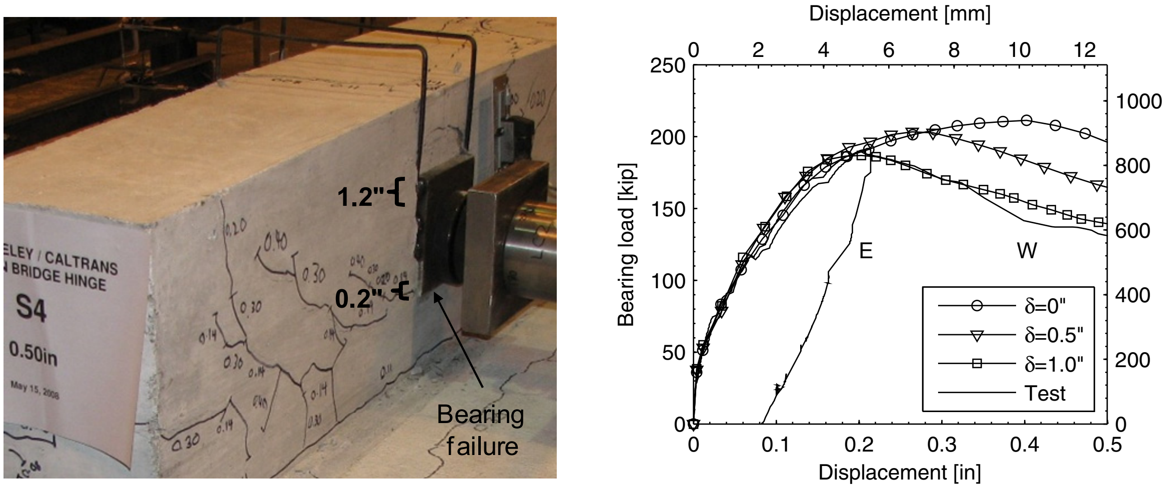

(a) Loading point offset on the west side

(b) Load-displacement

Fig. 3.6 Effect of loading point location in specimen S4.

The sensitivity analysis of the loading point location was studied using FEA. To modify the loading point location, the coordinate of the center node of the bearing plate was modified to obtain the desired offset (the concrete mesh was not modified). The load-displacement results for a loading point offset of $\delta=0$ in., 0.5 in. (13 mm), and 1.0 in. (25 mm) are shown in Figure 3.6b. The figure shows that the predicted strength of the ISH decreases as the offset of the loading point increases. Additionally, it is observed that the FEA response approaches the test result of specimen S4 when the offset is incorporated. This result is confirmed on the local level when the strains of the reinforcement are compared. The strain of the diagonal bar D1, located at near the bearings, versus the bearing displacement is shown in Figure 3.7. The figure shows that an offset of δ=1.0 in. (25 mm) predicts a strain plateau of the diagonal bar at a strain level of 1.7%. This prediction approaches the experimental result, where a strain plateau was observed in the bar located at the west side (side where failure was observed) of the specimen. It is concluded that the loading point offset of 0.70 in. (18 mm) has to be considered in the FEA of specimens S4 and S5.

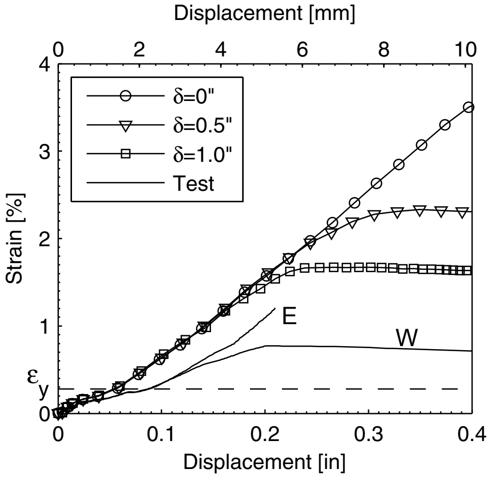

Fig. 3.7 Strain of diagonal bar versus bearing displacement.

3.5 LOAD VERSUS DISPLACEMENT

The bearing load versus displacement prediction of the FEA is compared with the experimental results (east and west bearings) for the five tested specimens in Figure 3.8. The figure shows an excellent agreement between the experimental and analytical results. The displacement is measured at the concrete surface, as shown in the insert of Figure 3.8b. For the experimental results, two load-displacement relationships are shown for each specimen, representing the load-displacement envelope of the east and west bearings. The average bearing strength of each specimen is compared with the predicted strength in Table 3.2. The table shows that the FEA gives a good prediction of the strength of the tested ISHs, where a maximum error of 6% is obtained for specimen S1.

Table 3.2 Comparison of bearing strength.

	S1	S2	S3	S4	S5
Test [kip (kN)]	233 (1036)	213 (947)	269 (1197)	191 (850)	193 (858)
FEA [kip (kN)]	220 (979)	209 (930)	264 (1174)	198 (881)	199 (885)
Error[†] [%]	+5.6	+1.9	+1.9	-3.7%	-3.1%

[†] (Test-FEA)×100/Test

The load versus displacement of specimens S1 and S2 are shown in Figure 3.8a–b. These specimens represented the as-built conditions of typical ISHs of California prestress concrete box-girder bridges. Specimen S2 was detailed identical to S1 but it contained utility openings. For the FEA, specimen S1 was modeled considering the bearing plate offset of 0.75 in. (19 mm), described in Section 3.4.1, whereas S2 was modeled without a bearing plate offset.

The load versus displacement of specimen S3 is shown in Figure 3.8c. This specimen was designed identical to S2 but with oversized bearing plates to increase the punching shear strength. It is observed that the FEA gives a good prediction of the response for the specimens with a larger bearing plate. However, the predicted descending branch is steeper than the experimental results.

The load versus displacement of specimens S4 and S5 is shown in Figure 3.8d–e. Specimens S4 and S5 were designed with low reinforcement ratio aimed to improve the performance and the constructability of ISHs. Specimens S5 was detailed identical to S4 but it contained utility openings. For the FEA, specimens S4 and S5 were modeled with a loading point offset of 0.70 in. (18 mm). It is observed that the FEA gives a good prediction of the responses. However, the experimental strengths and descending branches are lower than the FEA, which can be attributed to the anchorage failure of the punching shear reinforcement observed in these two specimens. This type of anchorage failure, shown in Figure 6.21h in Hube and Mosalam (2009), is not modeled in the FEA.

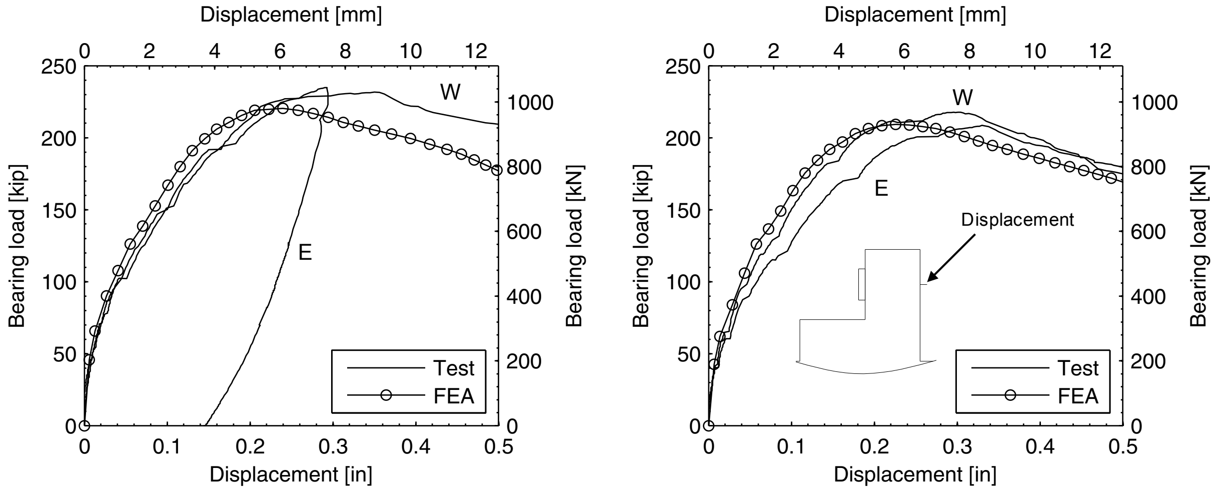

(a) S1

(b) S2

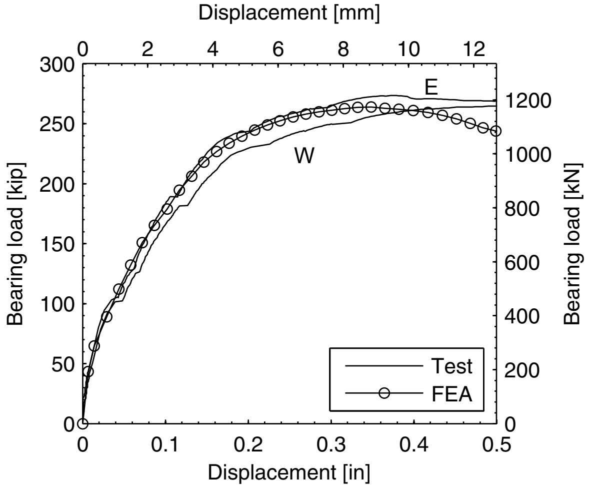

(c) S3

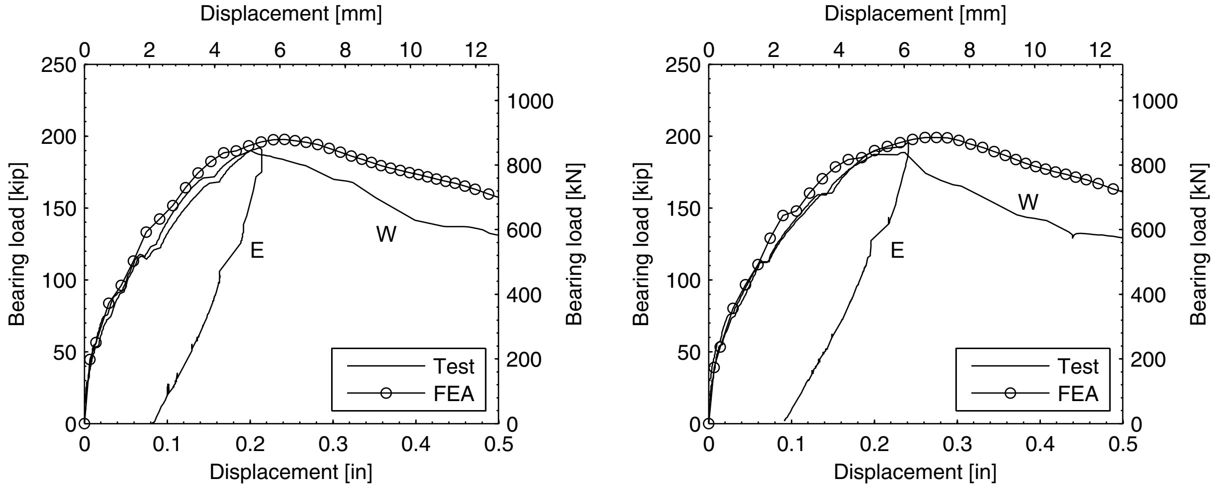

(d) S4

(e) S5

Fig. 3.8 Comparison of load-displacement relationship at bearings (east and west bearing shown for test results).

3.6 DAMAGE PROPAGATION

The comparison between the experimental and analytical results shows that the FEA provides a good estimation of the crack formation and propagation of the ISHs. For the five tested specimens, the crack initiation occurred near the seat corner with the diaphragm. Figure 3.9a shows this initial cracking in specimen S1 for a bearing load of 50 kip (222 kN). At this load level, the estimated cracks from the FEA are shown in Figure 3.9b. Here the short lines are perpendicular to the crack direction and their lengths are proportional to the crack normal strain (opening mode). It is observed that the location of the initial cracking is reproduced by the FEA. Moreover, the FEA predicts that this cracking extended through the whole specimen length (Section A-A of Fig. 3.9b), which agrees with the observed crack in Figure 3.9a.

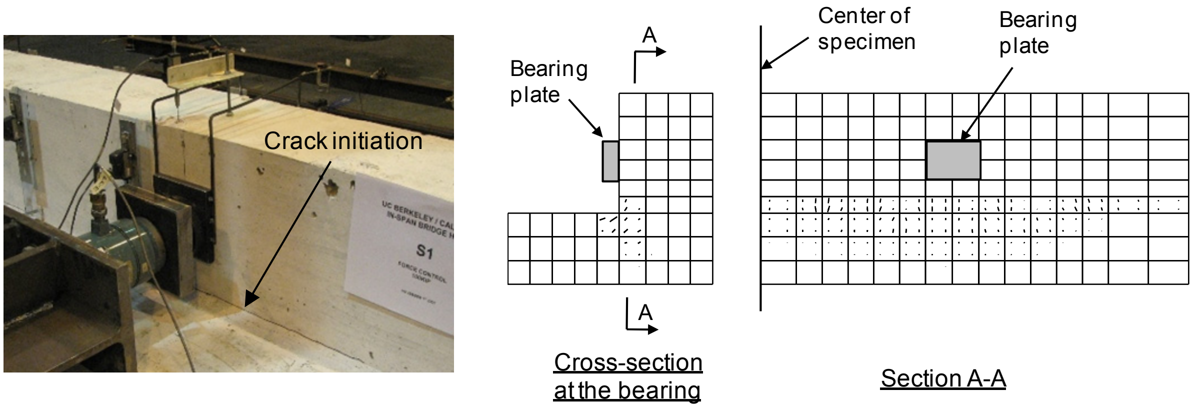

(a) Test (b) FEA

Fig. 3.9 Crack initiation in specimen S1 for 50 kip (222 kN) bearing load.

For the five tested specimens, the damage propagation continued with a bending vertical (in the test orientation) crack that appeared in the seat behind the bearing plates. Figure 3.10a shows this crack in specimen S1 for a bearing load of 75 kip (334 kN). At this load level, the estimated cracks in the FEA are shown in Figure 3.10b. It is observed that the FEA predicts accurately the formation of this secondary crack. After the vertical bending crack, a 45° inclined crack appeared in the seat towards the free end of specimens S1, S2, S4, and S5. This inclined crack did not appear in specimen S3, due to the larger bearing plates used in S3. Figure 3.11 shows the experimental and predicted cracks in specimen S1 for a bearing load of 150 kip (667 kN). It is observed that the FEA predicts adequately the diagonal crack towards the free end of the specimen.

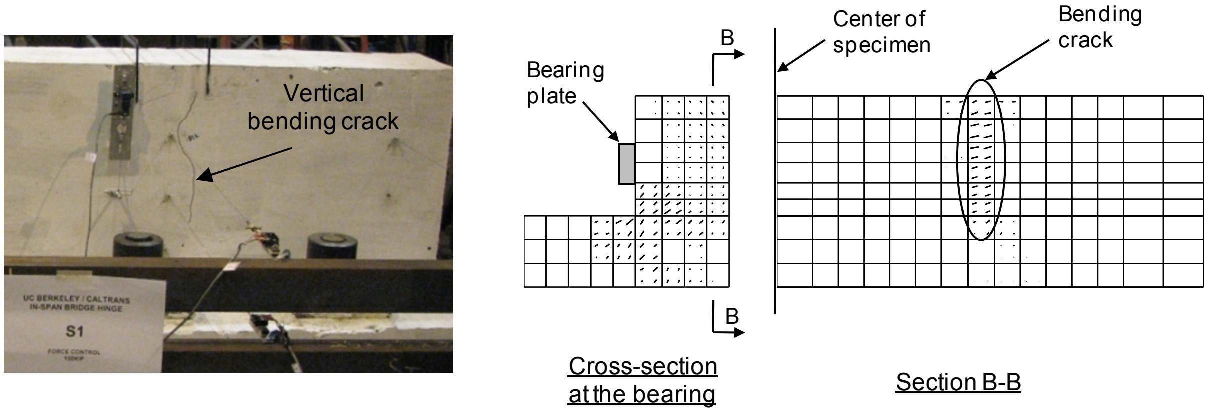

(a) Test, elevation of west side (b) FEA

Fig. 3.10 Bending crack in specimen S1 for 75 kip (334 kN) bearing load.

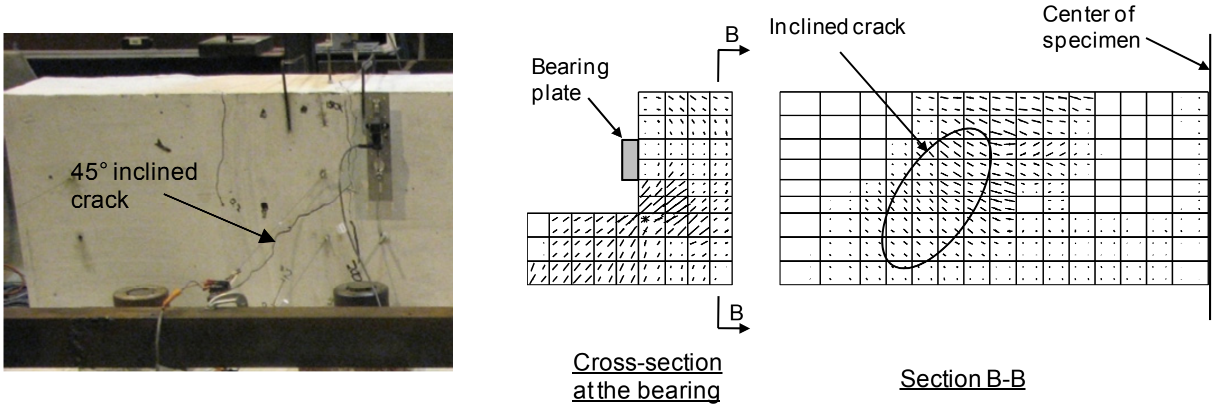

(a) Test, elevation of east side (b) FEA

Fig. 3.11 Diagonal cracking in specimen S1 for 150 kip (667 kN) bearing load.

From the test results it was concluded that ISHs fail with a combination of three failure modes: (1) one-dimensional (1D) shear, (2) two-dimensional (2D) strut-and-tie (SAT), and (3) punching shear (Hube and Mosalam 2009). The punching shear failure mode was observed at the bearings of the specimens mostly in one direction. For specimens S1, S3, S4, and S5, the punching shear cracks were observed towards the center of the specimens, whereas for specimen S2, the punching shear cracks were observed towards the free end. The FEA of the tested specimens was able to predict the combined failure modes of the specimens. However, the punching shear failure mode was predicted towards the free end for the five specimens.

In Specimen S2, punching shear was observed in the west side, and shear failure was observed in the east side. Figure 3.12a shows punching shear failure of the west side where the diagonal punching shear crack at the top of the seat (in the test orientation) only appeared towards the west free end of the specimen, as marked with an arrow in Figure 3.12a. Towards the middle of the specimen, the west side experienced shear failure that was connected with a 1D shear failure mode of the east bearing. This combined failure mode is shown in Figure 3.13. The predicted cracks at the peak strength of specimen S2 are shown in Figure 3.12b. The cross sections at the bearing location (section B-B) and at the center of the specimen (section C-C) show shear cracks that agree with the experimental observation. Moreover, the top view of the seat (section D-D) shows punching shear cracks towards the west free end.

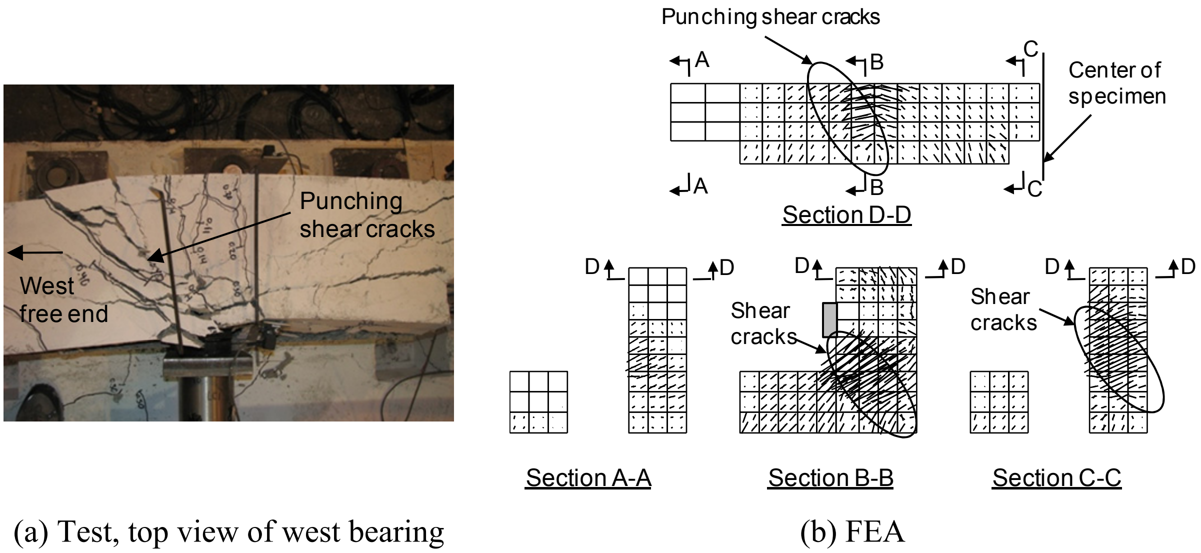

(a) Test, top view of west bearing

(b) FEA

Fig. 3.12 Cracking at failure, specimen S2.

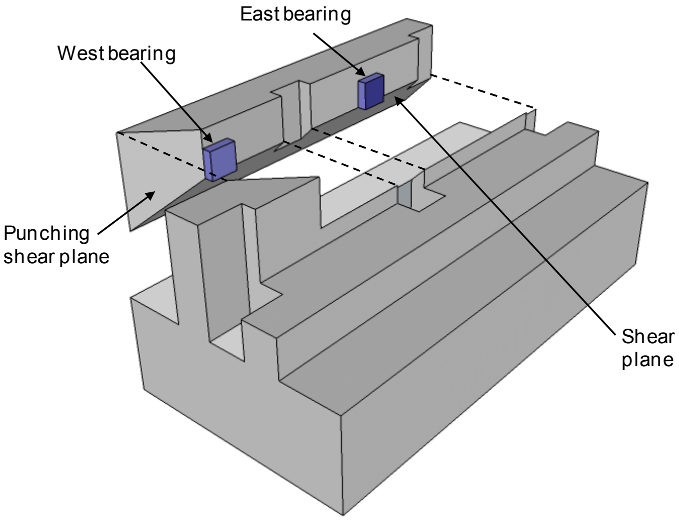

Fig. 3.13 Failure mode, specimen S2.

Specimen S3 was designed with larger bearing plates to avoid localized punching shear failure. When S3 reached the peak load, a global shear failure mode was observed throughout the whole length of the specimen. When the specimen was responding on the descending branch, a punching shear mechanism was observed on the east side, as shown in Figure 3.14a. The estimated cracks at the peak strength of specimen S3 are shown in Figure 3.14b. The cross section at the bearing (section B-B), center (section C-C) and free end (section A-A) location suggest that a global shear mechanism is predicted by the FEA. The top view of the seat (section D-D) shows punching shear cracks towards the free end of the specimen, contrary to the experiment, where punching shear cracks were observed at both sides of the bearing (Fig. 3.14a).

For specimens S4 and S5, anchorage failure was observed in the vertical (horizontal in the test orientation) reinforcing bars of the seat, shown in Figure 3.15a. The crack prediction at the top (in the test orientation and near the free end) of the seat (equivalent to section D-D in Fig. 3.14) at the peak strength for specimen S4 is shown in Figure 3.15b. This crack prediction does not consider the anchorage failure of the reinforcement, because the reinforcing steel is modeled using the embedded reinforcement formulation. If the vertical bars of the seat are eliminated from the FE model of S4, larger diagonal and horizontal cracks are predicted at the top of the seat, as shown in Figure 3.15c. The crack pattern observed in S4 is between Figure 3.15b and c. Therefore, it can be concluded that the damage prediction of the FEA is sensitive to the reinforcement details.

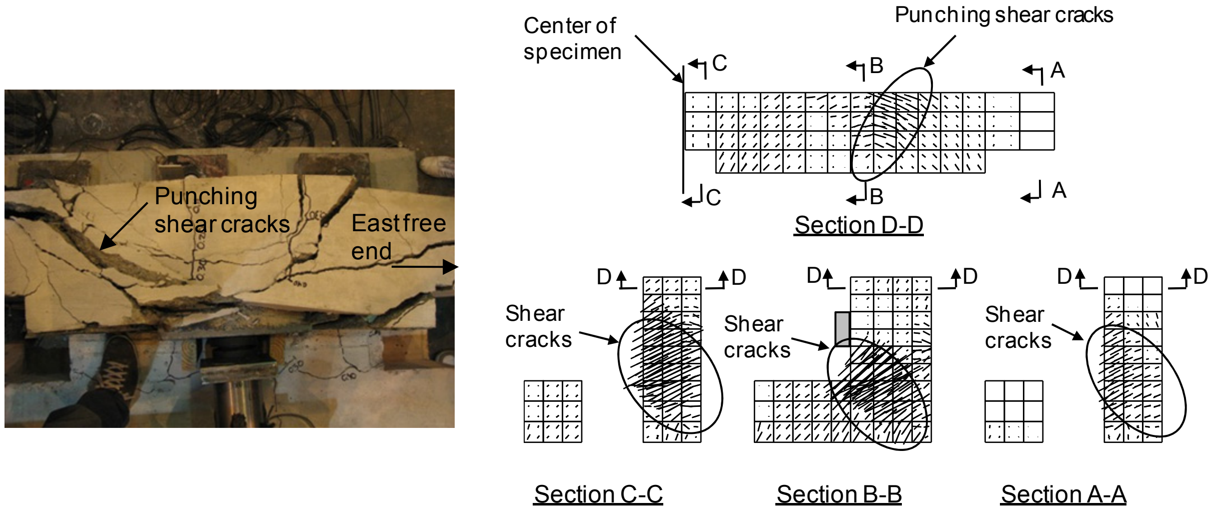

(a) Test, top view of east bearing

(b) FEA

Fig. 3.14 Cracking at failure, specimen S3.

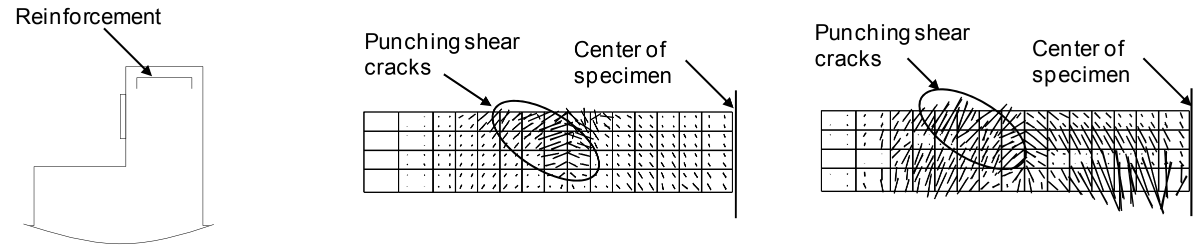

(a) Vertical reinforcement of the seat (b) As-built (c) Without vertical reinforcement of the seat

Fig. 3.15 Predicted cracking for specimen S4 with (as-built) and without vertical reinforcement of seat (in original bridge orientation).

3.7 REINFORCEMENT BEHAVIOR

The comparison between the experimental and analytical results shows that the FEA provides a good estimation of the reinforcement behavior of the ISHs. For the tested specimens, the stresses of the reinforcing bars were computed from the strain measurements using the stress-strain relationships obtained from the reinforcing bar material tests (Hube and Mosalam 2009). The details of the reinforcement of the tested specimens are shown in Figure 3.16.

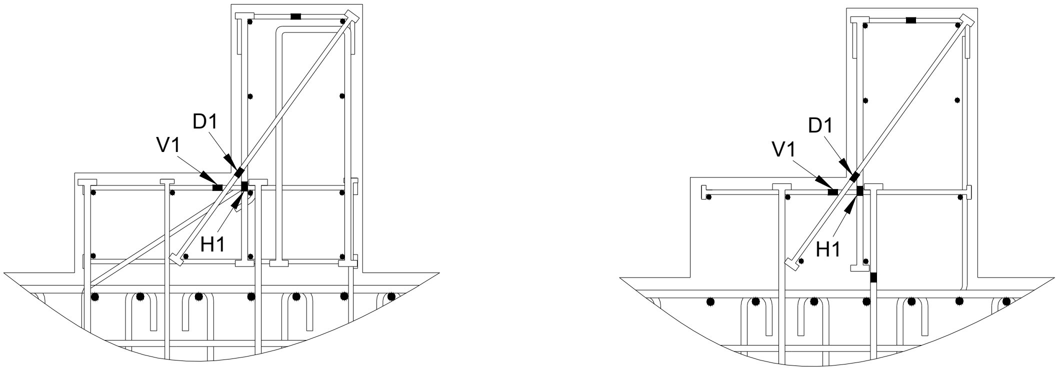

(a) Specimens S1, S2 and S3 (b) Specimens S4 and S5

Fig. 3.16 Reinforcement details of tested ISHs (in test orientation).

The comparison between the reinforcement stresses versus the bearing load for all specimens (S1 to S5) is shown in Figure 3.17. The figure shows the stresses of the principal bars located at the bearing cross section. For the analytical results, the stresses of the bars were calculated at the location of the corresponding strain gages, shown in Figure 3.16. For the experimental results, two load-displacement relationships are shown, representing the envelopes measured at the east and west bearings. The yield stresses of the reinforcing bars are shown in Figure 3.16. The #3 (D1 and V1) and #4 (H1) bars of each specimen were characterized by a different yielding stress. Equivalent to the experimental results, the FEA predicts yielding initiation for all the specimens in the diagonal bar D1. Figure 3.16 shows that the FEA predicts the stress of the diagonal bar D1 accurately for the five specimens. The comparison between the stresses of the horizontal (vertical in the test orientation) bar H1 and the vertical (horizontal in the test orientation) bar V1 are not as accurate as the diagonal bar D1, especially for specimens S4 and S5. However, for high bearing loads, the FEA of S4 and S5 predicts yielding of these reinforcements, which agree with the test results.

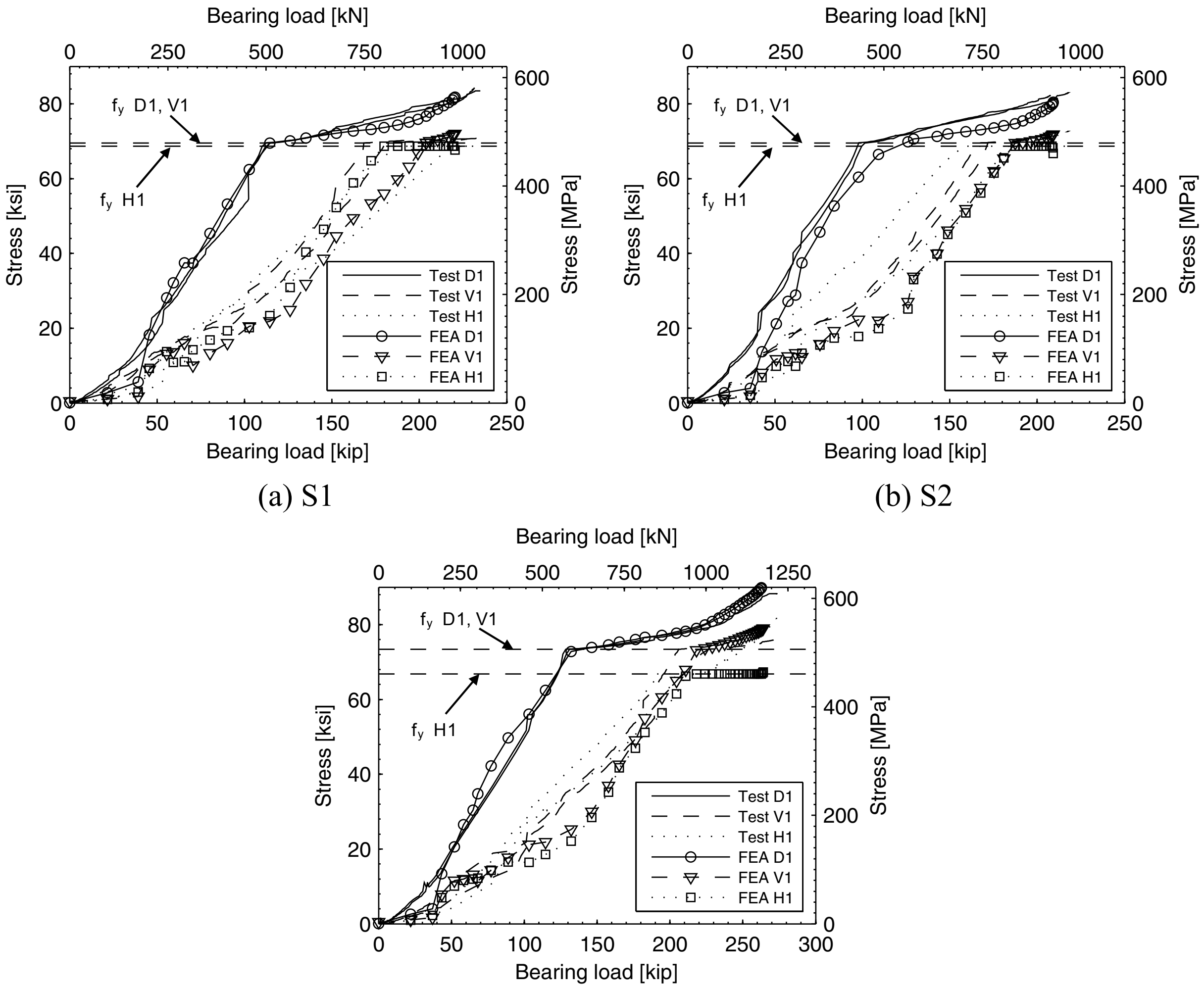

(a) S1

(b) S2

(c) S3

Fig. 3.17 Comparison of stresses in reinforcement at bearing cross section (east and west bearings shown for test results).

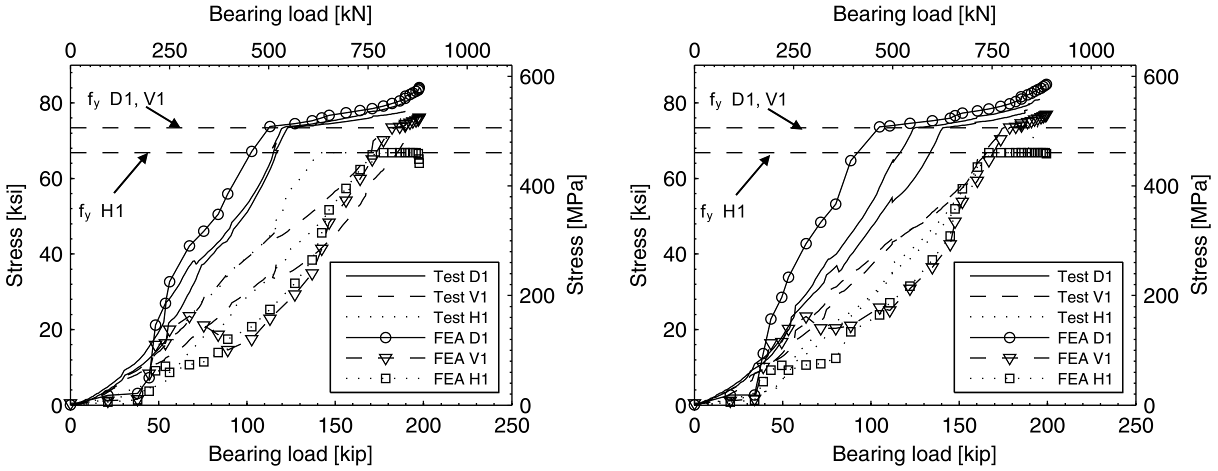

(d) S4 (e) S5

Fig. 3.17—*Continued.*

At the peak ISH strength, the FEA stress prediction of the reinforcing bars located in the bearing cross section of specimen S1 and S4 is shown in Figure 3.18. The stress results of S1, Figure 3.18a, show that the 2D SAT proposed for S, Figure 5.7 in Hube and Mosalam (2009) is developed. However, the FEA predicts elastic response i.e., no yielding of the vertical (horizontal in the test orientation) bar V3 of Figure 3.18a. This prediction agrees with the experimental results (Hube and Mosalam 2009), which showed a maximum stress of 0.88 f_y for bar V3 located at the west bearing. For specimen S4, Figure 3.18b shows that the 2D SAT proposed in Hube and Mosalam (2009) for S4 is also developed at the bearing cross section.

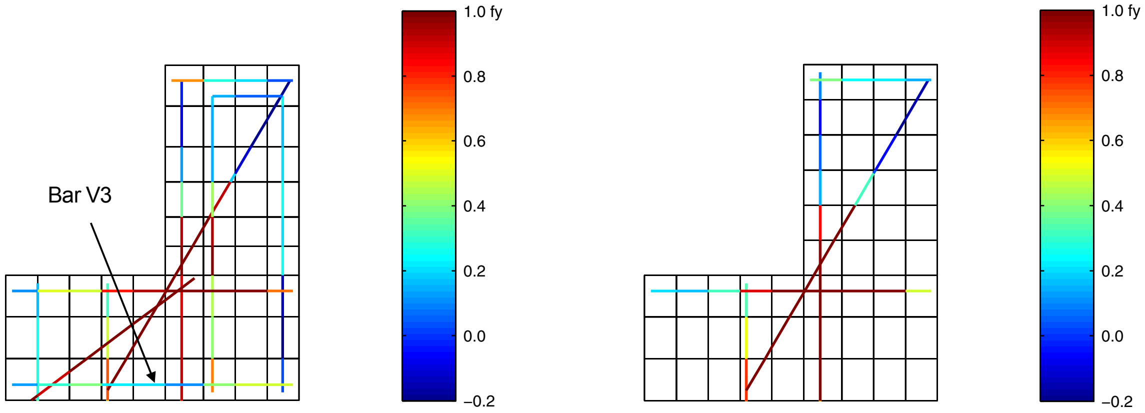

(a) S1 (b) S4

Fig. 3.18 Stress prediction of reinforcing bars at the bearing cross section, from FEA for specimens S1 and S4.

To measure the 3D load transfer from the bearings to the whole diaphragm length, strain gages were installed on reinforcing bars throughout the specimen length. The comparison between the strain distributions on the reinforcing bars through the specimen length for specimens S1 and S3 is shown in Figure 3.19 for bearing loads of 100 kip (445 kN) and 200 kip (890 kN). For a bearing load of 100 kip (445 kN), i.e., 43% and 37% of the peak experimental strength (Table 3.2) for specimens S1 and S3, respectively, the lower plots of Figure 3.19 show that the FEA strain predictions of the diagonal bars D1 and vertical bars V1 are adequate for both specimens. For a bearing load of 200 kip (890 kN), i.e., 86% and 74% of the peak experimental strength (Table 3.2) for specimens S1 and S3, respectively, the higher plots of Figure 3.19 show that the differences between the experimental and analytical results are larger. However, at this load level, severe cracks were observed in the tested specimen, which induced significant strain variations along the bar length. These variations were also observed in the FEA where the strains predictions are very sensitive to the selection of the integration point along the bar length. Finally, Figure 3.19 shows that the strain predictions for S3 are more uniform than the strains for S1 near the bearing region. This is caused by the larger bearing plate incorporated in the FEA of S3.

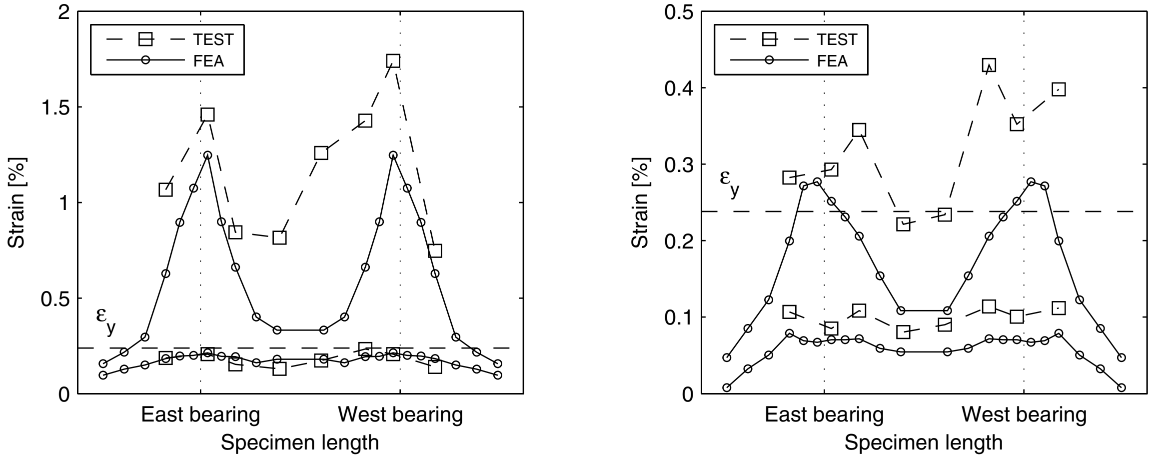

(a) S1, diagonal bars D1

(b) S1, vertical bars V1

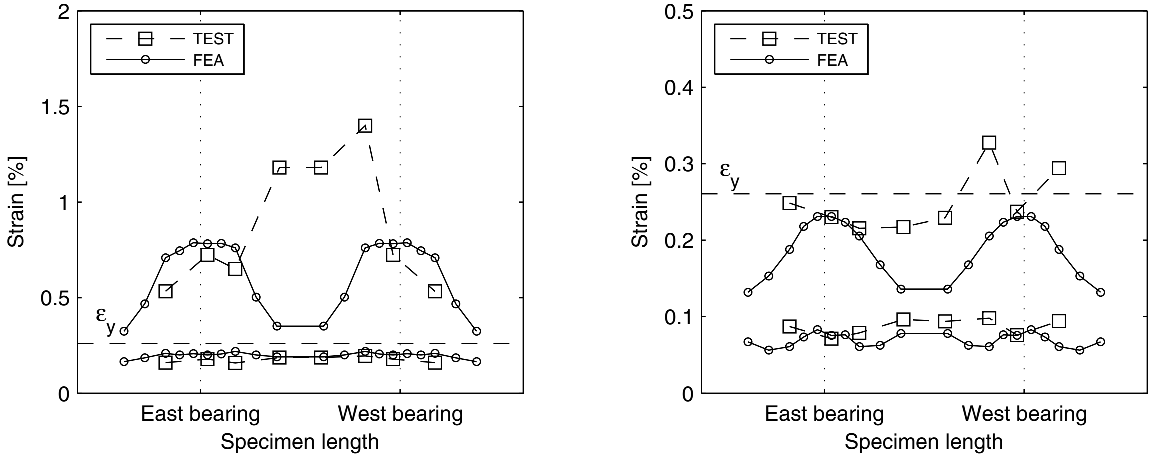

(c) S3, diagonal bars D1

(d) S3, vertical bars V1

Fig. 3.19 Strain distributions throughout ISH length at 100 kip (445 kN) (lower plots) and 200 kip (890 kN) (higher plots) of bearing load.

3.8 CYCLIC BEHAVIOR

The ISHs were tested using a quasi-static cyclic compression load. However, the post-test FEA were conducted using a monotonically increasing load, and the predicted responses were compared with the envelopes of the experimental results. Figure 3.20 shows the load-displacement comparison of specimen S4 if the cyclic loading is incorporated in the FEA of specimen S4. It is concluded that the cyclic characteristics of the loading do not affect the prediction of the analytical model due to the relatively high density of the reinforcement in the

ISH region. Therefore, the influence of compression-only cyclic loading on the concrete constitutive model is minimal.

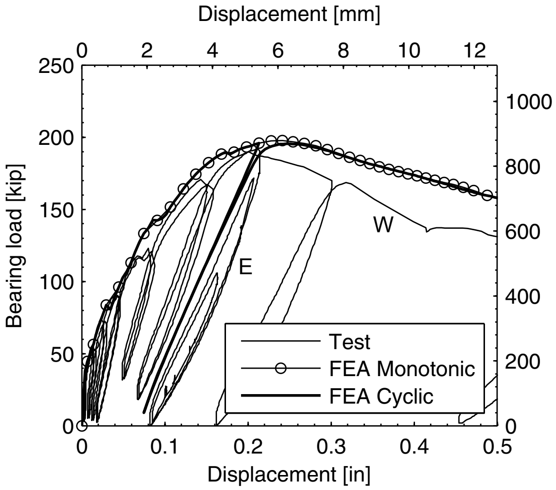

Fig. 3.20 Load-displacement of specimen S4 with monotonic and cyclic loading.

3.9 CONCLUSIONS OF POST-TEST FEA

From the comparison of the experimental and analytical results, it is concluded that the proposed FEA is adequate to simulate the behavior, the strength, and the mode of failure of ISHs. The FEA is sensitive to the reinforcement details, the bearing plate size, the bearing plate location, the loading condition, and to the presence of utility openings. Therefore, the proposed 3D FE model can be utilized to perform a parametric study of ISH regions for the purpose of developing design guideless as documented in the following chapters of this report.

4 Parametric Study

The parametric study of ISHs is conducted using the FEA described in the previous chapters. This parametric study is intended to expand findings from the real experimental program (five specimens), by using virtual experiments. The variables analyzed in the parametric study are the reinforcement steel ratio and detailing characteristics, the size of the bearing plate, the aspect ratio of the seat, the load eccentricity, and the characteristics of the utility openings. This parametric study is aimed to develop design guidelines for ISH of prestressed concrete box-girder bridges. Because of symmetry, only half of the virtual specimens are considered in the FE models of the parametric study.

4.1 REFERENCE ISH

A reference ISH was needed to be defined to conduct the virtual experiments of the parametric study. The geometry of the reference ISH was selected identical to specimen S1, which is characterized by not having utility openings. The reference ISH represents a 1/3-scale specimen anchored to the floor; its mesh is shown in Figure 4.1.

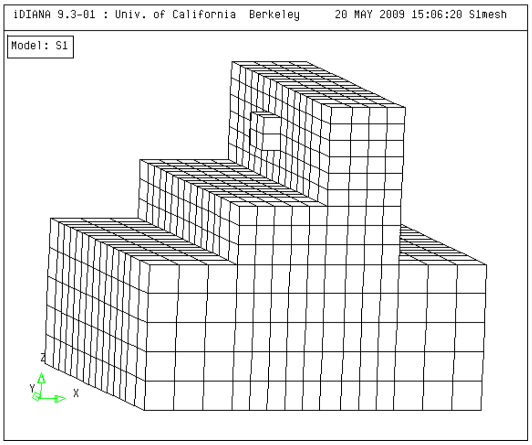

Fig. 4.1 Concrete finite element mesh of reference ISH.

Based on the projects survey (Hube and Mosalam 2009), the parametric study is conducted with a concrete compressive strength of f_c'=5 ksi (34.5 MPa). The modulus of elasticity is based on the ACI code (ACI 2008) recommendation, E_c= 4030 ksi (27.8 GPa), and the Poisson's ratio is chosen as ν=0.2 (Caltrans 2004). For the tensile behavior, linear tension softening is considered with a tensile strength of $4\sqrt{f_c'}$ (psi units) =0.28 ksi (1.9 MPa) and a fracture energy value based on the CEB-FIP (Comité 1990) code recommendations, G_f^I=0.28 lbf/in. (49 N/m). The crack band width considered in the concrete material model is $h = \kappa\sqrt[3]{V_e}$, where V_e is the volume of the FE and κ =2.0 is the calibration parameter. For the reinforcing steel, elastic-perfectly plastic behavior is assumed with a yield stress of f_y=60 ksi (414 MPa) and modulus of elasticity of E_s=29000 ksi (200 GPa).

The reinforcing steel ratios included in the diaphragm and the seat are shown in Figure 4.2. It is assumed that the end diaphragm with prestressed blockout is not a critical element of the ISH and was excluded from this research (Hube and Mosalam 2009). In Figure 4.2, ρ_{sd}, ρ_{sv}, ρ_{sh}, and ρ_{slon} represent the diagonal, vertical, horizontal, and longitudinal reinforcing steel ratios of the seat, respectively. Also in Figure 4.2, ρ_{dd}, ρ_{dv}, ρ_{dh}, and ρ_{dlon} represent the diagonal, vertical, horizontal, and longitudinal reinforcing steel ratios of the diaphragm, respectively. These reinforcing steel ratios are defined in Equation (2.4) in Hube and Mosalam (2009).

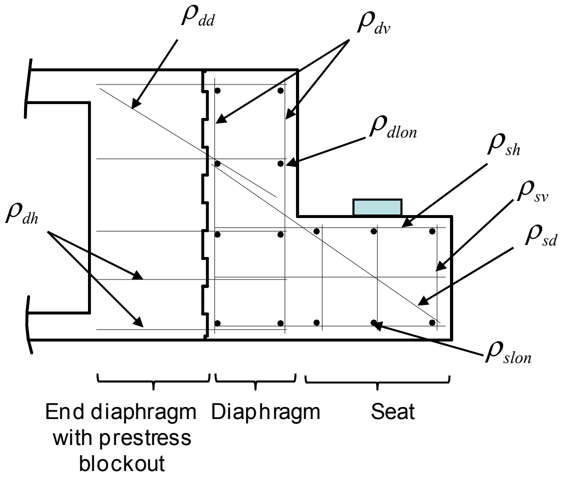

Fig. 4.2 Reinforcing steel designations of ISH.

The reinforcing steel ratios of the tested specimens, the surveyed projects (Hube and Mosalam 2009), and the average ratios of the surveyed projects are shown in Figure 4.3. The reinforcing steel ratios of the reference ISH are selected as the average ratios of the surveyed projects (see Table 4.1). The ratios of the reference ISH are different from those of the as-built specimen S1, because the ratios of S1 were based mainly on the San Francisco Approach, Project 4 in Figure 4.3 which is the main project used to define the prototype ISH for the experimental program. Similar to the tested specimens, the reinforcing steel ratios of the reference ISH are adopted near the bearings, defined by an equivalent width of 1.5 times the seat height. Beyond this region, the reinforcing steel ratios are reduced to 66% of the values listed in Table 4.1, except for the ratios of the longitudinal bars, which are kept constant throughout the specimen length.

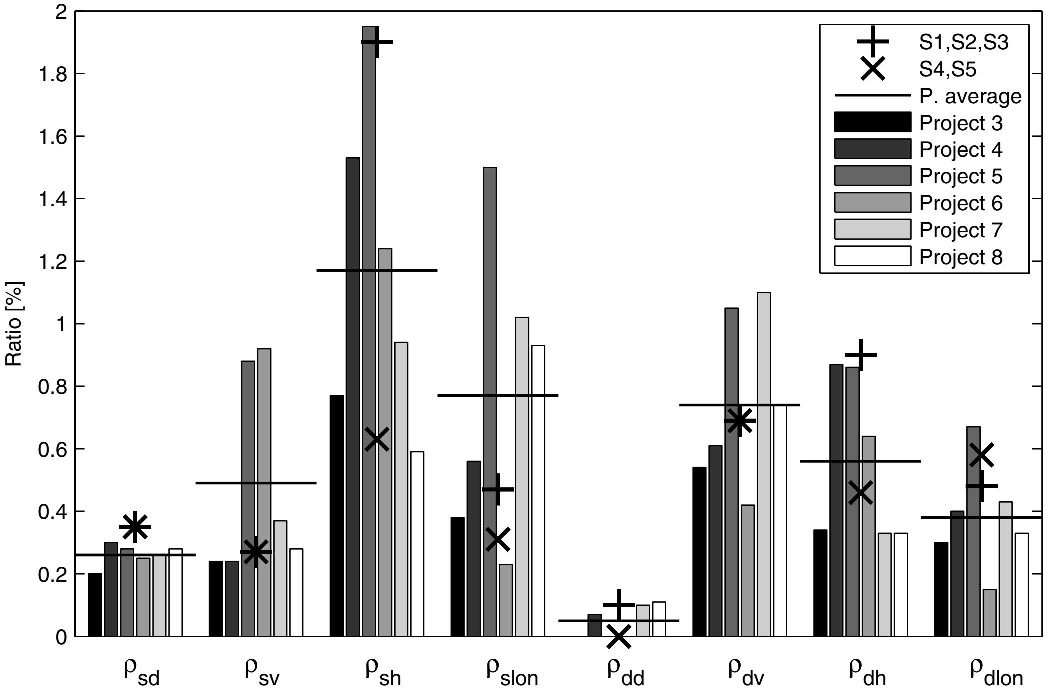

Fig. 4.3 Reinforcing steel ratios of ISH [%].

Table 4.1 Summary of reinforcing steel ratios of ISH [%].

	ρ_{sd}	ρ_{sv}	ρ_{sh}	ρ_{slon}	ρ_{dd}	ρ_{dv}	ρ_{dh}	ρ_{dlon}
S1, S2, and S3	0.35	0.27	1.90	0.47	0.10	0.69	0.90	0.48
S4 and S5	0.35	0.27	0.63	0.31	0.00	0.46	0.58	0.36
Projects average	**0.26**	**0.49**	**1.17**	**0.77**	**0.05**[†]	**0.74**	**0.56**	**0.38**

[†] ρ_{dd} is chosen equal to zero in the reference ISH

The detailing of the reinforcing steel of the reference ISH, shown in Figure 4.4, is selected based on the experimental results and the common practice observed from the surveyed projects. Near the bearing, and similar to the tested specimens, the bars are spaced at 3 in. (76 mm), except for the longitudinal bars. Beyond these regions, the bars are spaced at 4.5 in. (114 mm). Similar to the tested specimens, the diagonal reinforcement of the seat (ρ_{sd}) is oriented at 36°, as shown in Figure 4.4a. For constructability concerns, the vertical reinforcement of the seat (ρ_{sv}) is concentrated in a single layer located at the edge of the seat, as shown in Figure 4.4a. The horizontal reinforcement of the seat (ρ_{sh}) is distributed through the seat height h using 3 layers, located (from the bottom) at $0.1h$, $0.65h$ and $0.9h$. The diagonal reinforcement of the diaphragm (ρ_{dd}) was eliminated from the reference ISH (similar to the tested specimens S4 and S5), to improve constructability. Moreover, the predicted behavior of the reference ISH is not affected by the presence of these diagonal bars, which are characterized by having a low reinforcement ratio (see Fig. 4.3). The vertical reinforcement of the diaphragm (ρ_{dv}) is divided in two bars, as shown in Figure 4.4b. The horizontal reinforcement of the diaphragm (ρ_{dh}) is distributed through the diaphragm height d_h using 4 layers, located (from the bottom) at $0.05d_h$, $0.4d_h$, $0.65d_h$ and $0.9d_h$. The proportion of each layer of the horizontal reinforcement in the seat and the diaphragm, and of the vertical reinforcement in the diaphragm, shown in Figure 4.4, is selected based on the experimental and post-test FEA results of the tested specimens. Finally, the longitudinal reinforcement, of the seat and diaphragm, is detailed using 8 bars located in each region, as shown in Figure 4.4.

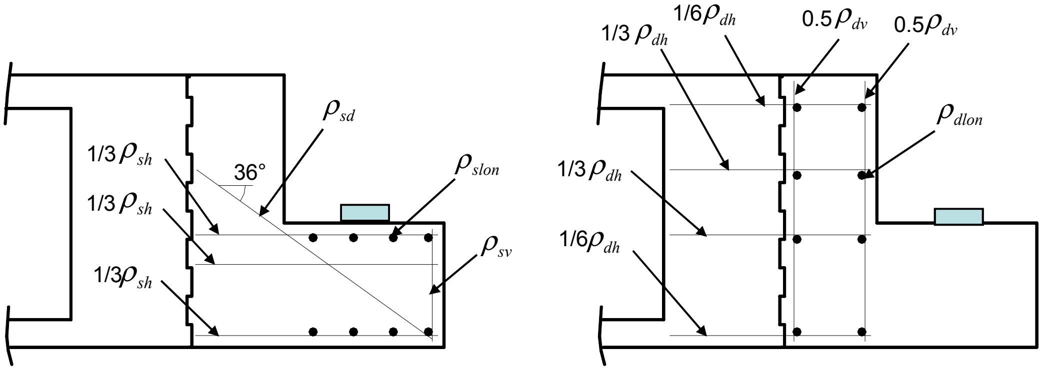

(a) Seat (b) Diaphragm

Fig. 4.4 Details of reinforcing steel in reference ISH.

The load-displacement relationship predicted for the reference ISH is shown in Figure 4.5a. The predicted strength is C_r=155 (689 kN) at a displacement of Δ_r=0.17 in. (4.3 mm). The load-displacement relationship is interrupted at 0.48 in. (11.8 mm) because the convergence criterion was not achieved in the FEA. Yielding of the reinforcement is initiated in the diagonal bars of the seat at an applied load of 80 kip (356 kN), i.e., at 0.52C_r, as indicated by the circle in Figure 4.5a. The predicted cracking at the peak load is shown in Figure 4.5b. This crack pattern is similar to the predicted cracks for the tested specimens, where some punching shear cracks are observed in section A-A.

The strength and displacement of the reference ISH are lower than the experimental results because the reference ISH considers nominal material properties for the purpose of developing the design recommendations presented in Chapter 5. These nominal material properties are lower than material properties of the tested specimens. Additionally, the reference ISH considers smaller amount of diagonal reinforcement of the seat (ρ_{sd} in Table 4.1) than that of the tested specimens. This type of reinforcement is very effective on the ISH strength, as discussed later.

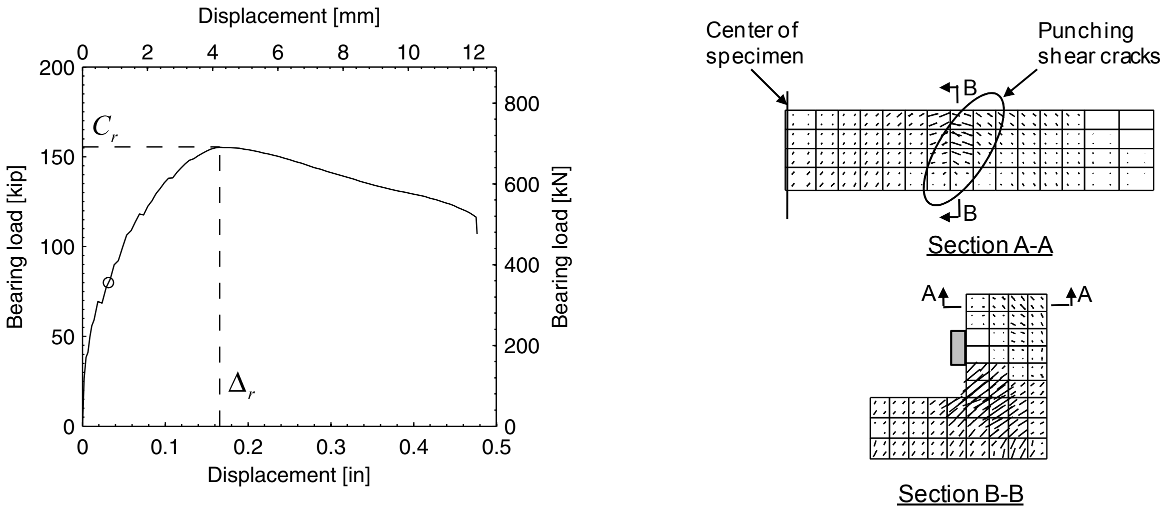

(a) Load-displacement relationship

(b) Cracking at peak load

Fig. 4.5 Reference ISH results.

4.2 REINFORCEMENT

A parametric study is conducted focusing on the reinforcement ratios and detailing characteristics of the reinforcing steel located in the seat and diaphragm (Fig. 4.4). First, the effect of using concentrated reinforcing bars near the bearing plates is evaluated. Subsequently, the effect of the reinforcement ratio and detailing characteristics of the designated reinforcement in Figure 4.2 is evaluated. For the reinforcing steel of the seat, this parametric study is conducted for the reinforcement ratios of the diagonal, vertical, horizontal, and longitudinal bars. Additionally, different detailing alternatives are analyzed for the diagonal, vertical, and horizontal bars of the seat. For the reinforcing steel of the diaphragm, this parametric study is conducted for the reinforcement ratios of the vertical and horizontal bars. For the vertical bars of the diaphragm, two detailing alternatives are analyzed. The longitudinal reinforcement of the diaphragm is not analyzed in this parametric study because it was considered not critical based on the experimental results as discussed in Hube and Mosalam (2009). It is to be noted that all load-displacement relationships of the parametric study are normalized with respect to the peak load and the corresponding displacement for the reference ISH.

4.2.1 Reinforcement Concentration Near Bearings

The reinforcing steel ratios of the reference ISH are adopted near the bearing, defined by an equivalent width of 1.5 times the seat height. As stated above, beyond this region, the reinforcing steel ratios are reduced to 66% of the values listed in Table 4.1, except for ratios of the longitudinal bars, which are kept constant throughout the specimen length. To study the effect of the reinforcement concentration, the reference ISH is compared with a virtual specimen containing uniform steel ratios throughout the entire length of the specimen. This second specimen is characterized by having 24% more steel than the reference ISH.

The normalized load-displacement relationships of the ISHs with concentrated and uniform reinforcement throughout the specimen length are shown in Figure 4.6. It is observed that the strength of the ISH increases only to $1.05C_r$ when the reinforcement ratio is uniform throughout the specimen length. The yield loads are marked with circles in the load-displacement relationships of Figure 4.6. It is observed that the yield load increases from $0.52C_r$ for the case of concentrated reinforcement to $0.57C_r$ for the case of uniform reinforcement. Therefore, it is concluded that concentrating the reinforcement near the bearings is recommended to optimize the ISH design.

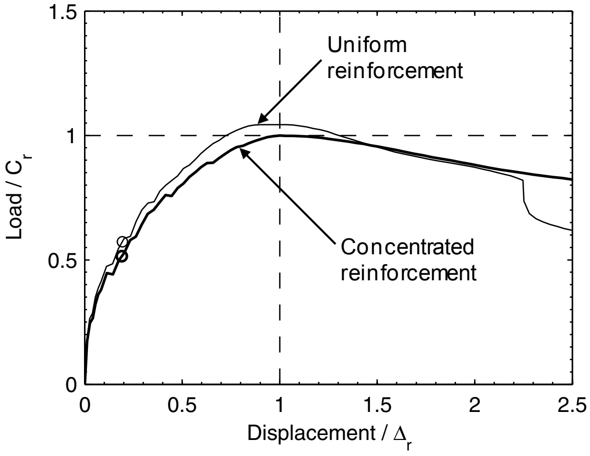

Fig. 4.6 Normalized load-displacement relationships of ISH with concentrated (reference) and uniform reinforcement throughout specimen length.

4.2.2 Diagonal Bars of Seat

The experimental and post-test FEA results revealed that the diagonal bars of the seat are the most critical bars (i.e., bars subjected to the largest strains) of the ISH region. These diagonal bars contribute to the sliding shear, SAT, 1D shear, and punching shear strength mechanisms of the ISH.

From the projects survey, the range of the reinforcement ratio of diagonal bars of the seat varies from ρ_{sd}= 0.20% to 0.30% (see Fig. 4.3). The normalized load-displacement relationships for the ISH with ρ_{sd} varying from 0.0% to 1.0% with an increment of 0.2%, i.e., 6 levels in addition to the reference case, are shown in Figure 4.7a, where the relationship for the reference ratio (ρ_{sd}=0.26%) is shown with a thicker line. The modification in the reinforcement ratios was achieved by changing the cross section of the diagonal bars but keeping the bar spacing constant. Figure 4.7a shows that the strength of the ISH increases from 0.83C_r for ρ_{sd}=0.0% to 1.43C_r for ρ_{sd}=1.0%. However, Figure 4.7a shows that the ductility of the ISH decreases as ρ_{sd} increases above the reference value of 0.26%.

To study different detailing options, the ISH with the diagonal bars of the seat oriented differently from the reference case of 36° is analyzed. The normalized load-displacement relationships for the 5° orientation and the 54° orientation are shown in Figure 4.7b and c, respectively. It is observed that using a steeper orientation increases the strength, where a maximum increase of 11% is observed for reinforcement ratio ρ_{sd}=0.4%, when comparing the 54° and 36° orientations. However, the ductility of the ISH is significantly reduced for the case of 45° and 54° with large values of ρ_{sd}.

The yield loads are marked with circles on the normalized load-displacement relationships of Figure 4.7. For all cases, yielding is initiated in the diagonal reinforcement of the seat. It is observed that the yield load increases as the reinforcement ratio increases, for the three bar orientations. Particularly, for the 36° orientation, the yield load increases from $0.26C_r$ for ρ_{sd}=0.0% to $1.05C_r$ for ρ_{sd}=1.0%.

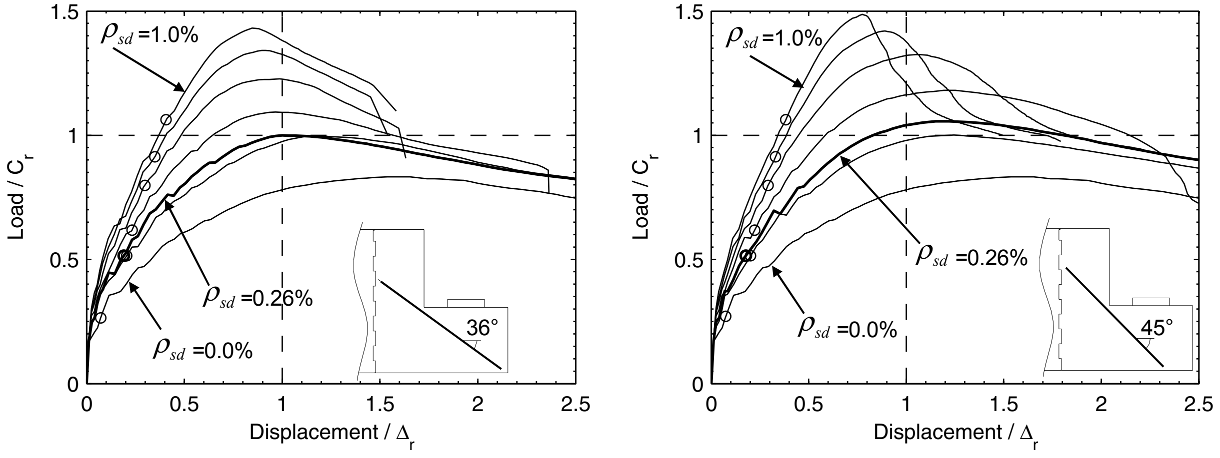

(a) 36° orientation

(b) 45° orientation

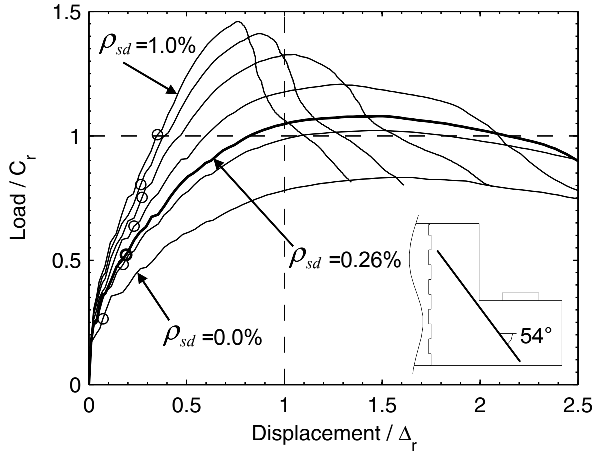

(c) 54° orientation

Fig. 4.7 Normalized load-displacement relationships of ISH with diagonal reinforcement of seat ρ_{sd} = 0.0, 0.2, 0.26 (reference ratio), 0.4, 0.6, 0.8, and 1.0%.

4.2.3 Vertical Bars of Seat

The vertical bars of the seat contribute to the punching shear strength of the ISH. From the projects survey, the range of the reinforcement ratio of these bars varies from ρ_{sv}= 0.24% to 0.92% (see Fig. 4.3). The normalized load-displacement relationships for the ISH with ρ_{sv} varying from 0.0% to 1.0% with an increment of 0.2%, i.e., 6 levels in addition to the reference case, are shown in Figure 4.8a, where the relationship for the reference ratio (ρ_{sv}=0.49%) is shown with a thicker line. Figure 4.8a shows that the strength of the ISH increases from 0.86C_r for ρ_{sv}=0.0% to 1.02C_r for ρ_{sv}=1.0%. However, for a reinforcement ratio of ρ_{sv}=0.2%, a capacity of 0.98C_r is already achieved. Additionally, Figure 4.8a shows that the ductility is not affected by ρ_{sv}.

To study different detailing options, the normalized load-displacement relationships for the ISH with the vertical bars of the seat distributed in two (at 6 in. [152 mm] spacing) and four (at 3 in. (76 mm) spacing) layers are shown in Figure 4.8b and c, respectively. It is observed that the strength and the ductility are improved when the vertical bars of the seat are distributed using more layers. For the reference ratio (ρ_{sv}=0.49%), the strength is increased to 1.14C_r and 1.17C_r for the cases of two and four layers, respectively, compared with the reference case of one layer at the end of the seat. It is concluded that using several layers of vertical bars improves the behavior of the seat by providing a more effective detailing for the punching shear mode of failure. However, this improved behavior was not investigated with the tested specimens.

The yield loads are marked with circles in the normalized load-displacement relationships of Figure 4.8. For all cases, yielding is initiated in the diagonal bars of the seat. Accordingly, it is observed that the yield load is not affected by the ratio ρ_{sv} or by the number of layers of the vertical bars of the seat.

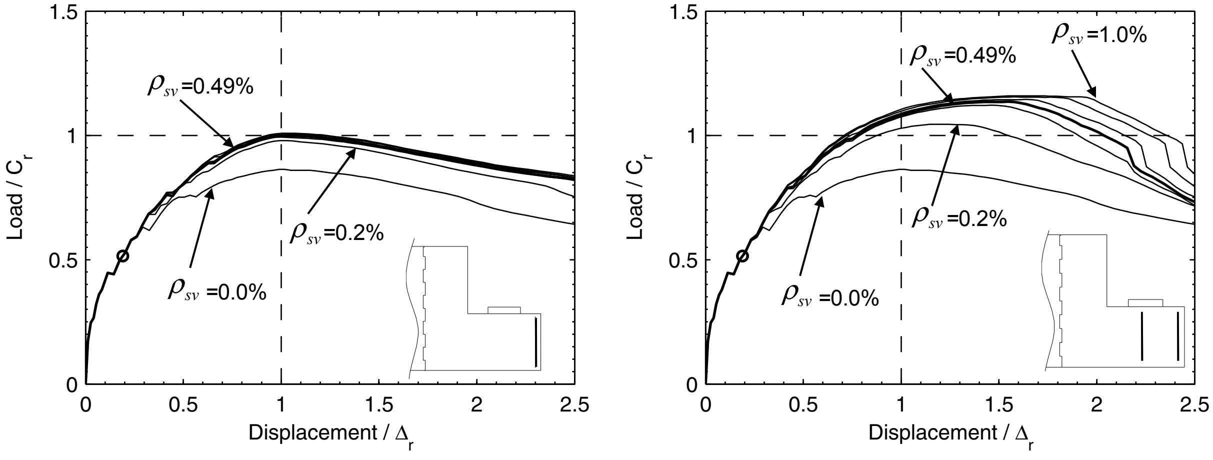

(a) Steel concentrated in one layer

(b) Steel distributed in two layers

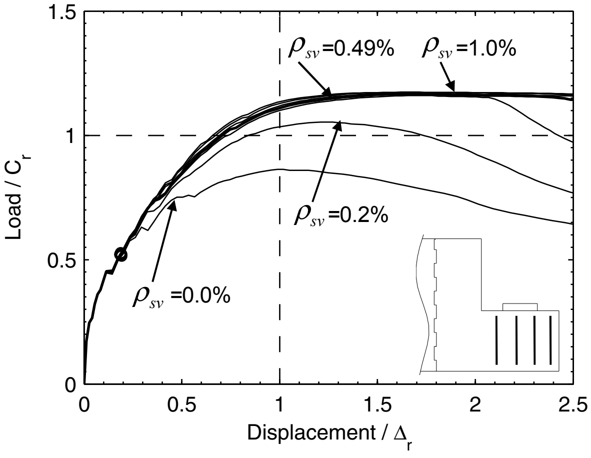

(c) Steel distributed in four layers

Fig. 4.8 Normalized load-displacement relationships of ISH with vertical reinforcement of seat ρ_{sv} = 0.0, 0.2, 0.4, 0.49 (reference ratio), 0.6, 0.8, and 1.0%.

4.2.4 Horizontal Bars of Seat

The horizontal bars of the seat contribute to the sliding shear, the bending, and the SAT strength mechanisms of the ISH. From the projects survey, the range of the reinforcement ratio of these horizontal bars varies from ρ_{sh} = 0.59% to 1.95% (see Fig. 4.3). The normalized load-displacement relationships for the ISH with ρ_{sh} varying from 0.0% to 2.0% with an increment of 0.4%, i.e., 6 levels in addition to the reference case, are shown in Figure 4.9a, where the relationship for the reference ratio (ρ_{sh}=1.17%) is shown with a thicker line. Figure 4.9a shows that the strength of the ISH increases from 0.45C_r for ρ_{sh}=0.0% to 1.03C_r for ρ_{sh}=2.0%.

However, for a reinforcement ratio of ρ_{sh}=0.8%, a capacity of $0.98C_r$ is already achieved. For larger horizontal reinforcement ratios in the seat, the bending failure mode is not critical, and the strength of the ISH is not improved effectively.

To study a different detailing option, the normalized load-displacement relationships for the ISH with the horizontal reinforcement of the seat concentrated in one layer located at the top of the seat is shown in Figure 4.9b. This detailing was used in specimens S4 and S5 of the experimental program. It is observed that the strength and the ductility are compromised when the horizontal bars of the seat are concentrated in one layer. However, for the case of ρ_{sh}=0.4% the strength increases by 16% when one layer is considered.

The yield loads are marked with circles in the normalized load-displacement relationships of Figure 4.9. For all cases, yielding is initiated in the diagonal bars of the seat. When the steel is distributed in three layers, the yield load increases from $0.28C_r$ for ρ_{sh}=0.0% to $0.56C_r$ for ρ_{sh}=2.0%.

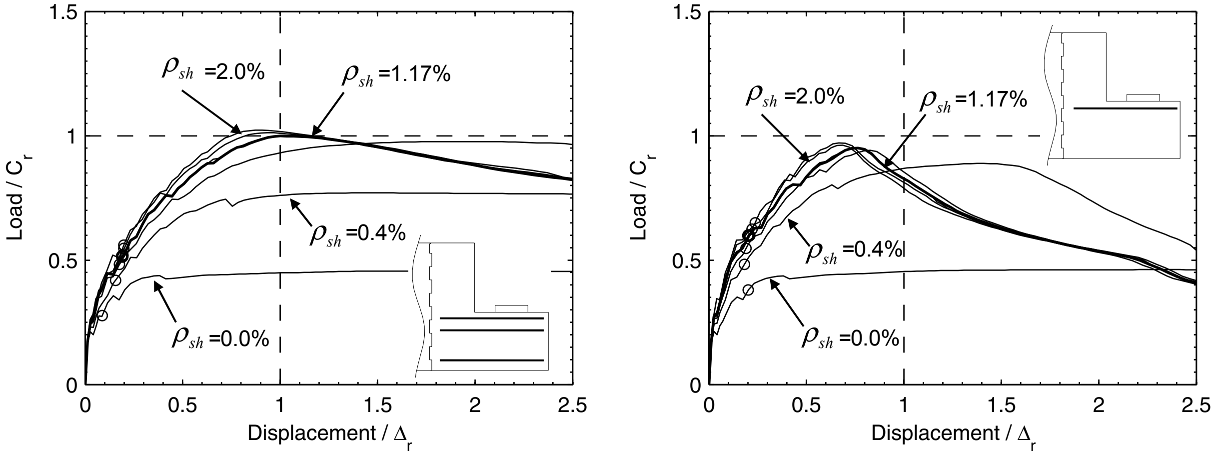

(a) Steel distributed in three layers (b) Steel concentrated in one layer

Fig. 4.9 Normalized load-displacement relationships of ISH with horizontal reinforcement of seat ρ_{sv} = 0.0, 0.4, 0.8, 1.17 (reference ratio), 1.2, 1.6, and 2.0%.

4.2.5 Longitudinal Bars of Seat

The longitudinal bars of the seat contribute to the bending strength of the seat along the longitudinal axis of the bridge. From the project survey, the range of the reinforcement ratio of these longitudinal bars varies from ρ_{slon} = 0.23% to ρ_{slon} = 1.50% (see Fig. 4.3). The normalized load-displacement relationships for the ISH with ρ_{slon} varying from 0.0% to 2.0% with an increment of 0.4%, i.e., 6 levels in addition to the reference case, are shown in Figure 4.10, where the relationship for the reference ratio (ρ_{slon}=0.77%) is shown with a thicker line. Figure 4.10 shows that the strength of the ISH increases from $0.92C_r$ for ρ_{slon}=0.0% to $1.04C_r$ for ρ_{slon}=2.0%. Additionally, it is observed from Figure 4.10 that the ductility is not affected by ρ_{slon}.

The yield loads are marked with circles in the normalized load-displacement relationships of Figure 4.10. For ρ_{slon}≥0.2%, yielding is initiated in the diagonal bars of the seat at $0.52C_r$. For ρ_{slon}=0.0%, yielding is initiated in the longitudinal bars of the seat at $0.37C_r$ (ρ_{slon}=0.0% represents the limit case where longitudinal bars still exist with a very small area). Therefore, it is concluded that a minimum ratio of ρ_{slon}≥0.2% is required to provide adequate yield strength for the ISHs.

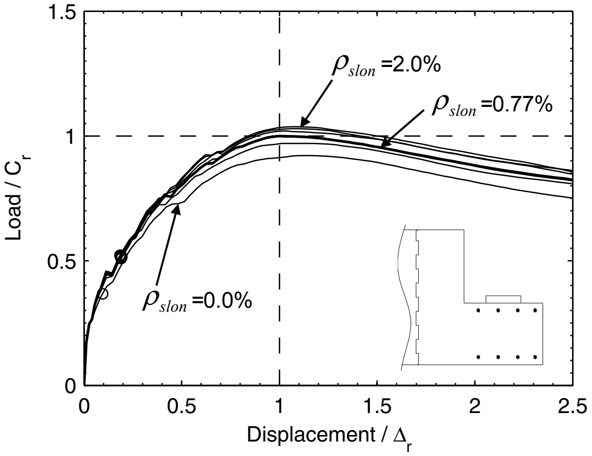

Fig. 4.10 Normalized load-displacement relationships of ISH with longitudinal reinforcement of seat ρ_{slon} = 0.0, 0.4, 0.77 (reference ratio), 0.8, 1.2, 1.6, and 2.0%.

4.2.6 Vertical Bars of Diaphragm

The vertical bars of the diaphragm contribute to the SAT, 1D shear, and punching shear strength mechanisms of the ISH. From the projects survey, the range of the reinforcement ratio of these vertical bars varies from ρ_{dv} = 0.42% to 1.10% (see Fig. 4.3). The normalized load-displacement relationships for the ISH with ρ_{dv} varying from 0.0% to 2.0% with an increment of 0.4%, i.e., 6 levels in addition to the reference case, are shown in Figure 4.11, where the relationship for the reference ratio (ρ_{dv}=1.17%) is shown with a thicker line. Figure 4.11a shows that the strength of the ISH increases from 0.75C_r for ρ_{dv}=0.0%, to 1.12C_r for ρ_{dv}=2.0%. However, the ductility decreases as ρ_{dv} increases. For high values of ρ_{dv}, the strength of the ISH is controlled by a combined 1D shear and punching shear failure modes, where the failure surface of the 1D shear mode is located in the seat between the bearing and the first vertical bar of the diaphragm. This failure surface of the 1D shear mode is observed in Figure 4.12, where the predicted crack pattern is plotted for ρ_{dv}=2.0% at the maximum strength.

To study a different detailing option, the normalized load-displacement relationships for the ISH with the vertical reinforcement of the diaphragm concentrated in one layer is shown in Figure 4.11b. This detailing was used on specimens S4 and S5 of the experimental program. It is observed that the strength increases when the vertical bars of the seat are concentrated in one layer, because the shear force is transmitted more effectively. For the reference ratio (ρ_{dv}=1.17%), the strength of the ISH increases by 12% when concentrating the vertical reinforcement of the diaphragm in one layer compared with the reference case of two layers. However, the maximum strength that can be obtained for ρ_{dv}=2.0% in both cases is similar.

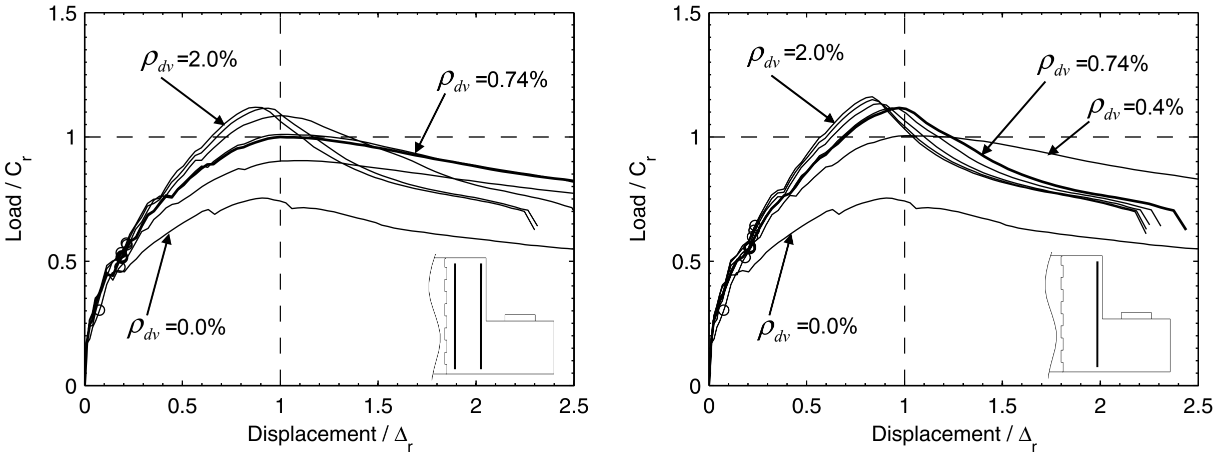

(a) Steel distributed in two layers (b) Steel concentrated in one layer

Fig. 4.11 Normalized load-displacement relationships of ISH with vertical reinforcement of diaphragm ρ_{dv} = 0.0, 0.4, 0.74 (reference ratio), 0.8, 1.2, 1.6, and 2.0%.

The yield loads are marked with circles in the normalized load-displacement relationships of Figure 4.11. For ρ_{dv}≥0.4%, yielding is initiated in the diagonal bars of the seat for both detailing options. For the case of ρ_{dv}=0.0%, yielding is initiated in the vertical bars of the diaphragm at $0.30C_r$ for both detailing options (ρ_{dv}=0.0% represents the limit case where vertical bars still exist with a very small area).

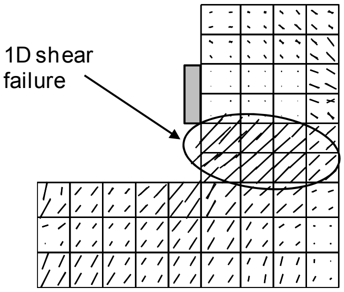

Fig. 4.12 Predicted crack pattern at bearing cross section for ρ_{dv}=2% and steel distributed in two layers (in test orientation).

4.2.7 Horizontal Bars of Diaphragm

The horizontal bars of the diaphragm transfer the horizontal stresses from the seat to the end diaphragm with prestressed blockout. These bars are used to anchor the horizontal bars of the seat and contribute to the sliding shear and bending strength mechanism of the diaphragm. From the projects survey, the range of the reinforcement ratio of these horizontal bars varies from ρ_{dh}= 0.33% to ρ_{dh}= 0.87% (see Fig. 4.3). The normalized load-displacement relationships for the ISH with ρ_{dh} varying from 0.0% to 1.0%, with an increment of 0.2%, i.e., 6 levels in addition to the reference case, are shown in Figure 4.13, where the relationship for the reference ratio (ρ_{dh}=0.56%) is shown with a thicker line. Figure 4.13 shows that the behavior of the ISH is affected only when ρ_{dh}≤0.2% where the strength prediction for ρ_{dh}=0.0% is $0.67C_r$. For this case, the diaphragm is not strong enough to transfer the forces from the seat to the end diaphragm with prestressed blockout.

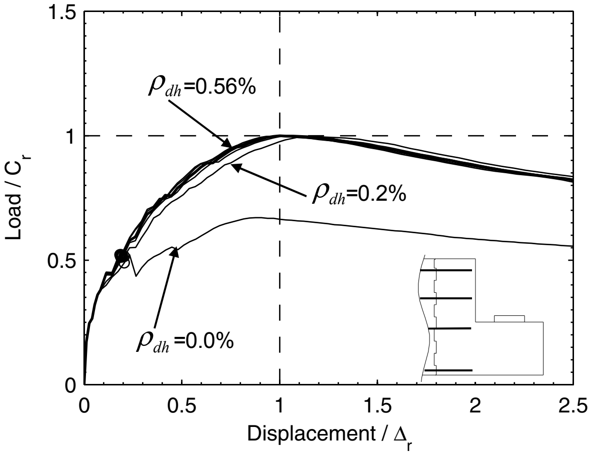

Fig. 4.13 Normalized load-displacement relationships of ISH with horizontal reinforcement of diaphragm ρ_{dh} = 0.0, 0.2, 0.4, 0.56 (reference ratio), 0.6, 0.8, and 1.0%.

4.3 SIZE OF BEARING PLATE

The experimental program revealed that punching shear is one of the critical failure modes of the ISH. To increase the punching shear strength, a larger bearing plate can be used. This idea was incorporated in specimen S3. From the projects survey (Hube and Mosalam 2009), the average bearing plate size for prestressed box-girder bridges is $bp = 0.4b$, where b is the seat width. To prevent local bearing failure, a square bearing plate of $bp = 0.45b$ (i.e., bp =6.0 in. (152 mm)) was used in the experimental program of the specimens with normal bearing size (all specimens except S3). This bearing size was equivalent to $0.14bw$, where bw is the distance between the box webs of the bridge.

To study the effect of the bearing plate area, a parametric study with different bearing plate sizes is conducted. In the longitudinal direction of the bridge, and equivalent to all tested specimens, a bearing size of $ap = 0.14bw$ is considered. In the transverse direction of the bridge, bearing sizes of $bp = 0.14bw$, $0.33bw$, and $0.44bw$ are considered, where the intermediate size ($bp = 0.33bw$) is equivalent to the bearing size of specimen S3. The effect of the bearing area in the normalized load-displacement relationships is shown in Figure 4.14, where the relationship for the reference size ($bp = 0.14bw$) is shown with a thicker line. It is observed that the strength increases to $1.15C_r$ and $1.19C_r$ for the cases of $0.33bw$ and $0.44bw$, respectively. The predicted strength increases for the case of bp=0.33bw and is smaller than that measured in the experimental program, where the capacity of specimen S3 was 26% larger than that of S2.

The predicted crack patterns at the cross section located at the edge of the specimens (i.e., cross section equivalent to section A-A in Fig. 3.12), at displacement of 1.0Δ_r are shown in Figure 4.15. Here the short lines are perpendicular to the crack direction and their lengths are proportional to the crack normal strain (opening mode). It is observed that the crack widths at the edge of the specimen increase as the bearing area increases. Therefore, the load is distributed more uniformly throughout the seat length when a larger bearing area is used. Finally, Figure 4.14 shows that the ductility increases with the use of larger bearing plate. This observation coincides with the experimental results, where specimen S3 with larger bearing plates showed a more ductile behavior than the rest of the specimens with normal size plates (Hube and Mosalam 2009).

The yield loads are marked with circles in the normalized load-displacement relationships of Figure 4.14. It is observed that the yield load increases from 0.52C_r for the case of bp=0.14bw to 0.54C_r when a bearing plate of bp=0.33bw or 0.44bw is used.

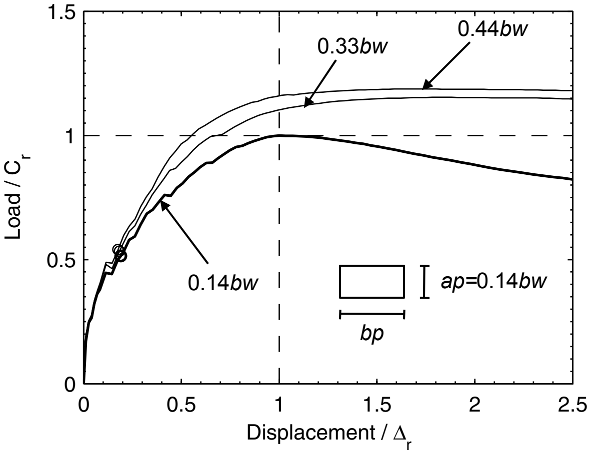

Fig. 4.14 Normalized load-displacement relationships of ISH with size of bearing area bp = 0.14 (reference size), 0.33 and 0.44bw.

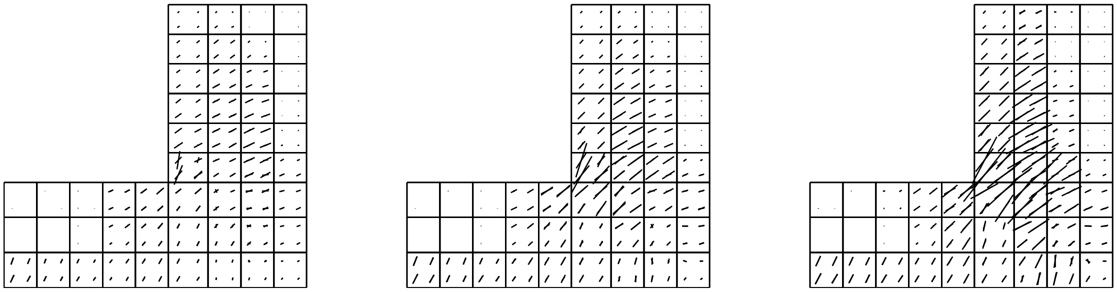
(a) bp =0.14 bw (b) bp =0.33 bw (c) bp =0.44 bw

Fig. 4.15 Predicted crack patterns with different sizes of bearing plates, at cross section located at edge of specimens (in test orientation).

4.4 SEAT ASPECT RATIO

A parametric study of the seat aspect ratio is conducted in this section. The seat aspect ratio is defined as $\alpha = b/h$, where b is the seat width and h is the seat height. The seat aspect ratio of the tested specimens, and the reference ISH, is α =1.29. From the projects survey of ISHs with prestressed box girders, the range of the aspect ratio varies from α =0.62 to α =1.58, and the average aspect ratio is α =1.05.

To study the effect of the aspect ratio, the reference ISH is compared with ISHs of aspect ratios α =0.86 and 1.71. These FE models are obtained by subtracting and adding two rows of elements at the edge of the seat, for the lower and higher aspect ratio, respectively. To keep all the reinforcement ratios constant, the bar areas were adjusted in the cases of α =0.86 and 1.71 due to the modification of concrete volume. The cross sections of the FE models for the three cases are shown in Figure 4.16.

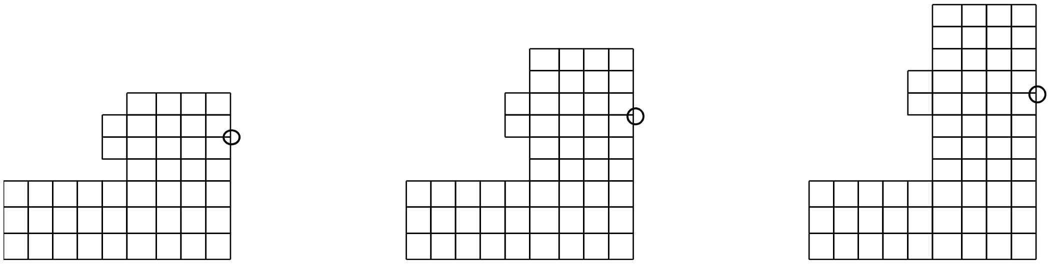
(a) α =0.86 (b) α =1.29 (reference ISH) (c) α =1.71

Fig. 4.16 Cross section of FE model for different aspect ratios (in test orientation, base not shown).

The normalized load-displacement relationships for the ISH with seat aspect ratio α=0.86, 1.29, and 1.71 are shown in Figure 4.17, where the relationship for the reference ratio (α=1.29) is shown with a thicker line. For the three cases, the displacement is measured at the concrete node located in the bearing axis, marked with a circle in Figure 4.16. From the results shown in Figure 4.17, the strength of the ISH increases as the aspect ratio decreases. However, the displacement at peak strength, and the ductility, decrease as the aspect ratio increases. The predicted strengths are 1.08C_r and 0.90C_r for the case of α=0.86 and 1.71, respectively. For the small aspect ratio (α=0.86), larger punching shear cracks are predicted. However, the larger strength prediction for this case may be affected by the concrete base because of the smaller distance between the applied load and the horizontal (in the test orientation) reinforcement of the base. For the large aspect ratio (α=1.71), the bending behavior becomes more relevant, but the strength is reduced because of the absence of shear reinforcement in the seat (vertical reinforcement of the seat in the real orientation) between the bearings and the diaphragm. The described behavior for small and large aspect ratios can be confirmed when observing the principal concrete stresses at the bearing sections in Figure 4.18. In this figure, the compression stresses for the peak load are show for each case of aspect ratio.

The yield loads are marked with circles in the normalized load-displacement relationships of Figure 4.17. For the shown three cases, yielding is initiated in the diagonal bars of the seat (ρ_{sd}). It can be concluded that the diagonal bars are the most critical bars regardless of the value of the value of the aspect ratio.

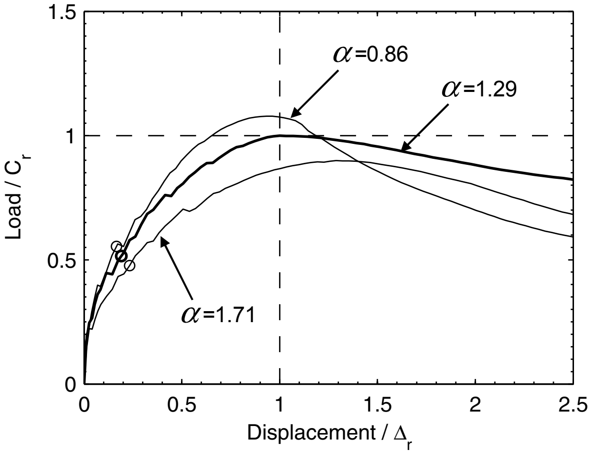

Fig. 4.17 Normalized load-displacement relationships of ISH with seat aspect ratio α = 0.86, 1.29 (reference ratio), and 1.71.

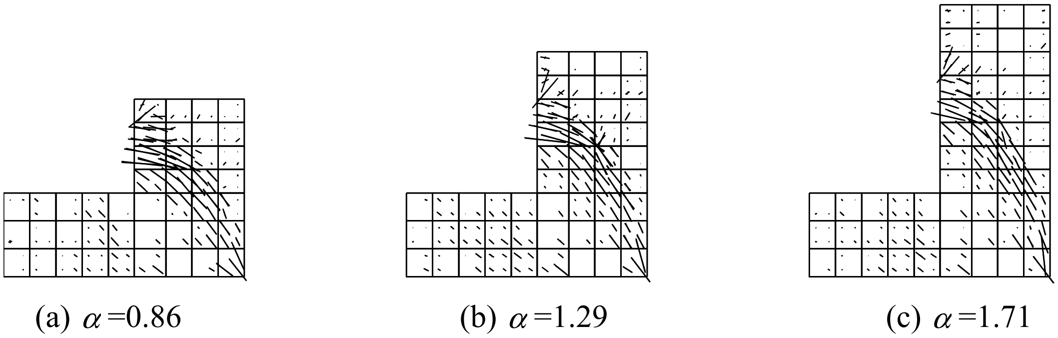
(a) α=0.86 (b) α=1.29 (c) α=1.71

Fig. 4.18 Predicted principal compression stresses of ISH with seat aspect ratio α = 0.86, 1.29 (reference ratio), and 1.71 (in test orientation).

4.5 LOAD ECCENTRICITY

Due to thermal, prestressing, and shrinkage deformation, or due to construction offsets, ISHs can be subjected to load eccentricity when the applied vertical load of the bearing is not centered with respect to the bearing plate, as shown in the insert of Figure 4.19. A second type of eccentricity occurs when the bearing pad is not located at the center of the seat, but the load is centered with respect to the bearing (Hube and Mosalam 2009). The parametric study of this section deals with the first type of eccentricity.

The normalized load-displacement relationships for the ISH with load eccentricity ratio $\eta = e/b =$ 0, -5% and +5% is shown in Figure 4.19, where b is the seat width and e is the distance from the center of the seat to the applied load. It is observed that when the ISH is subjected to a negative eccentricity ratio of η=-5%, the strength is reduced to $0.96C_r$ because stress concentration induces a local bearing failure of the concrete. The deformed shapes at the bearing cross sections for a displacement of $1.1\Delta_r$ are show in Figure 4.20, where the localized bearing failure for η=-5% is shown in Figure 4.20a. This localized bearing deformation was also observed in specimens S4 and S5, which were characterized by having a load eccentricity ratio η=-5% (see Section 3.4.2). When the ISH is subjected to a positive eccentricity ratio η=+5%, the strength is increased to $1.03C_r$ and the displacement at peak strength is increased considerably up to $1.45\Delta_r$. For this case, less shear deformation is predicted at the seat, as shown in Figure 4.20c.

The yield loads are marked with circles in the normalized load-displacement relationships of Figure 4.19. For all cases, yielding occurred in the diagonal bars of the seat. The predicted yield loads are $0.54C_r$, $0.52C_r$, and $0.49C_r$ for η= -5%, 0%, and +5%, respectively. It is concluded that a negative load eccentricity increases the yield load but decreases the strength of the ISH.

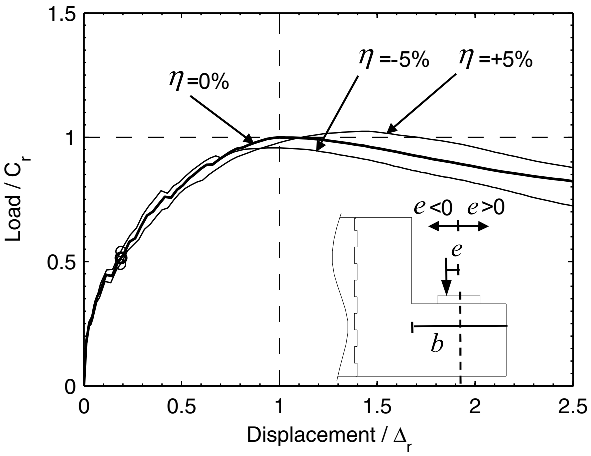

Fig. 4.19 Normalized load-displacement relationships of ISH with load eccentricity η= e/b = -5%, 0% (reference eccentricity), and +5%.

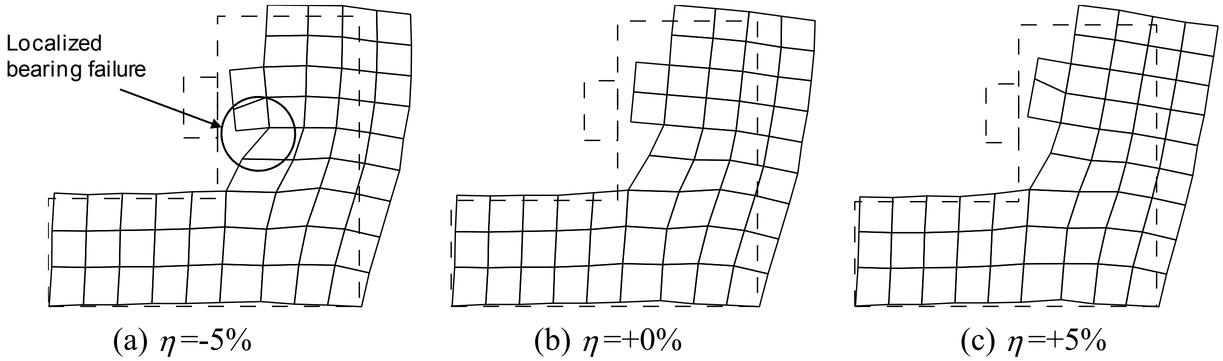

(a) η=-5% (b) η=+0% (c) η=+5%

Fig. 4.20 Predicted deformed shapes at bearing cross section for a displacement of 1.1Δ_r and different values of load eccentricity.

4.6 UTILITY OPENINGS

The utility openings are introduced in the ISH region for maintenance purpose to allow routine inspection of the bearings (Hube and Mosalam 2009). The utility openings allow human access from the interior of the box girder to the seat of the ISH. They are commonly specified between two adjacent bearings, as shown in Figure 4.21. From the projects survey, these openings are located at mid-height or at low-height of the diaphragm. The cross sections of the openings are square, rectangular, or circular, as recommended by the Standard Plan B7-10 of Caltrans (Caltrans 2006). For square or rectangular cross sections, the dimensions recommended by Caltrans are

$$h_{op} = max\{1/3d_h \ , 18\,\text{in.}(457\text{mm})\} \tag{4.1}$$

$$w_{op} = max\{1/3d_h \ , 24\,\text{in.}(610\text{mm})\} \tag{4.2}$$

where h_{op} is the opening height, w_{op} is the opening width, and d_h is the diaphragm height, as shown in Figure 4.21.

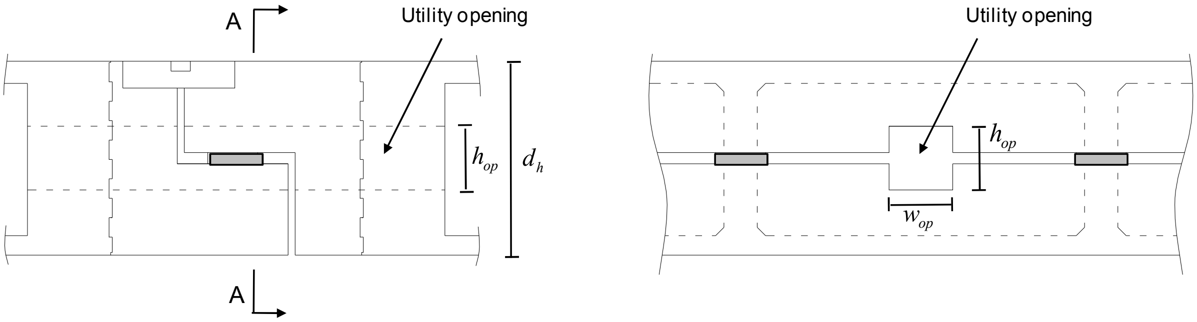

(a) Elevation view (b) Section A-A

Fig. 4.21 Utility opening at mid-height location.

For the experimental program, square openings of $h_{op}=w_{op}=1/3\,d_h$ located at mid-height of the diaphragm were considered in specimens S2, S3, and S5. The utility openings of these scaled specimens satisfy the dimensions requirements of Equations (4.1) and (4.2).

For the parametric study of the utility openings, square and rectangular openings are considered. It is assumed that the circular openings are associated with less stress concentrations than that of rectangular openings. Therefore, circular openings are assumed less critical and are not considered in this parametric study. The variables analyzed in the parametric study of the utility openings are opening locations, opening dimensions, and reinforcement detailing.

4.6.1 Opening Location

The utility openings are located between the bearings at middle or lower height of the diaphragm. These openings are shown in Figure 4.21 and Figure 4.22, for the middle and lower height location, respectively. For an ISH with a lower opening (Fig. 4.22b), if the distance y

between the top of the opening and the seat is less than 8 in. (203 mm), Caltrans recommends extending the top of the utility opening to the top seat edge (Caltrans 2006).

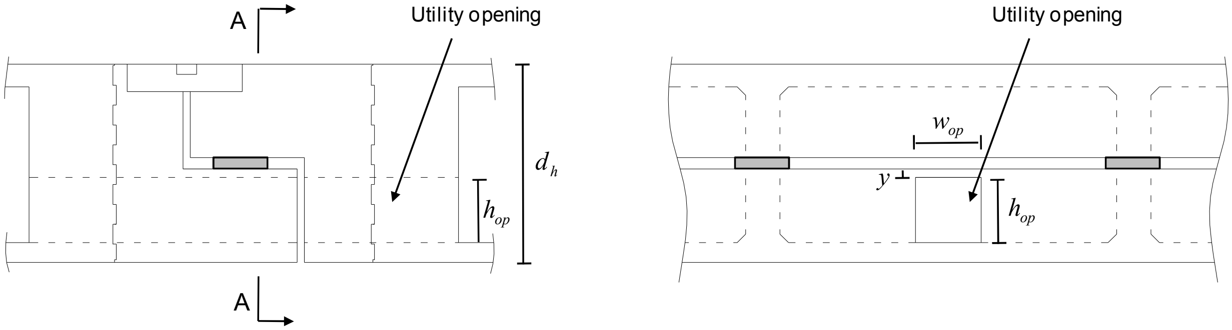

(a) Elevation view (b) Section A-A

Fig. 4.22 Utility opening at low-height location.

To study the effect of the utility opening location, the behaviors of the ISH without and with mid-height and low-height utility openings are compared. For the openings, a square cross section is considered with dimensions $w_{op} = h_{op} = 1/3\, d_h$. For the ISH with a low-height opening location, the opening is considered at the top part of the seat because the scaled specimen does not satisfy the 8 in. (203 mm) distance required by Caltrans. The concrete meshes of the ISH with both types of openings are shown in Figure 4.23. To obtain a conservative estimate of the behavior, all the reinforcing bars located at the seat and diaphragm are terminated at the opening cross section except for the longitudinal bars that are not interrupted by the openings in both cases, as shown in the right insert of Figure 4.24.

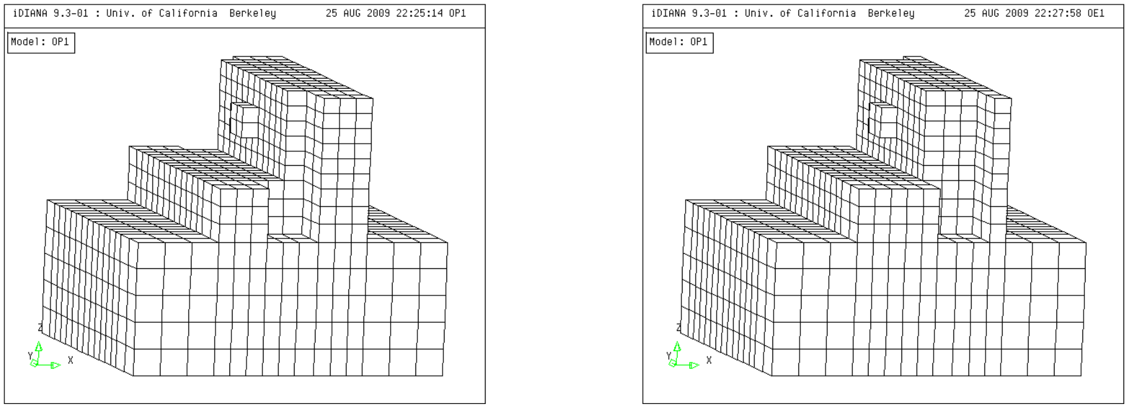

(a) middle location (b) lower location

Fig. 4.23 Concrete mesh for utility opening locations.

The normalized load-displacement relationships for the case without utility openings (reference ISH), with middle, and lower utility openings are shown in Figure 4.24. It is observed that the presence of utility openings reduces the strength to $0.96C_r$ and $0.95C_r$ for the middle and lower locations, respectively. This strength reduction is equivalent to the 5% strength reduction measured in specimen S2 (with middle openings) compared to S1 (without openings).In contrast, a strength reduction was not measured in specimen S5 compared to S4 because their new reinforcement design was found to be less sensitive to the presence of utility openings. From Figure 4.24, it is also observed that the ductility is not affected considerably by the presence or locations of the utility openings.

The yield loads are marked with circles in the normalized load-displacement relationships of Figure 4.24, where yielding is initiated for all cases at the diagonal bars of the seat. It is observed that the presence of utility openings, at either location, reduces the yield load from $0.52C_r$ to $0.45C_r$. This load reduction is equivalent to 13% and is larger than the reduction caused to the load capacity by the openings. This larger reduction of the yield load is attributed to higher influence of the stress concentration caused by the openings at this load level. Finally, based on the behavior observed in Figure 4.24, it is concluded that the opening location does not affect significantly the behavior of ISHs.

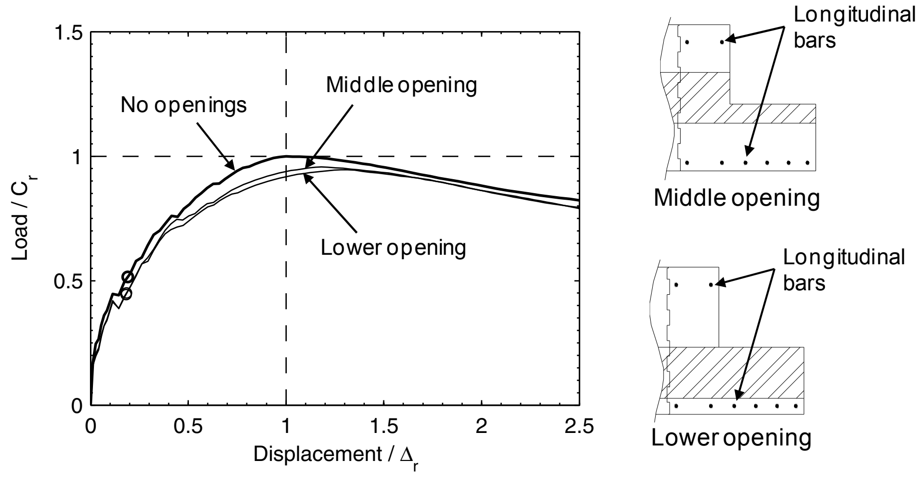

Fig. 4.24 Normalized load-displacement relationships of ISH without utility openings (reference), with middle, and lower utility openings.

4.6.2 Opening Dimensions

The dimensions of the utility openings of the ISHs suggested by Caltrans are given by Equations (4.1) and (4.2). To study the effect of the opening size, a rectangular opening located at mid-height of the diaphragm, with constant height h_{op}=1/3d_h and variable width w_{op} / h_{op}=1.0, 1.7, and 2.5 are considered. The rectangular opening with w_{op} / h_{op}=1.0 is equivalent to the size of the opening of the tested specimens S2, S3, and S5. The cross sections of the ISH with varying opening dimensions are shown in Figure 4.25. The widths of these openings are equivalent to 19%, 32%, and 46% of the spacing between bearings for w_{op} / h_{op}=1.0, 1.7, and 2.5, respectively. To obtain a conservative estimate of the effect of the opening size, all the reinforcing bars located at the seat and diaphragm are terminated at the opening cross section, except for the longitudinal bars that are not interrupted by the openings, shown in the top insert of Figure 4.24.

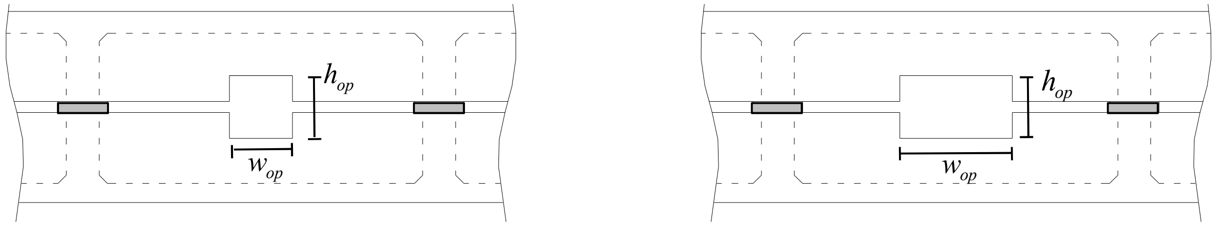

(a) w_{op} / h_{op}=1.0 (b) w_{op} / h_{op}=1.7

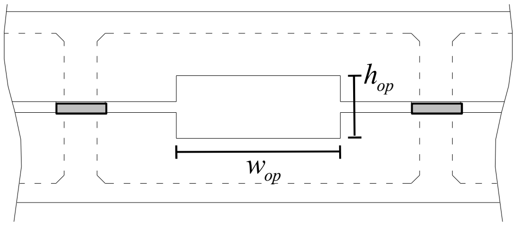

(c) w_{op} / h_{op}=2.5

Fig. 4.25 Cross section of ISH with varying utility opening dimensions.

The normalized load-displacement relationships for the ISH with varying utility opening size are shown in Figure 4.26. The reference ISH, characterized by not having utility openings, is shown with a thicker line. It is observed that the strength of the ISH decreases as the opening size increases, where predicted strength values are 0.96C_r, 0.83C_r, and 0.63C_r for the cases of w_{op} / h_{op}=1.0, 1.7, and 2.5, respectively. However, Figure 4.26 shows that the ductility increases as the opening size increases, because the punching shear failure mode becomes less critical. The predicted crack patterns at the edge of the seat (section B-B) for the ISH with the three opening sizes are shown in Figure 4.27, at displacement of $1.0\Delta_r$. It is observed that the punching shear cracks are reduced significantly as the opening size increases.

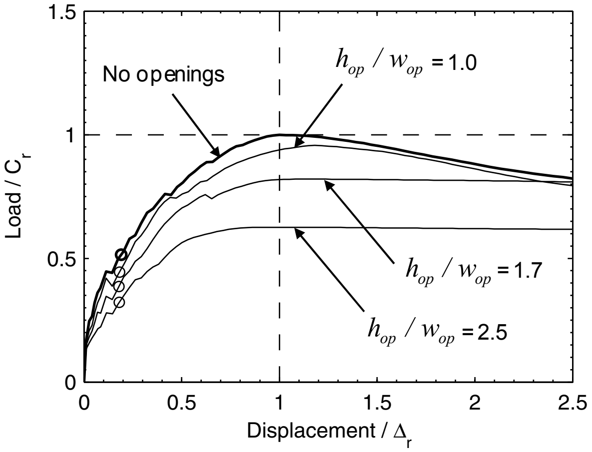

Fig. 4.26 Normalized load-displacement relationships of ISH with varying utility opening dimensions.

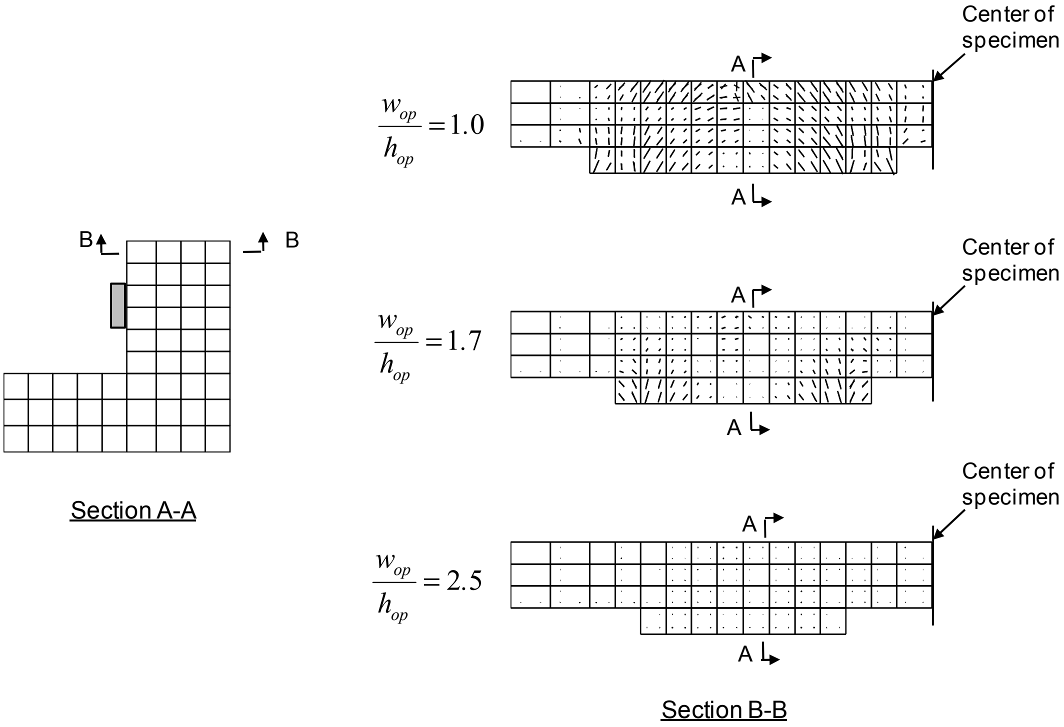

Fig. 4.27 Predicted crack patterns of ISH with varying utility opening dimensions (in test orientation).

The yield loads are marked with circles in the normalized load-displacement relationships of Figure 4.26, where yielding is initiated for all cases at the diagonal bars of the seat. It is observed that the yield load decreases as the opening size increases. Finally, it is concluded that the utility opening size is critical for the behavior, the strength, the ductility, and the failure mode of the ISH.

4.6.3 Reinforcement Detailing

The parametric study of the opening location and dimensions described previously is conducted neglecting most of the reinforcement located near the openings. The strength reduction predicted by the virtual specimen with square openings, located at the mid-height of the diaphragm (Fig. 4.21), is comparable to the strength reduction measured from the tests, when the strength of specimen S2 is compared to S1. However, specimen S2 was characterized by having reinforcement near the openings (Hube and Mosalam 2009). The fact that the reduction of strength of the virtual specimen is comparable to the strength reduction measured in the test suggests that the reinforcement near the opening is not critical for the behavior and the strength of the ISH. Nevertheless, this reinforcement is recommended to control cracking due to stress concentration near the openings.

In this section, the reinforcement detailing near the utility opening is analyzed. The utility openings considered have square cross sections of dimension $w_{op}=h_{op}=1/3\,d_h$ and are located at the mid-height of the diaphragm. These dimensions are consistent with the utility openings used in the experimental program.

To understand the reinforcement requirements at the opening locations, Figure 4.28 shows vertical and horizontal (in the test orientation) cross sections of the predicted crack patterns of the virtual specimen at the peak load. The corresponding normalized load-displacement relationship is shown in Figure 4.24, for the mid-height case. The short lines in Figure 4.28 are perpendicular to the crack direction, and their lengths are proportional to the crack normal strain (opening mode). These predicted cracks agree with the observed cracks of the tested specimens near the utility openings. The predicted directions of the largest cracks, at the cross section of the center opening, of the virtual specimen are shown in section B-B of Figure 4.28. These cracks also have a strain component in the direction longitudinal to the diaphragm (i.e., normal to section B-B), as shown in sections C-C and D-D of Figure 4.28. At the peak load, the largest crack strain (crack opening normalized by the crack band width as discussed in Chapters 2) predicted at an integration point is 1.60% (about 8 times the steel yield strain) and 1.23% (about 6 times the steel yield strain) for the cross sections A-A and B-B, respectively.

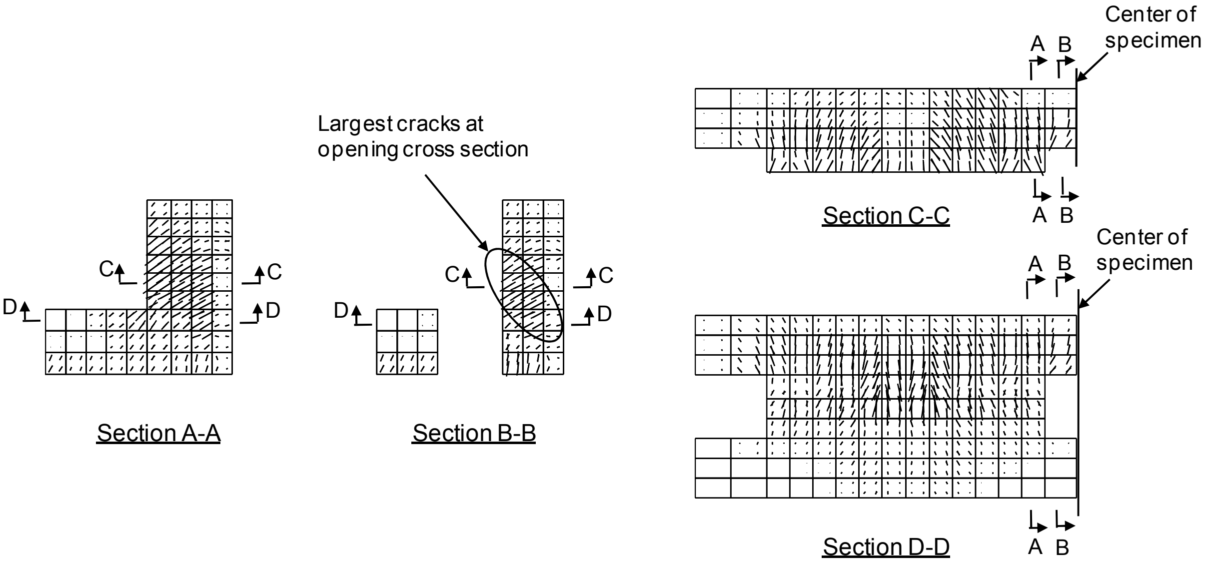

Fig. 4.28 Predicted crack patterns of ISH near openings, D1 detailing defined in Table 4.1 (in test orientation).

The representative reinforcement detailing near the utility openings is obtained from the projects survey. Additionally, the Standard Plan B7-10 (Caltrans 2006) suggests reinforcement detailing for square and circular utility openings located at low-height of the diaphragm, for the case of non-prestressed box-girder bridges. The reinforcement within the utility opening region consists of (a) longitudinal bars in the seat and diaphragm (shown in the insert of Fig. 4.24); (b) vertical and horizontal bars of the seat and diaphragm at the opening cross section; (c) longitudinal bars around the opening; and (d) additional (concentrated) diagonal, vertical, and horizontal bars at the opening sides. These reinforcements are shown in Figure 4.29 for a utility opening located at mid-height of the diaphragm.

To study the effect of the reinforcement detailing near the utility openings, 9 virtual specimens are analyzed. The reinforcement characteristics of these specimens are listed in Table 4.2. The reinforcing steel ratios within the opening region are identical to the steel ratios of the reference specimen, beyond the bearings region (values of Table 4.1 multiplied by 0.66). For the cases of additional bars at the sides of the opening, the corresponding bars interrupted by the openings are relocated to the opening sides, such that the total number of bars is equivalent to the number of bars of an ISH without openings. For the longitudinal bars around the openings, a reinforcing steel ratio of 0.1% is considered (area of steel divided by the diaphragm concrete area in section B-B of Fig. 4.29). This ratio is consistent with the Standard Plan B7-10 (Caltrans 2006).

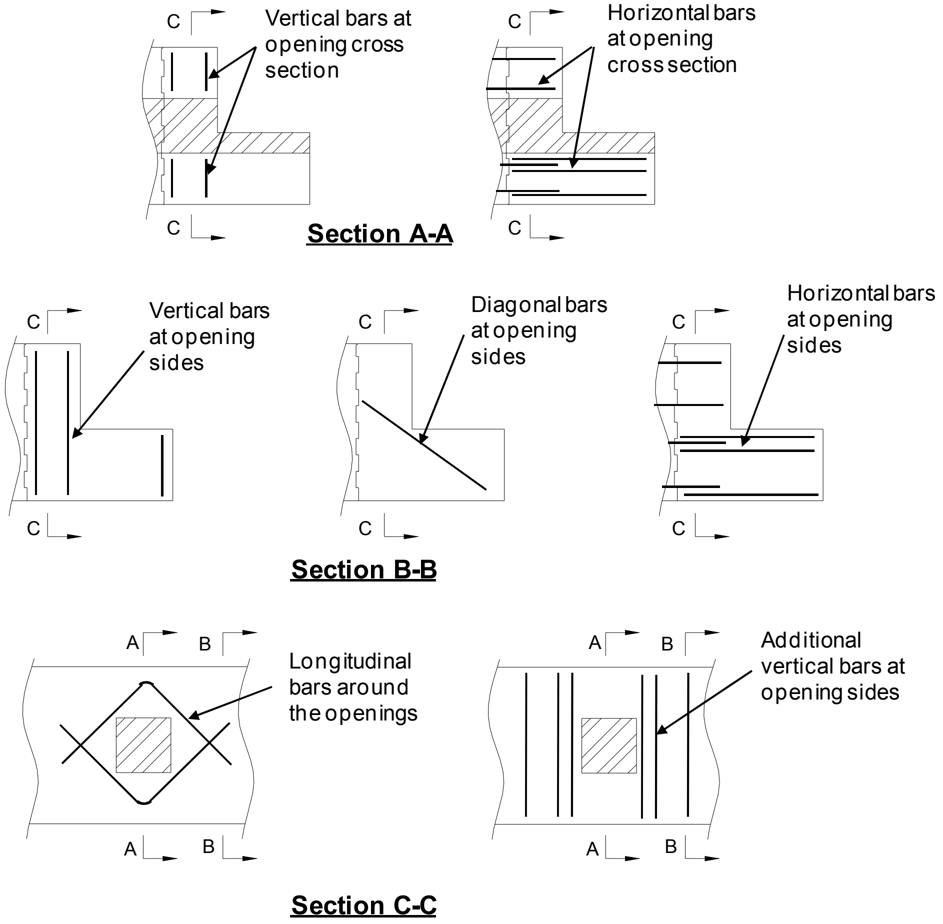

Fig. 4.29 Reinforcement detailing near utility openings.

The results of the parametric study related to the reinforcement detailing near the utility openings are summarized in Table 4.2, together with the identification of the considered cases of the reinforcement detailing in this study. It is observed that the most effective bars to increase the strength of the ISH are the additional vertical and diagonal bars located adjacent to the utility openings. This result is consistent with the crack pattern predicted near the opening for the case D1, section A-A of Figure 4.28. Using these bars, the strength of the ISH is increased from $0.96C_r$ to $0.98C_r$, and $0.99C_r$ for the cases of diagonal (Case D5) and vertical (Case D6) bars, respectively. If both types of reinforcement are utilized simultaneously (case D8), the strength is increased to $1.00 C_r$, which is the strength of the ISH without openings. However, the yield load for the case D8 is equivalent to $0.48 C_r$, which is 7% lower than the yield load of the reference ISH (i.e., $0.52 C_r$). The maximum crack strains at the cross sections either adjacent to or through the utility opening are tabulated in Table 4.2. It is observed that the longitudinal bars surrounding the openings are the most effective bars to reduce the crack strains at the section through the utility openings.

Table 4.2 Parametric study of reinforcement detailing near utility openings.

Case	D1	D2	D3	D4	D5	D6	D7	D8	D9
Vertical bars at opening cross section	-	Yes	-	-	-	-	-	-	-
Horizontal bars at opening cross section	-	-	Yes	-	-	-	-	-	-
Longitudinal bars surrounding the opening	-	-	-	Yes	-	-	-	-	Yes
Additional diagonal bars at opening sides	-	-	-	-	Yes	-	-	Yes	Yes
Additional vertical bars at opening sides	-	-	-	-	-	Yes	-	Yes	Yes
Additional horizontal bars at opening sides	-	-	-	-	-	-	Yes	-	-
Strength [C_r]	**0.96**	**0.97**	**0.96**	**0.97**	**0.98**	**0.99**	**0.97**	**1.00**	**1.00**
Yield load [C_r]	**0.45**	**0.45**	**0.46**	**0.45**	**0.46**	**0.46**	**0.46**	**0.48**	**0.48**
Crack strain #1 † [%]	1.60	1.53	1.46	1.68	1.43	1.55	1.64	1.38	1.28
Crack strain #2‡ [%]	1.23	1.20	1.66	0.86	1.10	1.04	1.22	0.81	0.82

† Maximum concrete crack strain in section adjacent to utility opening (Section A-A in Fig. 4.28).
‡ Maximum concrete crack strain in section through utility opening (Section B-B in Fig. 4.28).

The normalized load-displacement relationship of the ISH with opening reinforcement detailing cases D1 and D9 are shown in Figure 4.30. Additionally, Figure 4.30 shows the relationship for the reference ISH, characterized by not having utility openings. It can be concluded that using additional vertical and diagonal bars at the opening sides, and using longitudinal bars surrounding the opening (case D9), the behavior of the ISH is almost identical to an ISH without openings. However, it is recommended to keep the horizontal bars of the diaphragm in the opening cross section, to provide better anchorage between the diaphragm and the end diaphragm with prestressed blockout (see Fig. 4.2).

For ISHs with larger openings, the reinforcement detailing near the opening is more critical. The normalized load-displacement relationships of an ISH with opening width $w_{op}=1.7\,h_{op}$ (equivalent to 32% of the spacing between bearings) and with detailing D1 and D9 are shown in Figure 4.31. It can be observed that the predicted strength is increased from $0.83\,C_r$ for detailing D1 to 1.00 for detailing D9. Therefore, providing adequate reinforcement near the opening, the reduction of strength due to the existence of the opening can be eliminated. Moreover, Figure 4.31 shows that for this larger opening size, the ductility with detailing D9 is larger than that for an ISH without opening. It is to be noted that for this larger opening size, the punching shear failure mode becomes less critical.

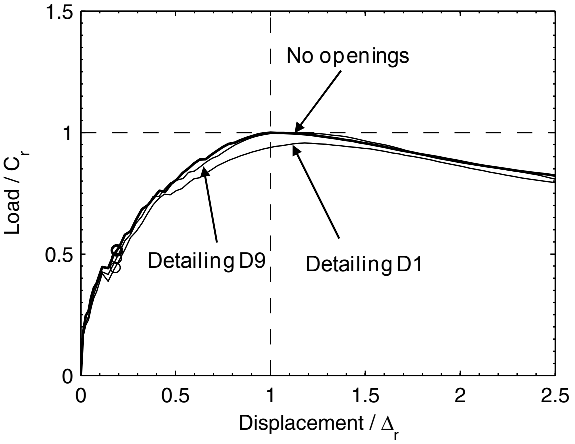

Fig. 4.30 Normalized load-displacement relationships of ISH with reference opening (w_{op} / h_{op} =1.0) and different reinforcement detailing near openings.

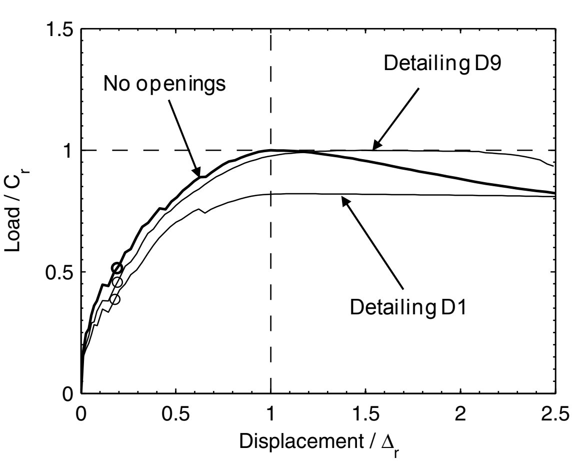

Fig. 4.31 Normalized load-displacement relationships of ISH with larger opening (w_{op} / h_{op} =1.7) and different reinforcement detailing near openings.

5 Design Recommendations

The design recommendations presented in this chapter are applicable to the ISH of RC box-girder bridges when subjected to vertical loads through the bearings. The cross section and the reinforcement designation of the ISH are shown in Figure 5.1. It is assumed that an end diaphragm with prestressed blockout is not a critical element of the ISH and is therefore excluded from this study. In Figure 5.1 ρ_{sd}, ρ_{sv}, ρ_{sh}, and ρ_{slon} represent the diagonal, vertical, horizontal, and longitudinal reinforcing steel ratios of the seat, respectively. Also in Figure 5.1, ρ_{dv}, ρ_{dh}, and ρ_{dlon} represent the vertical, horizontal, and longitudinal reinforcing steel ratios of the diaphragm, respectively. These reinforcing steel ratios are defined in Equation (2.4) in Hube and Mosalam (2009). It is to be noted that the ISH should be designed according to the Caltrans Bridge Design Specifications (Caltrans 2004) and the specific project design criteria.

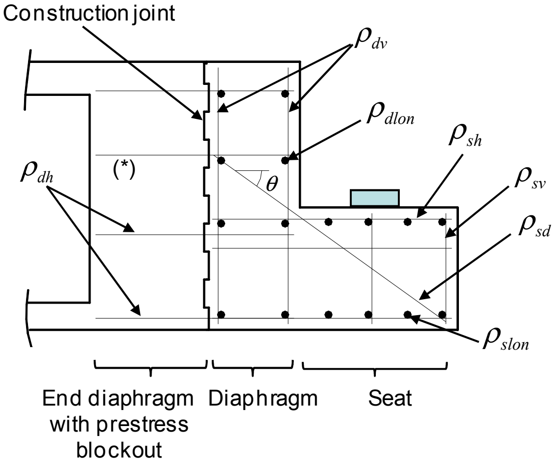

Fig. 5.1 Cross section and reinforcement steel designations of ISH of prestressed box-girder bridges.

5.1 STRENGTH ESTIMATION

Based on the experimental and analytical results, it is concluded that the ISH fails with a combination of three failure modes when it is subjected to vertical loads though the bearings: (1) one-dimensional (1D) shear, (2) two-dimensional (2D) strut-and-tie (SAT), and (3) punching shear. Therefore, the ISH design must consider these failure modes and their combination, in addition to the bending and the sliding shear modes typically considered in the design approach of short cantilevers (Hube and Mosalam 2009). Accordingly, it is recommended to obtain the strength of the ISH using all of the following design criteria:

(a) Sliding shear friction
(b) Bending moment
(c) 2D SAT
(d) 1D shear
(e) Punching shear

Additionally, it is recommended to check the concrete bearing failure at the locations of the bearing plates to avoid localized concrete failure, e.g., using ACI318 (2008) requirements in Section 10.14. The details of the listed design models above, with the corresponding design equations, were introduced in details in Hube and Mosalam (2009). The design equations are based on the ACI code (2008) and on the Bridge Design Specifications (Caltrans 2004). When utility openings are present, the reduction of the concrete section and the possible reduction of reinforcing steel have to be incorporated in the capacity estimation. Additional design recommendations for each of the design criteria are described below.

The sliding shear friction and the bending moment have to be computed at the seat and at the diaphragm, as shown in Figure 5.2. The critical section of the diaphragm coincides with the concrete junction of the diaphragm. To obtain the sliding shear friction, or bending moment strength of the ISH, a section width equal to the total length of the diaphragm should be considered.

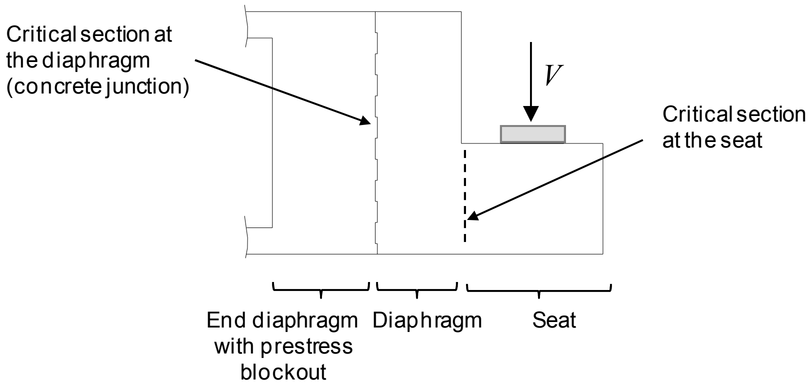

Fig. 5.2 Critical sections for sliding shear and bending moment.

The proposed 2D SAT model provides a good capacity estimate for the ISH. This model assumes that the bearing load is distributed uniformly through the bridge width, and neglects the 3D effect caused by the concentrated load at the bearing locations. The proposed SAT is shown in Figure 5.3 where continuous and dashed lines represent tension ties and compression struts, respectively. The thickness of this truss considers the total diaphragm length; the steel area of each tie is the sum of the bars along the bridge width. The proposed truss is statically indeterminate, but the capacity is obtained assuming that the vertical bars of the diaphragm (ρ_{dv}) and the diagonal bars of the seat (ρ_{dv}) are yielding simultaneously. Therefore, the SAT capacity for the ISH is given by

$$V_n = A_{dv} f_y + A_{sd} f_y \, sin(\theta) \tag{5.1}$$

where A_{dv} is the area of steel of the vertical bars of the diaphragm, A_{sd} is the area of steel of the diagonal bars of the seat, θ is the orientation of these diagonal bars (Fig. 5.1), and f_y is the yield stress of the steel. In order to obtain the capacity given by Equation (5.1), equilibrium requirements must be satisfied. The amount of reinforcing steel in ties BA and HI must be sufficient to satisfy the equilibrium at nodes A and I, respectively. Additionally, the amount of horizontal reinforcing steel located near node K in the diaphragm (marked with (*) in Fig. 5.1) must be sufficient to transfer the horizontal component of the diagonal tie KF at node K.

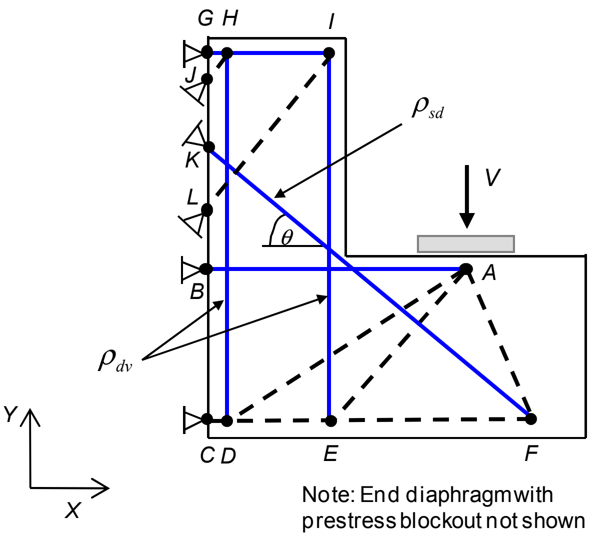

Note: End diaphragm with prestress blockout not shown

Fig. 5.3 Proposed 2D SAT of ISH.

The geometry of the proposed 2D SAT model (Fig. 5.3) is determined using the following procedure. The X coordinate of node A is centered with respect to the bearing, and the Y coordinate coincides with the location of the upper horizontal reinforcing steel of the seat (ρ_{sh} in Fig. 5.1). The tie AB is fixed at node B, which has its coordinate coinciding with the concrete junction of the diaphragm. Note that tie AB is not physically fixed at B, but it is assumed that the stress from the horizontal bars of the seat (ρ_{sh}) is transferred to the horizontal bars of the diaphragm (ρ_{dh}) using adequate lap splices. The nodes D and E are located at the bottom end of the vertical bars of the diaphragm (ρ_{dv}), and node F is located at the bottom end of the diagonal bar (ρ_{sd}). The nodes H and I are located at the intersection of the vertical bars of the diaphragm (ρ_{dv}) with the upper horizontal bar of the diaphragm (ρ_{dh}). Node K is located at the top end of the diagonal bars of the seat, which are oriented with an angle α. Note that the diagonal bars of the seat do not extend beyond the construction joint, whereas the horizontal bars of the diaphragm (ρ_{dh}) marked with (*) in Figure 5.1 transfer the horizontal component of the stress to the end diaphragm with prestress blockout. Finally, nodes J and L are obtained considering 45° compression strut from nodes H and I, respectively.

For the 1D shear failure mode shown in Fig. 5.4, the capacity of the ISH is obtained assuming a width equal to the whole diaphragm length. The distance d, in Fig. 5.4, corresponds to the effective depth of the seat assuming a 45° inclination of the shear plane. The total shear resistance (V_n) is the sum of the contributions from the concrete (V_c) and the transverse reinforcing steel (V_s). The reinforcing steel bars that contribute to V_s are the diagonal bars of the seat (ρ_{sd}) and the vertical bars of the diaphragm (ρ_{dv}) that cross the shear plane in Figure 5.4. According to ACI code (2008), the contribution of diagonal reinforcement has to be limited to $V_{sdiag} = 3\sqrt{f_c'} b_w d$ (psi units), where b_w is the concrete width. For the 1D shear failure mode, the contribution of the vertical reinforcement bars of the seat (ρ_{sv}) is neglected because it is assumed that they mainly contribute to the punching shear failure mode.

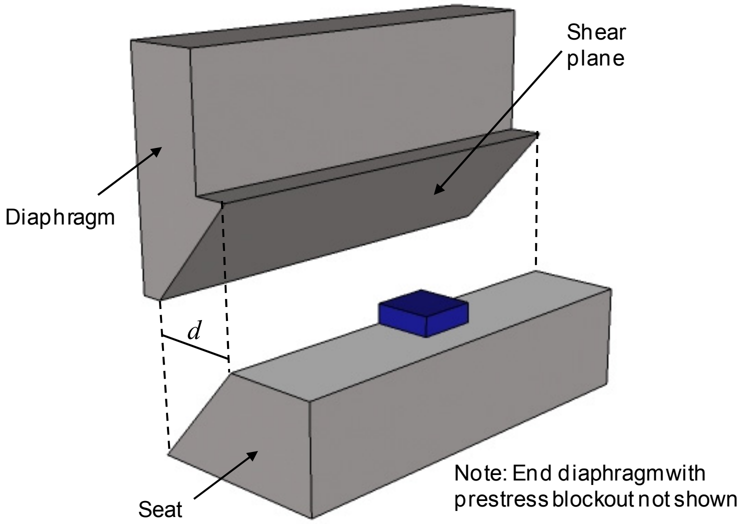

Fig. 5.4 1D shear failure mode of ISH.

The punching shear failure mode is shown in Figure 5.5, where the distance d corresponds to the effective depth of the seat. The total punching shear resistance (V_n) is the sum of the contributions from the concrete (V_c) and the transverse reinforcing steel (V_s). The contribution from the concrete is obtained using the critical perimeter b_o defined in Section 2.4 of (Hube and Mosalam 2009). On the other hand, the contribution from the steel is obtained from the transverse bars that cross the three shear planes of the punching shear cone in Figure 5.5. From the two shear planes on the sides, the vertical bars of the seat (ρ_{sv}) are considered. From the shear plane on the back, the diagonal bars of the seat (ρ_{ds}) and vertical bars of the diaphragm (ρ_{vd}) are considered.

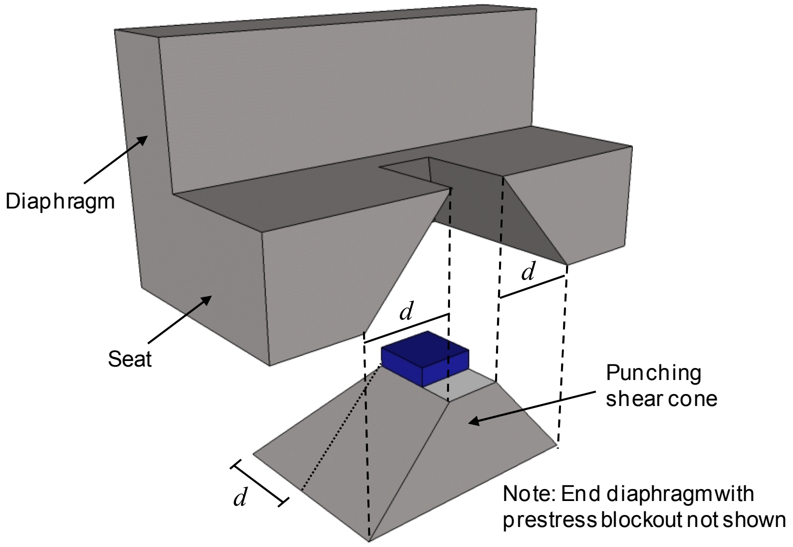

Fig. 5.5 Punching shear failure mode of ISH.

Using the described design models, the experimental capacity versus computed capacity (E/C) ratios of the five tested specimens are obtained in Section 6.9 of (Hube and Mosalam 2009). The experimental capacity (referred to as demand in Hube and Mosalam [2009]) of the specimens is loosely defined as the maximum strength obtained from each test, and the computed capacity corresponds to the strength computed using the described design models. The E/C ratios for the five tested specimens are summarized in Figure 5.6. In this figure, SS_s is for the sliding shear of the seat, SS_d is for the sliding shear of the diaphragm, B_s is for the bending moment of the seat, B_d is for the bending moment of the diaphragm, SAT is for the 2D strut-and tie, and S is for the 1D shear. For the punching shear case, two ratios are shown: PS, computed for $V_n = V_c + V_s$, and PS_{max}, computed for the punching shear limit of $V_n = 6\sqrt{f_c'}b_o d$. Finally, the case labeled as Max corresponds to the critical E/C ratio for each specimen, obtained from the largest ratio of all the failure modes. From Figure 5.6, it is observed that the critical cases (with E/C larger than 1.0) are the SAT, the 1D shear, and the punching shear modes of failure. This result agrees with the experimental observations, where a combined failure from these three modes was observed.

For the virtual specimens used in the parametric study, the corresponding E/C ratios are shown in Figure 5.7. A total of 38 virtual specimens are considered, where specimens that have reinforcement ratios within the surveyed range (see Section 4.2) are included. For the virtual specimens with utility openings, only the specimens with detailing types D1 and D9 (see Table

4.2) are considered. More details of the capacity estimates for the virtual specimens are available in Appendix A. Because of the absence of experimental results, the experimental capacity of each virtual specimen is defined as the maximum strength predicted by the FEA. Similar to the experimental specimens, Figure 5.7 shows that the critical cases are the SAT, the 1D shear, and the punching shear mode of failures. In addition, for two virtual specimens, the ratios for bending of the seat and for bending of the diaphragm are also larger than 1.0.

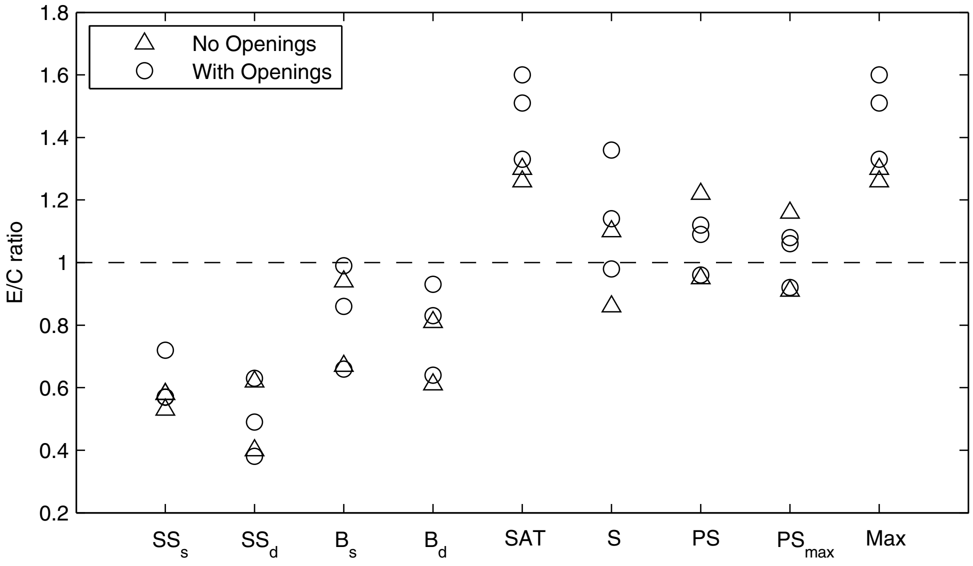

Fig. 5.6 E/C ratio of experimental specimens.

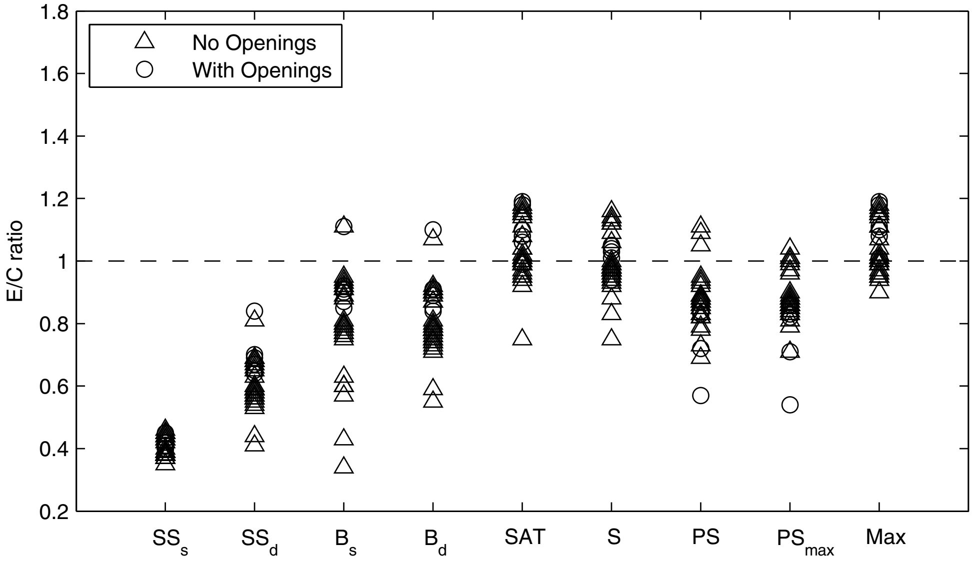

Fig. 5.7 E/C ratio of virtual specimens of parametric study.

The E/C ratios of the experimental and virtual specimens, shown respectively in Figure 5.6 and Figure 5.7, are summarized in Table 5.1. When the ISH is designed using all the described failure modes (column Max in Table 5.1), the mean E/C ratios are 1.40 and 1.05 for the experimental and virtual specimens, respectively. Therefore, a conservative strength estimate of the ISH is obtained in both cases. The corresponding coefficients of variations (cov) are 0.10 and 0.08 for the experimental and virtual specimens, respectively (Table 5.1). For the experimental specimens, the strength of the ISH is controlled in all cases by the SAT design criteria, whereas for the virtual specimens, 79% of the cases are controlled by SAT, 8% by bending of the seat (for large aspect ratio or low ρ_{sh}), 5% by 1D shear (for low ρ_{dv}), 5% by punching shear (for small aspect ratio or uniform reinforcement distribution), and 3% by bending of the diaphragm (for small ρ_{dh}). The difference between the strength estimates of the experimental and virtual specimens is mainly caused by the higher concrete strength of the experimental specimens, which increases the ISH strength considerably (as shown in Section 2.4.2), but does not increase the SAT capacity estimation. For the virtual specimens, the lowest E/C ratio of 0.90 is obtained for the virtual specimen with uniform reinforcement distribution through the specimen length. This type of reinforcement distribution is not recommended in ISHs (see Section 5.2).

Table 5.1 E/C ratio of experimental and virtual specimens.

			SS_s	SS_d	B_s	B_d	SAT	S	PS	PS_{max}	Max
Test	All cases	Mean	0.59	0.50	0.83	0.76	1.40	1.09	1.07	1.03	**1.40**
		Cov	0.13	0.24	0.18	0.18	0.10	0.17	0.11	0.11	**0.10**
	No openings	Mean	0.55	0.51	0.81	0.71	1.28	0.98	1.09	1.03	**1.28**
	With openings	Mean	0.62	0.50	0.84	0.80	1.48	1.16	1.06	1.02	**1.48**
Parametric	All cases	Mean	0.41	0.62	0.81	0.82	1.04	1.00	0.86	0.87	**1.05**
		Cov	0.07	0.13	0.19	0.13	0.09	0.09	0.11	0.11	**0.08**
	No openings	Mean	0.40	0.60	0.79	0.80	1.02	1.00	0.88	0.89	**1.03**
	With openings	Mean	0.41	0.70	0.92	0.92	1.10	1.02	0.79	0.77	**1.11**

For the ISHs that contain utility openings, the mean values of the E/C ratio are 1.48 and 1.11, for the experimental and virtual specimens, respectively (see Table 5.1). Therefore, the capacity prediction of ISHs with openings is more conservative than for ISHs without openings. In fact, the region where the openings are located is away from the bearing area and does not significantly affect the actual strength (from experiments or FEA) of the ISH, but it does reduce the capacity estimate from the different models discussed above.

For service loads levels, yielding of the ISH starts in the diagonal bars of the seat for all the experimental and virtual specimens considered. The yield load for all these cases is shown in Figure 5.8, normalized by the maximum strength of each specimen. It is observed that yielding is initiated at an average load of 55% and 50% of the maximum strength for the experimental and virtual specimens, respectively. The minimum yield load corresponds to 44% of the maximum strength for specimen S2 (specimen with as-built reinforcement detailing and with utility opening) of the experimental specimens. On the other hand, the maximum yield load corresponds to 65% of the maximum strength for specimen S5 (less congested reinforcement detailing and with utility openings) of the experimental specimens.

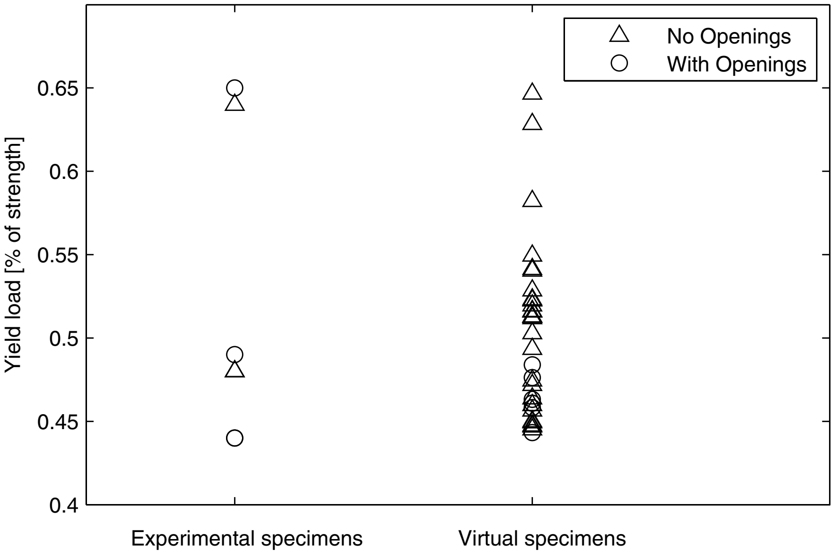

Fig. 5.8 Yield strength of experimental and virtual specimens.

Finally, it is important to note that Caltrans recommends vertical factored loads for the design of the ISH, which depends on the diaphragm height (Caltrans 2007). The suggested factored vertical load per bearing, for the reference ISH (which represents a 1/3-scale of a prototype ISH with 70 in. (1780 mm) diaphragm height), is 68 kip (302 kN). Accordingly, the mean safety factor is 3.2 (beyond any load factor incorporated in the suggested values from Caltrans (2007)) for the five tested specimens, obtained by dividing the mean experimental capacity by the suggested factored load. Similarly, the mean safety factor is 2.3 (beyond any load factor incorporated in the suggested values from Caltrans [2007]) for the virtual specimens considered in this study.

5.2 REINFORCEMENT DETAILING

This section contains design recommendations for the reinforcement detailing of the ISH. It is important to note that the experimental specimens were detailed with headed reinforcement for all bars of the ISH region except for the longitudinal bars (ρ_{slon} and ρ_{dlon}), the vertical bars of the seat (ρ_{sv}), and the diagonal bars of the diaphragm (ρ_{dd}); see Figure 5.1 for reinforcing bar designations. If headed bars are not used in the ISH, adequate lap splice length and hooked anchorages must be provided to the reinforcement.

5.2.1 Reinforcement Concentration Near Bearings

It is recommended to concentrate the reinforcement (using smaller spacing) within the extended bearing region, defined by an equivalent width of 1.5 times the seat height. Beyond this region, it is recommended to reduce the reinforcing steel ratio by 33%. It is important to note that the capacity estimates in the previous section are obtained for experimental and virtual specimens with this concentrated reinforcement near the bearings.

5.2.2 Diagonal Bars of Seat

The diagonal bars of the seat (ρ_{sd}) are the most critical bars (i.e., bars subjected to the largest strains) of the ISH region. These diagonal bars contribute to the sliding shear, SAT, 1D shear, and punching shear strength mechanisms of the ISH. Increasing their reinforcement ratio is the most effective way to increase the yield and peak the loads of the ISH. An orientation angle $35° \leq \theta \leq 55°$ is recommended, but 45° is preferred (see Fig. 5.1). A minimum reinforcement ratio of 0.2% is recommended (calculated using the vertical cross section of the seat).

5.2.3 Vertical Bars of Seat

The vertical bars of the seat (ρ_{sv}) contribute to the punching shear strength of the ISH. Distributing these vertical bars in several layers through the seat width improves the behavior of the seat by providing a more effective detailing for the punching shear mode of failure. Therefore, at least two layers are recommended to distribute these bars into, as shown in Figure 5.1. A minimum reinforcement ratio of ρ_{sv}=0.3% is recommended (calculated using the horizontal cross section of the seat) in the punching shear failure region shown in Figure 5.5. The vertical bars should have a hook of 135° at one end and of 90° at the other end, as shown in Figure 5.9, and they should be installed with alternating ends. It is to be noted that installing these bars does not considerably affect the construction process because the vertical bars can be easily installed from the top.

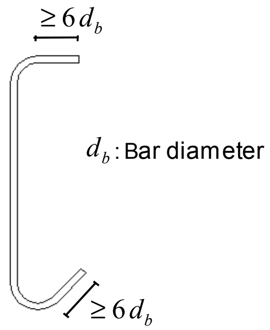

Fig. 5.9 Details of vertical bars of seat.

5.2.4 Horizontal Bars of the Seat

The horizontal bars of the seat (ρ_{sh}) contribute to the sliding shear, the bending, and the SAT strength mechanisms of the ISH. However, current designs of ISHs are over-reinforced with horizontal bars of the seat to prevent bending failure (Hube and Mosalam 2009). To increase the ductility of the seat, it is recommended to distribute these bars along the seat height using two or three layers. If three layers are used, it is recommended to install the middle layer close to the top one, as shown in Figure 5.1.

5.2.5 Longitudinal Bars of Seat

The longitudinal bars of the seat (ρ_{slon}) contribute to the bending strength of the seat along the longitudinal axis of the bridge. They are required to control the vertical (in the test orientation) bending cracks that appeared behind the seat in the five experimental specimens. It is recommended to use at least 4 bars distributed at the top and at the bottom of the seat, as shown in Figure 5.1. A minimum reinforcement ratio of 0.4% is recommended (calculated using the vertical cross section of the seat) to provide adequate yield strength and crack control for the ISH.

5.2.6 Diagonal Bars of Diaphragm

The diagonal bars of the diaphragm (ρ_{dd}) that are installed across the concrete junction of the diaphragm are not recommended for constructability concerns.

5.2.7 Vertical Bars of Diaphragm

The vertical bars of the diaphragm (ρ_{dv}) contribute to the SAT, 1D shear, and punching shear strength mechanisms of the ISH. It is recommended to distribute these bars using two layers, as shown in Figure 5.1. This recommendation allows using closed stirrups when headed bars are not installed or available.

5.2.8 Horizontal Bars of Diaphragm

The horizontal bars of the diaphragm (ρ_{dh}) transfer the horizontal stresses from the seat to the end diaphragm with prestressed blockout. It is recommended to distribute these bars using four layers, as shown in Figure 5.1. These bars should be long enough to provide adequate lap splices with the horizontal bars of the seat. The third layer, marked with (*) in Figure 5.1 is used to transfer the horizontal force component of the diagonal bars (tie KF of the SAT model in Fig. 5.3) of the seat and it should be sized accordingly. For constructability concerns of the upper and lower seats, it is not recommended to extend the horizontal bars of the diaphragm to the end of the seat. Figure 5.1 shows that the horizontal bars of the diaphragm do not continue towards the seat region (lower seat shown).

5.2.9 Longitudinal Bars of Diaphragm

The longitudinal bars of the diaphragm are not critical for the strength of the ISH when it is loaded vertically through the bearings. Minimum reinforcement should be installed to provide an adequate bending resistance and crack control along the diaphragm length.

5.3 GEOMETRICAL DETAILING

This section contains design recommendations for the geometrical considerations of the ISH. Additionally, design recommendations for the utility openings and the reinforcement are suggested.

5.3.1 Size of Bearing Plate

The size of the bearing plate has to be large enough to prevent local bearing failure of the concrete. Larger bearing plates can be used to considerably increase the strength and the ductility of the ISH. The use of larger bearing plates distributes the bearing load to a wider region of the seat, and accordingly increases the punching shear strength.

5.3.2 Seat Aspect Ratio

The seat aspect ratio is defined as $\alpha = b/h$, where b is the seat width and h is the seat height. The recommended range of this aspect ratio is $0.9 \leq \alpha \leq 1.5$. Aspect ratios $\alpha \leq 0.9$ (i.e., short seats) are not recommended because the risk of unseating is increased, the allowed tolerance for the construction of the bridge deck is reduced, and because the ISH becomes difficult to construct due to the small available space. For $\alpha \geq 1.5$ (i.e., long seats) the bending behavior of the seat becomes more important and additional horizontal reinforcement of the seat might be required. Additionally, for $\alpha \geq 1.5$, special vertical shear reinforcement needs to be installed in the seat between the bearing and the diaphragm.

5.3.3 Load Eccentricity

The ISH can be subjected to load eccentricity when the applied vertical load of the bearing is not centered with respect to the bearing plate. Such eccentricity may produce local bearing failure underneath the bearing plate. The accepted eccentricity is $\eta = e/b \leq 5\%$, where b is the seat width and e is the distance from the center of the seat to the applied load. This eccentricity is equivalent to approximately ±2 in. (51 mm) for the full-scale bridge. A second type of eccentricity occurs when the bearing pad is not located at the center of the seat, but the load is centered with respect to the bearing. This eccentricity can be treated as an ISH with different seat aspect ratio according to the previous section. For this case, b is obtained as two times the distance between the loading point and the diaphragm.

5.3.4 Utility Openings

The utility openings are introduced in the ISH region to allow routine inspection of the bearings. The utility openings are located at the center between two adjacent bearings to minimize its effect on the ISH. These openings can be located at the middle or lower height of the diaphragm (see Fig. 4.21 and Fig. 4.22, respectively). The shape of the opening may be square or circular and the recommended dimensions are $h_{op} = w_{op} = d_h/3$. A larger rectangular opening may be used with $h_{op} = d_h/3$ and $w_{op} \leq 1.5 h_{op}$, but additional reinforcement at or near the openings is required.

To minimize the effect of the openings on the strength of the ISH, additional diagonal reinforcement of the seat, and vertical reinforcement of the diaphragm are required adjacent to the utility openings. This is achieved by relocating the interrupted bars (because of the presence of the openings) to the opening side, such that the total number of bars is equivalent to the number of bars of an ISH without openings. To minimize cracking at the opening location, longitudinal bars around the openings should be provided (see Fig. 4.29). A minimum reinforcing steel ratio of 0.1% is recommended for these bars (area of steel divided by the diaphragm only concrete area in section B-B of Fig. 4.29).

5.4 ISH DESIGN METHODOLOGY

Based on the recommendations of this chapter, a design methodology for ISHs of RC box-girder bridges, subjected to vertical loads through the bearings, is presented in this section. This methodology is based on the strength estimation and the reinforcement and geometrical recommendations described previously. The design methodology is presented below.

1. Obtain the factored vertical design load of the ISH from the structural analysis of the whole bridge structure following the corresponding code recommendations. Alternatively, the recommended Caltrans factored load of Table 2.6 in Hube and Mosalam (2009) can be considered.
2. Determine the seat width of the ISH based on the code requirements of Section 2.1 in Hube and Mosalam (2009) and the recommendations of Section 5.3.2.
3. If a utility opening is required, determine its location and dimensions from Section 5.3.4. Smaller openings required for the installation of restrainers and equalizing bolts are not considered critical and no recommendations are provided.
4. Define the size of the bearing plates according to the manufacturer specifications and using the recommendations in Section 5.3.1.
5. Define reinforcement detailing of the ISH region based on the recommendations of Section 9.2.
6. Compute the nominal ISH strength based on sliding shear at the critical sections of the seat and diaphragm, Equations (2.5), (2.6), and (2.7) in Hube and Mosalam (2009).
7. Compute the nominal ISH strength based on bending moment at the seat and diaphragm, Equation (2.8) in Hube and Mosalam (2009).
8. Compute the nominal ISH strength based on the proposed 2D SAT, Equation (5.1).
9. Compute the nominal ISH strength based on 1D shear (see Fig. 5.4), Equations (2.13), (2.14), and (2.15) in Hube and Mosalam (2009).
10. Compute the nominal ISH strength based on punching shear (see Fig. 5.5), Equations (2.13), (2.16), and (2.17) in Hube and Mosalam (2009).
11. Verify that the minimum strength (with the corresponding reduction factor ϕ, defined by the adopted code requirements) predicted from steps 6–10 above, is larger than the factored vertical load from step 1.

12. Check the concrete bearing failure, e.g., using ACI318 (2008) requirements in Section 10.14, at the locations of the bearing plates to avoid localized concrete failure.
13. Specify reinforcement near the utility openings following the recommendations of Section 5.3.4.

6 Conclusions and Future Extensions

This report presents the results of the post-test analysis and the design recommendations for in-span-hinges (ISHs) of reinforced concrete (RC) box-girder bridges. The report focuses on ISHs of prestressed box-girder bridges, when subjected to vertical loads through the bearings. For the post-test analysis, a computational model is validated with the previous experimental results of five ISH specimens. With this computational model, a parametric study is conducted to predict the behavior and the strength of ISHs with different detailing and geometrical characteristics. This parametric study is intended to expand findings from the experimental program, by using these analysis virtual experiments.

The computational model adopts nonlinear three-dimensional (3D) finite element analysis (FEA) that considers cracking behavior of concrete and elastic-plastic behavior of the reinforcement. The reinforcing steel is modeled using embedded reinforcement formulation assuming perfect bond between the concrete and the reinforcement. The concrete material is modeled using the total strain rotating crack constitutive model. The reduction of compressive strength due to perpendicular cracking is incorporated in the constitutive model.

The parametric study of the ISHs is conducted using the proposed FEA. The variables analyzed in the parametric study are the reinforcement steel ratio and detailing characteristics, the size of the bearing plate, the aspect ratio of the seat, the load eccentricity and the characteristics of the utility openings.

From the results of the parametric study and the experimental program, detailed design recommendations and guidelines are presented for ISHs of RC box-girder bridges. These recommendations aimed towards obtaining optimal designs with less congestion and improved structural behavior. For the design recommendations of the ISH region, global geometrical parameters, reinforcement ratios, and detailing characteristics are considered. Additionally, design recommendations for the geometrical characteristics and the reinforcement detailing related to the utility openings of ISHs are presented in this report.

6.1 CONCLUSIONS

From the comparison of the experimental and computational results of ISHs, it is concluded that the developed 3D FEA is adequate to simulate the behavior, the strength, and the mode of failure of ISHs. The FEA is sensitive to the reinforcement details, the bearing plate size, the bearing plate location, the loading condition, and the presence of utility openings. Accordingly, the developed 3D FEA can be utilized to assess the behavior and the strength of current and future ISHs of RC box-girder bridges.

Based on the experimental and analytical results, it is concluded that the ISH fails with a combination of three failure modes when it is subjected to vertical loads though the bearings: (1) one-dimensional (1D) shear, (2) two-dimensional (2D) strut-and-tie (SAT), and (3) punching shear. Therefore, the ISH design must consider these failure modes and their combination, in addition to the bending and the sliding shear modes typically considered in the design approach of short cantilevers.

It is concluded that the strength of the ISH should be obtained from the critical of five design criteria: (1) sliding shear friction, (2) bending moment, (3) 2D SAT, (4) 1D shear, and (5) punching shear. The design equations corresponding to each design criteria are based on current ACI and Caltrans design code recommendations. Additionally, it is recommended to check the concrete bearing failure at the locations of the bearing plates to avoid localized concrete failure. Using this proposed design methodology a conservative strength estimate of the ISH can be achieved. The mean ratios of the "measured" capacity (using tests or FEA) versus the computed (using formulas for the above five design criteria) capacity are 1.40 and 1.05 for the experimental and virtual specimens, respectively. The difference between these two ratios is mainly due to the higher compressive concrete strength of the experimental specimens compared to the nominal compressive strength of the virtual specimens. Moreover, if the recommended design factored vertical loads from Caltrans are considered, it is concluded that mean safety factors (beyond any load factors incorporated in the suggested values from Caltrans) of 3.2 and 2.3 are obtained for the experimental and virtual specimens, respectively.

For service load levels, it is concluded that yielding is initiated in the diagonal reinforcement of the seat at about 50% of the maximum ISH strength. The lowest yield initiation is obtained at 44% of the maximum ISH strength for an experimental specimen containing utility openings and with as-built reinforcement configuration.

From the reinforcement detailing recommendations, it is concluded that the diagonal bars of the seat are the most critical bars of the ISH region. Increasing their reinforcement ratio is the most effective way to increase the yield and the peak loads of the ISHs. For economical and structural performance aspects, it is recommended to concentrate the reinforcement using smaller spacing within the extended bearing region, defined by an equivalent width of 1.5 times the seat height.

From the geometry recommendations, it is concluded that using larger bearing plates is an effective alternative to increase the strength and the ductility of the ISH. The use of larger bearing plates distributes the bearing load in a wider area of the ISH and increases the punching shear strength. Regarding the seat aspect ratio ($\alpha = b / h$ where b is the seat width and h is the seat height), it is concluded that a range of $0.9 \leq \alpha \leq 1.5$ is recommended mainly for constructability concerns.

When utility openings are required in the ISH region, it is concluded that the strength is not compromised if an adequate reinforcement detailing is provided near the openings.

Finally, it is concluded that use of headed bars is clearly appropriate to reduce reinforcement congestion for improving constructability and for providing adequate reinforcement development in the relatively small ISH region.

6.2 FUTURE EXTENSIONS

To identify the representative ISH characteristics, a survey of eight bridge projects was considered in this report. It is recommended to expand this survey to obtain a more representative characterization of current ISHs.

The experimental program conducted on ISHs considered only five specimens. To corroborate the design recommendations, it is suggested to expand the experimental program of ISHs with specimens of different geometrical and reinforcement detailing configurations. It would be desirable to corroborate the design recommendations for the following: (1) the concentration of the reinforcement near the bearing region, (2) the distribution of the vertical bars of the seat along the seat width, (3) the orientation of the diagonal bars of the seat, (4) the seat aspect ratio, (5) the utility opening locations, (6) the utility opening size, and (7) the utility opening reinforcement.

The proposed methodology to estimate the strength of ISHs is verified using the experimental results of five ISH specimens and the FE results of 38 virtual specimens. However, the virtual specimens of the parametric study are based on a reference ISH defined from the average properties of a survey of few bridge projects. The strength estimate using the proposed methodology should be compared with the FEA predictions for the ISHs of each surveyed project in a future study.

The development of a 3D nonlinear SAT model, a structural reliability analysis, and the use of topology optimization for the design of ISHs are considered parts of the study program of ISHs. These tasks are not addressed in this report and are suggested for the future study of ISHs. The development of a 3D nonlinear SAT model is aimed to simulate the behavior and the strength of ISHs to provide an alternative analysis tool to the proposed 3D FEA of this report. The structural reliability analysis of ISHs is suggested to obtain the probability of failure of current and future ISHs by developing a performance-based design and assessment framework for these critical regions of the bridge system. This reliability analysis can be used to improve the design recommendations of ISHs. Finally, the topology optimization is suggested to obtain alternative reinforcement configurations that could be used for the design of ISHs based on different optimization criteria (e.g., to minimize the total amount of steel for reduced cost, to minimize the use of diagonal reinforcement for improved constructability, etc.).

REFERENCES

ACI Committee 318, 2008. Building Code Requirements for Structural Concrete and Commentary, ACI 318-08. American Concrete Institute, Farmington Hills, MI.

Bažant, Z.P., Oh, B., 1983. Crack Band Theory for Fracture Concrete. *Material and Structures*, Vol. 16, No. 93, pp. 155-157.

Bažant, Z.P., Planas, J., 1998. Fracture and Size Effect in Concrete and Quasibrittle Materials. CRC Press, Boca Raton, Florida.

Belarbi, A., Hsu, T., 1991. Constitutive Laws of Reinforced Concrete in Biaxial Tension-Compression. Research Report UHCEE 91-2, University of Houston, Houston.

Caltrans, 2004. Bridge Design Specifications, California Department of Transportation, Sacramento.

Caltrans, 2006. Standard Plans. http://www.dot.ca.gov/hq/esc/oe/project_plans/Stdplnsindex.htm, California Department of Transportation, Sacramento.

Caltrans, 2007. Bridge Standard Detail Sheets (XS Sheets). http://www.dot.ca.gov/hq-/esc/techpubs/manual-/bridgemanuals/bridge-standard-detail-sheets/index.html. California Department of Transportation, Sacramento.

Cho, K., Kobayashi, A., Hawkins, N., Barker, D., Jeang, F., 1984. Fracture Process Zone of Concrete Cracks. *Journal of Engineering Mechanics*, ASCE, Vol. 110, No. 8, pp. 1174-1184.

Comité Euro-International du Béton, 1990. CEB-FIP Model Code. Thomas Telford House.

Cornelissen, H., Hordijk, D., and Reinhardt, H., 1986. Experimental Determination of Crack Softening Characteristics of Normalweight and Lightweight Concrete. *Heron*, Vol. 31, No. 2.

DIANA, 2008. Diana Finite Element Analysis User's Manual Release 9.3, TNO DIANA vb, The Netherlands.

EERI, 2005. Northridge Earthquake Reconnaissance Report, Volume 1, *Earthquake Spectra*, 11: pp. 287-372, supplemental report to Volume 11.

Evans, R., Marathe, M., 1968. Microcracking and Stress-Strain Curves for Concrete in Tension. *Materiaux et Constructions*, Vol. 1, No. 1, pp. 61-64.

Gerstle, K.H., 1981. Simple Formulation of Triaxial Concrete Behavior. *ACI Structural Journal*, Vol. 78. No. 5, pp. 382-387.

Gopalaratnam, V.S., Shah S.P., 1985. Softening Response of Plain Concrete in Direct Tension. *ACI Structural Journal*, Vol. 82, No. 3, pp. 310-323.

Hillerborg, A., Modeer, M., Peterson, P., 1976. Analysis of Crack Formation and Crack Growth in Concrete by Means of Fracture Mechanics and Finite Elements. *Cement Concrete Research*, Vol. 6, No. 6, pp. 773-782.

Hillerborg, A., 1985. Numerical Methods to Simulate Softening and Fracture of Concrete. *Fracture Mechanics of Concrete,* pp. 141-170.

Hsieh, S.S., Ting, E.C., Chen, W.F., 1982. A Plastic-Fracture Model for Concrete. *International Journal of Solids Structures*, Vol. 18, No. 3, pp. 181-197.

Hube, M.A., Mosalam, K.M., 2009. Experimental and Computational Evaluation of Current and Innovative In-Span Hinge Details in Reinforced Concrete Box-Girder Bridges, Part 1: Experimental Findings and Pre-Test Analysis. PEER Report 2008/103, University of California, Berkeley.

Hughes, T. J. 2000. The Finite Element Method, Linear Static and Dynamic Finite Element Analysis. Dover Publications, Mineola, New York.

Koeberl, B., William, K., 2008. Question of Tension Softening versus Tension Stiffening in Plain and Reinforced Concrete. *Journal of Engineering Mechanics*, ASCE, Vol. 134, No. 9, pp. 804-808.

Kupfer, H., Hilsdorf, H.K., Rusch, H., 1969. Behavior of Concrete under Biaxial Stresses. *American Concrete Institute Journal*, Vol. 66, No. 8, pp. 656-666.

Maekawa, K., Irawan P., Okamura, H., 1997. Path-Dependent Three-Dimensional Constitutive Laws of Reinforced Concrete-Formulation and Experimental Verifications. *Structural Engineering and Mechanics*, Vol. 5, No. 6, pp. 743-754.

Maekawa, K., Pimanmas, A., Okamura, H., 2003. Nonlinear Mechanics of Reinforced Concrete. Spon Press, London.

Mills, L.L., Zimmerman, R.M., 1970. Compressive Strength of Plain Concrete under Multiaxial. Loading. *ACI Structural Journal*, Vol. 67, No. 10, pp. 802-807.

Mosalam, K.M., Paulino, G.H., 1997. Evolutionary Characteristic Length Method for Smeared Cracking Finite Element Models. *Finite Elements in Analysis and Design*, Vol. 27, No. 1, pp. 99-108.

Ottosen, N.S, 1977. A Failure Criterion for Concrete. *Journal of Engineering Mechanics,* ASCE, Vol. 103, No. 4, pp. 527-535.

Peterson, P., 1981. Crack Growth and Development of Fracture Zone in Plain Concrete and Similar Materials. Report No. TVBM-1006, Division of Building Materials, Lund Institute of Technology, Sweden.

Reinhardt, H., 1984. Fracture Mechanics of an Elastic Softening Material Like Concrete. *Heron*, Vol. 29, No. 2.

Richart, F.E., Brandtzaeg, A., Brown, R.L., 1928. A Study of the Failure of Concrete under Combined Compressive Stresses. University of Illinois, Engineering Experiment Station Bulletin, Vol. 26, No. 12.

Rilem TC 50-FMC, 1985. Determination of the Fracture Energy of Mortar and Concrete by Means of Three-point Bend Tests on Notched Beams. Committee on the Fracture Mechanics of Concrete, Materials and Structures, Vol. 18, No. 106, pp. 285–290.

Rots, J., Nauta, P., Kusters, G., Blaauwendraad, J., 1985. Smeared Crack Approach and Fracture Localization in Concrete. *Heron*, Vol. 30, No. 1.

Selby, R.G. and Vecchio, F.J., 1993. Three Dimensional Constitutive Relations for Reinforced Concrete. Tech. Report 93-02, Department of Civil Engineering, Univ. of Toronto, Canada.

Simo, J.C., Rifai, M.S., 1990. A Class of Mixed Assumed Strain Methods and the Method of Incompatible Modes. *Int. J. for Numerical Methods in Engineering,* Vol. 29, No. 8, pp. 1595-1638.

Shirai, S., Noguchi, H., 1989. Compressive Deterioration of Cracked Concrete. *Proc. ASCE Structures Congress: Structural Design, Analysis and Testing*, New York, pp. 1-10.

Vecchio, F.J., Collins, M.P., 1986. The Modified Compression-Field Theory for Reinforced Concrete Elements Subjected to Shear. *ACI Structural Journal*, Vol. 83, No. 22, pp. 219-231.

Vecchio, F.J., Collins, M.P., 1993. Compression Response of Cracked Reinforced Concrete. *Journal of Structural Engineering*, Vol. 19, No. 12, pp. 3590-3610.

Voce, E., 1948. The relationship Between Stress and Strain for Homogenous Deformation. *Journal of the Institute of Metals*, Vol. 74, No. 11, pp. 537-562.

Yankelevsky, D., Jabareen, Abutbul, M., 2008. One Dimensional Analysis of Tension Stiffening in Reinforced Concrete with Discrete Cracks. *Engineering Structures*, Vol. 30, No. 1 ,pp. 206-217.

Zhao, Z., Kwon, F., Shah, S., 2008. Effect of Specimen Size on Fracture Energy and Softening Curve of Concrete: Part 1, Experiments and Fracture Energy. *Cement and Concrete Research*. Vol. 38, No. 8, pp. 1049-1060.

Zienkiewicz, O.C., Taylor, R.L. 2005. The Finite Element Method, Sixth Edition. Elsevier Butterworth-Heinemann, Burlington, MA.

Appendix A: Capacity Estimation Results for Virtual Specimens

This appendix shows the detailed capacity estimates for the different failure modes for the virtual specimens used in the parametric study. These capacity estimates are compared with the strength of the virtual specimens predicted by the FEA. In this appendix, the capacities are normalized by the strength C_r of the reference ISH (see Section 4.1). Also, for the figures of this appendix, SS_s corresponds to sliding shear of the seat, SS_d to sliding shear of the diaphragm, B_s to bending moment of the seat, B_d to bending moment of the diaphragm, SAT to 2D strut-and-tie, S to 1D shear, and PS to punching shear. It is to be noted that some design criteria that are not shown in the subsequent figures have values larger than the range of the figure.

A.1 REINFORCEMENT VARIATIONS

The capacity estimates of the virtual specimens with varying reinforcing steel ratios and detailing are presented in this section.

The capacity estimates for the virtual specimens with varying reinforcement ratios and different orientations of the diagonal bars of the seat are shown in Figure A.1. For the three orientation angles it can be observed that the SAT and the punching shear (PS) accurately predict the FEA strength when $\rho_{sd} \leq 0.3\%$.

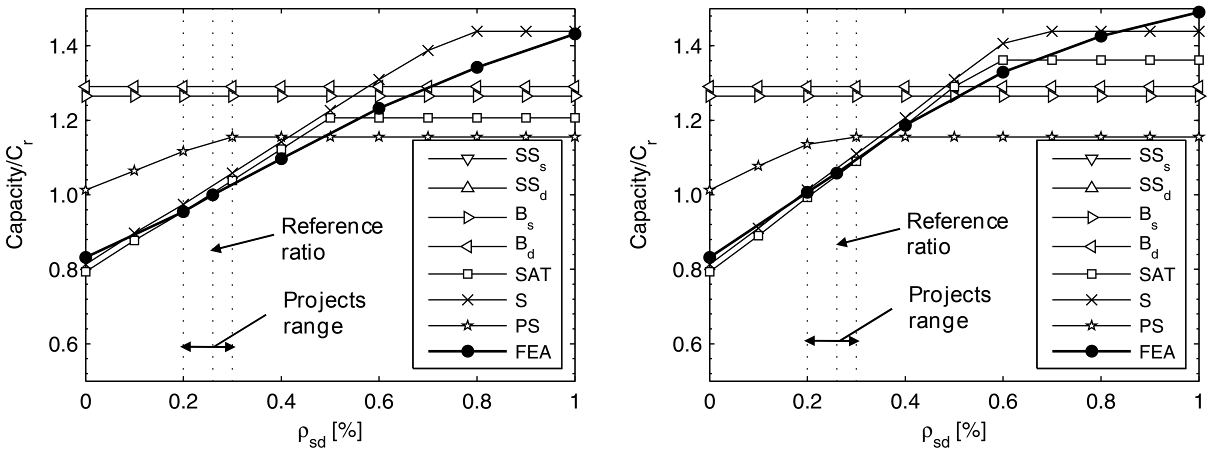

(a) 36° orientation

(b) 45°orientation

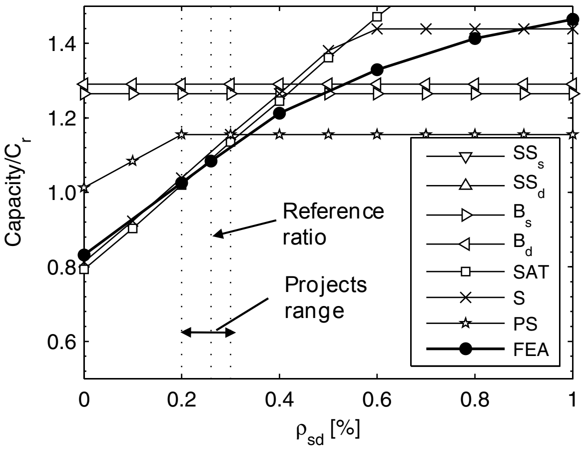

(c) 54°orientation

Fig. A.1 Capacity estimates with varying diagonal reinforcement of seat (ρ_{sd}).

The capacity estimates for the virtual specimens with varying reinforcement ratios and different configurations of the vertical bars of the seat are shown in Figure A.2. For the three reinforcement configurations (see section 4.2), it is observed that the punching shear (PS) failure mode underestimates the FEA strength for small reinforcement ratios. For $\rho_{sv} \geq 0.5\%$, the punching shear capacity is constant because it is controlled by the punching shear limit of $V_n = 6\sqrt{f_c^{'}}b_o d$. Additionally, when the vertical steel is distributed using two or three layers and $\rho_{sv} \geq 0.5\%$, the FEA strength is larger than the capacity prediction of the SAT and the 1D shear (S) modes of failure.

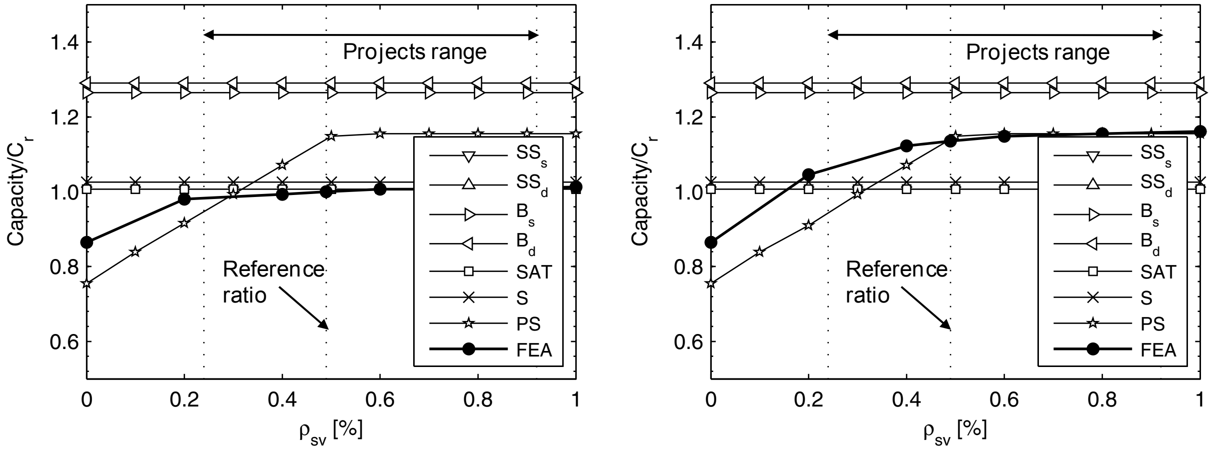

(a) Steel concentrated in one layer (b) Steel distributed in two layers

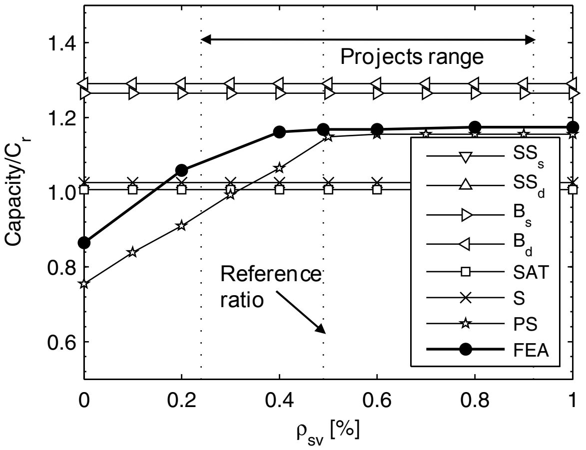

(c) Steel distributed in four layers

Fig. A.2 Capacity estimates with varying vertical reinforcement of seat (ρ_{sv}).

The capacity estimates for the virtual specimens with varying reinforcement ratios and different configurations of the horizontal bars of the seat are shown in Figure A.3. For the two reinforcement configurations (refer to Section 4.2), it is observed that the SAT and the bending moment of the seat (B_s) underestimate the FEA strength for small reinforcement ratios. Additionally, it is observed that the predicted sliding shear capacity of the seat (SS_s) is never smaller than the FEA strength.

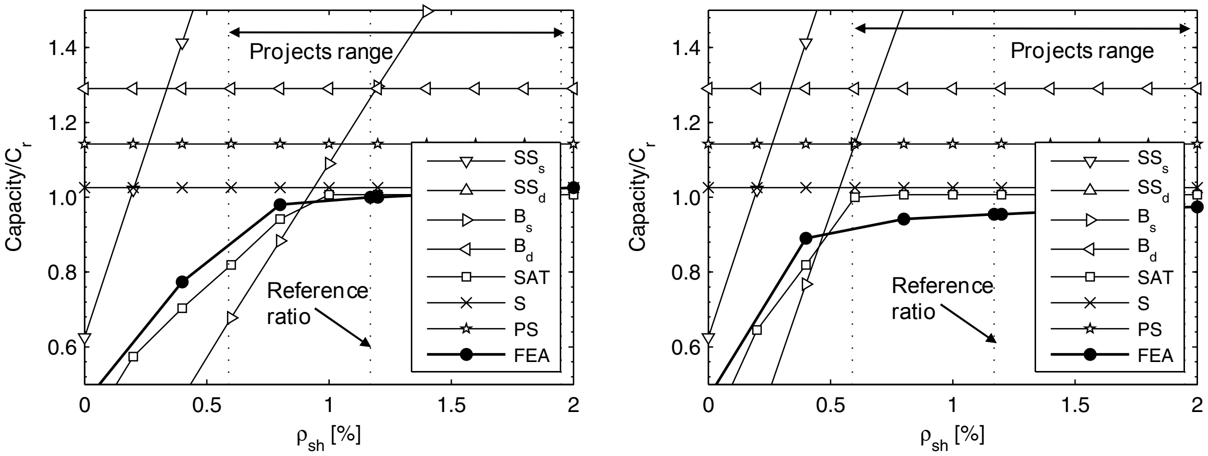

(a) Steel distributed in three layers (b) Steel concentrated in one layer

Fig. A.3 Capacity estimates with varying horizontal reinforcement of seat (ρ_{sh}).

The capacity estimates for the virtual specimens with varying reinforcement ratios of the longitudinal bars of the seat are shown in Figure A.4. It is observed that the predicted capacity of all the failure modes is not affected by this reinforcement ratio.

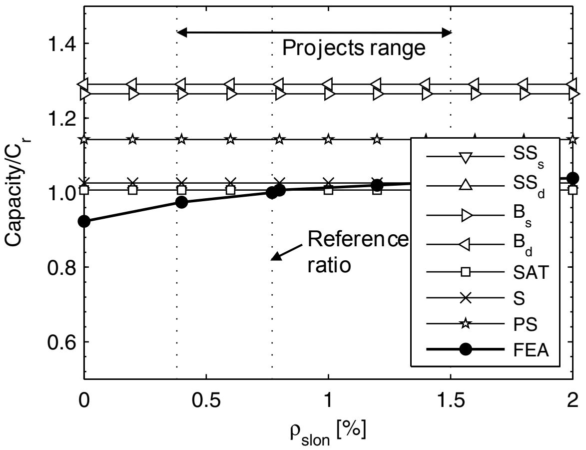

Fig. A.4 Capacity estimates with varying longitudinal reinforcement of seat (ρ_{slon}).

The capacity estimates for the virtual specimens with varying reinforcement ratios and different configurations of the vertical bars of the diaphragm are shown in Figure A.5. For the two reinforcement configurations (see Section 4.2), it is observed that the SAT and the shear modes of failure (S) underestimate the FEA strength for small reinforcement ratios.

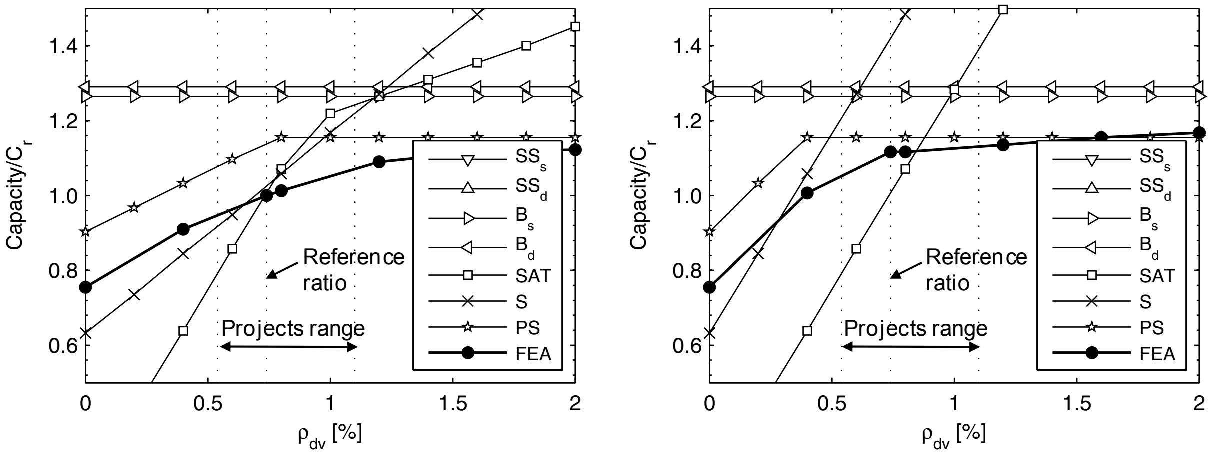

(a) Steel distributed in two layers (b) Steel concentrated in one layer

Fig. A.5 Capacity estimates with varying vertical reinforcement of diaphragm (ρ_{dv}).

The capacity estimates for the virtual specimens with varying reinforcement ratios of the horizontal bars of the diaphragm are shown in Figure A.6. It is observed that the sliding shear of the diaphragm and the bending of the diaphragm underestimate the FEA strength for small reinforcement ratios.

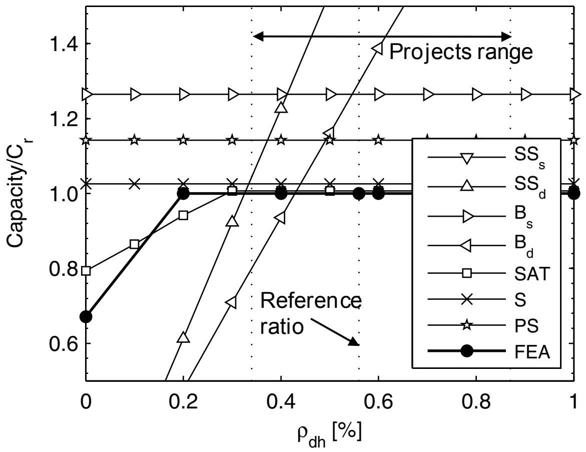

Fig. A.6 Capacity estimates with varying horizontal reinforcement of diaphragm (ρ_{dh}).

A.2 GEOMETRY VARIATIONS

The capacity estimates of the virtual specimens with varying bearing plate size and varying aspect ratios of the seat are presented in this section.

The capacity estimates for the virtual specimens with varying bearing plate size are shown in Figure A.7 (see Section 4.3). In Figure A.7 bp is the bearing size in the transverse direction of the bridge and bw is the distance between the box webs of the bridge (see Section 4.3). For the case of the geometrical variations, the capacity prediction for the different failure modes is only computed for the case of the virtual specimens (i.e., the capacity is computed only at three points as shown in Fig. A.7). From Figure A.7, it is observed that the punching shear failure mode is the only one affected by the bearing plate size. It is also observed that the 1D shear (S) and SAT modes of failure underestimate the FEA strength when the bearing plate size (bp/bw) is larger than the reference size. Finally, Figure A.7 shows that the punching shear strength overestimates the FEA strength for the three cases.

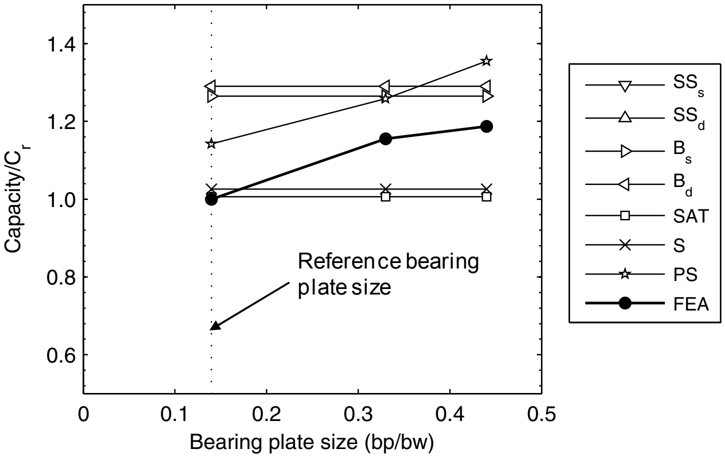

Fig. A.7 Capacity estimates with varying bearing plate size.

The capacity estimates for the virtual specimens with varying size of the seat aspect ratio is shown in Figure A.8 (see Section 4.4). It is observed that the capacity predictions for the bending of the seat (B_s) and of the diaphragm (B_s) decrease as the aspect ratio of the seat increases. For the case of α=1.71, it is observed that the bending of the seat becomes the critical failure mode (i.e., the failure mode that predicts the lowest capacity).

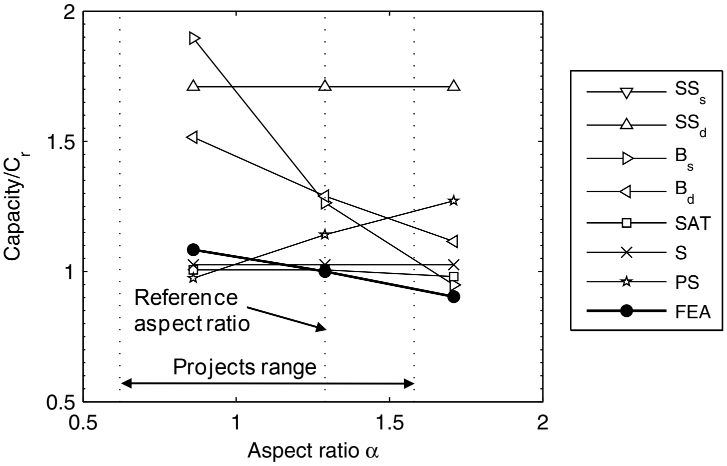

Fig. A.8 Capacity estimates with varying aspect ratio of seat.

PEER REPORTS

PEER reports are available individually or by yearly subscription. PEER reports can be ordered at http://peer.berkeley.edu/publications/peer_reports.html or by contacting the Pacific Earthquake Engineering Research Center, 1301 South 46th Street, Richmond, CA 94804-4698. Tel.: (510) 665-3448; Fax: (510) 665-3456; Email: peer_editor@berkeley.edu

PEER 2009/03 *The Integration of Experimental and Simulation Data in the Study of Reinforced Concrete Bridge Systems Including Soil-Foundation-Structure Interaction.* Matthew Dryden and Gregory L. Fenves. November 2009.

PEER 2009/02 *Improving Earthquake Mitigation through Innovations and Applications in Seismic Science, Engineering, Communication, and Response. Proceedings of a U.S.-Iran Seismic Workshop.* October 2009.

PEER 2009/01 *Evaluation of Ground Motion Selection and Modification Methods: Predicting Median Interstory Drift Response of Buildings.* Curt B. Haselton, Ed. June 2009.

PEER 2008/10 *Technical Manual for Strata.* Albert R. Kottke and Ellen M. Rathje. February 2009.

PEER 2008/09 *NGA Model for Average Horizontal Component of Peak Ground Motion and Response Spectra.* Brian S.-J. Chiou and Robert R. Youngs. November 2008.

PEER 2008/08 *Toward Earthquake-Resistant Design of Concentrically Braced Steel Structures.* Patxi Uriz and Stephen A. Mahin. November 2008.

PEER 2008/07 *Using OpenSees for Performance-Based Evaluation of Bridges on Liquefiable Soils.* Stephen L. Kramer, Pedro Arduino, and HyungSuk Shin. November 2008.

PEER 2008/06 *Shaking Table Tests and Numerical Investigation of Self-Centering Reinforced Concrete Bridge Columns.* Hyung IL Jeong, Junichi Sakai, and Stephen A. Mahin. September 2008.

PEER 2008/05 *Performance-Based Earthquake Engineering Design Evaluation Procedure for Bridge Foundations Undergoing Liquefaction-Induced Lateral Ground Displacement.* Christian A. Ledezma and Jonathan D. Bray. August 2008.

PEER 2008/04 *Benchmarking of Nonlinear Geotechnical Ground Response Analysis Procedures.* Jonathan P. Stewart, Annie On-Lei Kwok, Yousseff M. A. Hashash, Neven Matasovic, Robert Pyke, Zhiliang Wang, and Zhaohui Yang. August 2008.

PEER 2008/03 *Guidelines for Nonlinear Analysis of Bridge Structures in California.* Ady Aviram, Kevin R. Mackie, and Božidar Stojadinović. August 2008.

PEER 2008/02 *Treatment of Uncertainties in Seismic-Risk Analysis of Transportation Systems.* Evangelos Stergiou and Anne S. Kiremidjian. July 2008.

PEER 2008/01 *Seismic Performance Objectives for Tall Buildings.* William T. Holmes, Charles Kircher, William Petak, and Nabih Youssef. August 2008.

PEER 2007/12 *An Assessment to Benchmark the Seismic Performance of a Code-Conforming Reinforced Concrete Moment-Frame Building.* Curt Haselton, Christine A. Goulet, Judith Mitrani-Reiser, James L. Beck, Gregory G. Deierlein, Keith A. Porter, Jonathan P. Stewart, and Ertugrul Taciroglu. August 2008.

PEER 2007/11 *Bar Buckling in Reinforced Concrete Bridge Columns.* Wayne A. Brown, Dawn E. Lehman, and John F. Stanton. February 2008.

PEER 2007/10 *Computational Modeling of Progressive Collapse in Reinforced Concrete Frame Structures.* Mohamed M. Talaat and Khalid M. Mosalam. May 2008.

PEER 2007/09 *Integrated Probabilistic Performance-Based Evaluation of Benchmark Reinforced Concrete Bridges.* Kevin R. Mackie, John-Michael Wong, and Božidar Stojadinović. January 2008.

PEER 2007/08 *Assessing Seismic Collapse Safety of Modern Reinforced Concrete Moment-Frame Buildings.* Curt B. Haselton and Gregory G. Deierlein. February 2008.

PEER 2007/07 *Performance Modeling Strategies for Modern Reinforced Concrete Bridge Columns.* Michael P. Berry and Marc O. Eberhard. April 2008.

PEER 2007/06 *Development of Improved Procedures for Seismic Design of Buried and Partially Buried Structures.* Linda Al Atik and Nicholas Sitar. June 2007.

PEER 2007/05 *Uncertainty and Correlation in Seismic Risk Assessment of Transportation Systems.* Renee G. Lee and Anne S. Kiremidjian. July 2007.

PEER 2007/04 *Numerical Models for Analysis and Performance-Based Design of Shallow Foundations Subjected to Seismic Loading.* Sivapalan Gajan, Tara C. Hutchinson, Bruce L. Kutter, Prishati Raychowdhury, José A. Ugalde, and Jonathan P. Stewart. May 2008.

PEER 2007/03 *Beam-Column Element Model Calibrated for Predicting Flexural Response Leading to Global Collapse of RC Frame Buildings.* Curt B. Haselton, Abbie B. Liel, Sarah Taylor Lange, and Gregory G. Deierlein. May 2008.

PEER 2007/02 *Campbell-Bozorgnia NGA Ground Motion Relations for the Geometric Mean Horizontal Component of Peak and Spectral Ground Motion Parameters.* Kenneth W. Campbell and Yousef Bozorgnia. May 2007.

PEER 2007/01 *Boore-Atkinson NGA Ground Motion Relations for the Geometric Mean Horizontal Component of Peak and Spectral Ground Motion Parameters.* David M. Boore and Gail M. Atkinson. May. May 2007.

PEER 2006/12 *Societal Implications of Performance-Based Earthquake Engineering.* Peter J. May. May 2007.

PEER 2006/11 *Probabilistic Seismic Demand Analysis Using Advanced Ground Motion Intensity Measures, Attenuation Relationships, and Near-Fault Effects.* Polsak Tothong and C. Allin Cornell. March 2007.

PEER 2006/10 *Application of the PEER PBEE Methodology to the I-880 Viaduct.* Sashi Kunnath. February 2007.

PEER 2006/09 *Quantifying Economic Losses from Travel Forgone Following a Large Metropolitan Earthquake.* James Moore, Sungbin Cho, Yue Yue Fan, and Stuart Werner. November 2006.

PEER 2006/08 *Vector-Valued Ground Motion Intensity Measures for Probabilistic Seismic Demand Analysis*. Jack W. Baker and C. Allin Cornell. October 2006.

PEER 2006/07 *Analytical Modeling of Reinforced Concrete Walls for Predicting Flexural and Coupled–Shear-Flexural Responses*. Kutay Orakcal, Leonardo M. Massone, and John W. Wallace. October 2006.

PEER 2006/06 *Nonlinear Analysis of a Soil-Drilled Pier System under Static and Dynamic Axial Loading.* Gang Wang and Nicholas Sitar. November 2006.

PEER 2006/05 *Advanced Seismic Assessment Guidelines.* Paolo Bazzurro, C. Allin Cornell, Charles Menun, Maziar Motahari, and Nicolas Luco. September 2006.

PEER 2006/04 *Probabilistic Seismic Evaluation of Reinforced Concrete Structural Components and Systems.* Tae Hyung Lee and Khalid M. Mosalam. August 2006.

PEER 2006/03 *Performance of Lifelines Subjected to Lateral Spreading.* Scott A. Ashford and Teerawut Juirnarongrit. July 2006.

PEER 2006/02 *Pacific Earthquake Engineering Research Center Highway Demonstration Project.* Anne Kiremidjian, James Moore, Yue Yue Fan, Nesrin Basoz, Ozgur Yazali, and Meredith Williams. April 2006.

PEER 2006/01 *Bracing Berkeley. A Guide to Seismic Safety on the UC Berkeley Campus.* Mary C. Comerio, Stephen Tobriner, and Ariane Fehrenkamp. January 2006.

PEER 2005/16 *Seismic Response and Reliability of Electrical Substation Equipment and Systems.* Junho Song, Armen Der Kiureghian, and Jerome L. Sackman. April 2006.

PEER 2005/15 *CPT-Based Probabilistic Assessment of Seismic Soil Liquefaction Initiation.* R. E. S. Moss, R. B. Seed, R. E. Kayen, J. P. Stewart, and A. Der Kiureghian. April 2006.

PEER 2005/14 *Workshop on Modeling of Nonlinear Cyclic Load-Deformation Behavior of Shallow Foundations.* Bruce L. Kutter, Geoffrey Martin, Tara Hutchinson, Chad Harden, Sivapalan Gajan, and Justin Phalen. March 2006.

PEER 2005/13 *Stochastic Characterization and Decision Bases under Time-Dependent Aftershock Risk in Performance-Based Earthquake Engineering.* Gee Liek Yeo and C. Allin Cornell. July 2005.

PEER 2005/12 *PEER Testbed Study on a Laboratory Building: Exercising Seismic Performance Assessment.* Mary C. Comerio, editor. November 2005.

PEER 2005/11 *Van Nuys Hotel Building Testbed Report: Exercising Seismic Performance Assessment.* Helmut Krawinkler, editor. October 2005.

PEER 2005/10 *First NEES/E-Defense Workshop on Collapse Simulation of Reinforced Concrete Building Structures.* September 2005.

PEER 2005/09 *Test Applications of Advanced Seismic Assessment Guidelines.* Joe Maffei, Karl Telleen, Danya Mohr, William Holmes, and Yuki Nakayama. August 2006.

PEER 2005/08 *Damage Accumulation in Lightly Confined Reinforced Concrete Bridge Columns.* R. Tyler Ranf, Jared M. Nelson, Zach Price, Marc O. Eberhard, and John F. Stanton. April 2006.

PEER 2005/07 *Experimental and Analytical Studies on the Seismic Response of Freestanding and Anchored Laboratory Equipment.* Dimitrios Konstantinidis and Nicos Makris. January 2005.

PEER 2005/06 *Global Collapse of Frame Structures under Seismic Excitations*. Luis F. Ibarra and Helmut Krawinkler. September 2005.

PEER 2005//05 *Performance Characterization of Bench- and Shelf-Mounted Equipment.* Samit Ray Chaudhuri and Tara C. Hutchinson. May 2006.

PEER 2005/04 *Numerical Modeling of the Nonlinear Cyclic Response of Shallow Foundations.* Chad Harden, Tara Hutchinson, Geoffrey R. Martin, and Bruce L. Kutter. August 2005.

PEER 2005/03 *A Taxonomy of Building Components for Performance-Based Earthquake Engineering.* Keith A. Porter. September 2005.

PEER 2005/02 *Fragility Basis for California Highway Overpass Bridge Seismic Decision Making*. Kevin R. Mackie and Božidar Stojadinović. June 2005.

PEER 2005/01 *Empirical Characterization of Site Conditions on Strong Ground Motion.* Jonathan P. Stewart, Yoojoong Choi, and Robert W. Graves. June 2005.

PEER 2004/09 *Electrical Substation Equipment Interaction: Experimental Rigid Conductor Studies.* Christopher Stearns and André Filiatrault. February 2005.

PEER 2004/08 *Seismic Qualification and Fragility Testing of Line Break 550-kV Disconnect Switches*. Shakhzod M. Takhirov, Gregory L. Fenves, and Eric Fujisaki. January 2005.

PEER 2004/07 *Ground Motions for Earthquake Simulator Qualification of Electrical Substation Equipment.* Shakhzod M. Takhirov, Gregory L. Fenves, Eric Fujisaki, and Don Clyde. January 2005.

PEER 2004/06 *Performance-Based Regulation and Regulatory Regimes.* Peter J. May and Chris Koski. September 2004.

PEER 2004/05 *Performance-Based Seismic Design Concepts and Implementation: Proceedings of an International Workshop.* Peter Fajfar and Helmut Krawinkler, editors. September 2004.

PEER 2004/04 *Seismic Performance of an Instrumented Tilt-up Wall Building.* James C. Anderson and Vitelmo V. Bertero. July 2004.

PEER 2004/03 *Evaluation and Application of Concrete Tilt-up Assessment Methodologies.* Timothy Graf and James O. Malley. October 2004.

PEER 2004/02 *Analytical Investigations of New Methods for Reducing Residual Displacements of Reinforced Concrete Bridge Columns.* Junichi Sakai and Stephen A. Mahin. August 2004.

PEER 2004/01 *Seismic Performance of Masonry Buildings and Design Implications.* Kerri Anne Taeko Tokoro, James C. Anderson, and Vitelmo V. Bertero. February 2004.

PEER 2003/18 *Performance Models for Flexural Damage in Reinforced Concrete Columns.* Michael Berry and Marc Eberhard. August 2003.

PEER 2003/17 *Predicting Earthquake Damage in Older Reinforced Concrete Beam-Column Joints.* Catherine Pagni and Laura Lowes. October 2004.

PEER 2003/16 *Seismic Demands for Performance-Based Design of Bridges.* Kevin Mackie and Božidar Stojadinović. August 2003.

PEER 2003/15 *Seismic Demands for Nondeteriorating Frame Structures and Their Dependence on Ground Motions.* Ricardo Antonio Medina and Helmut Krawinkler. May 2004.

PEER 2003/14 *Finite Element Reliability and Sensitivity Methods for Performance-Based Earthquake Engineering.* Terje Haukaas and Armen Der Kiureghian. April 2004.

PEER 2003/13 *Effects of Connection Hysteretic Degradation on the Seismic Behavior of Steel Moment-Resisting Frames.* Janise E. Rodgers and Stephen A. Mahin. March 2004.

PEER 2003/12 *Implementation Manual for the Seismic Protection of Laboratory Contents: Format and Case Studies.* William T. Holmes and Mary C. Comerio. October 2003.

PEER 2003/11 *Fifth U.S.-Japan Workshop on Performance-Based Earthquake Engineering Methodology for Reinforced Concrete Building Structures.* February 2004.

PEER 2003/10 *A Beam-Column Joint Model for Simulating the Earthquake Response of Reinforced Concrete Frames.* Laura N. Lowes, Nilanjan Mitra, and Arash Altoontash. February 2004.

PEER 2003/09 *Sequencing Repairs after an Earthquake: An Economic Approach.* Marco Casari and Simon J. Wilkie. April 2004.

PEER 2003/08 *A Technical Framework for Probability-Based Demand and Capacity Factor Design (DCFD) Seismic Formats*. Fatemeh Jalayer and C. Allin Cornell. November 2003.

PEER 2003/07 *Uncertainty Specification and Propagation for Loss Estimation Using FOSM Methods.* Jack W. Baker and C. Allin Cornell. September 2003.

PEER 2003/06 *Performance of Circular Reinforced Concrete Bridge Columns under Bidirectional Earthquake Loading*. Mahmoud M. Hachem, Stephen A. Mahin, and Jack P. Moehle. February 2003.

PEER 2003/05 *Response Assessment for Building-Specific Loss Estimation.* Eduardo Miranda and Shahram Taghavi. September 2003.

PEER 2003/04 *Experimental Assessment of Columns with Short Lap Splices Subjected to Cyclic Loads*. Murat Melek, John W. Wallace, and Joel Conte. April 2003.

PEER 2003/03 *Probabilistic Response Assessment for Building-Specific Loss Estimation.* Eduardo Miranda and Hesameddin Aslani. September 2003.

PEER 2003/02 *Software Framework for Collaborative Development of Nonlinear Dynamic Analysis Program.* Jun Peng and Kincho H. Law. September 2003.

PEER 2003/01 *Shake Table Tests and Analytical Studies on the Gravity Load Collapse of Reinforced Concrete Frames.* Kenneth John Elwood and Jack P. Moehle. November 2003.

PEER 2002/24 *Performance of Beam to Column Bridge Joints Subjected to a Large Velocity Pulse.* Natalie Gibson, André Filiatrault, and Scott A. Ashford. April 2002.

PEER 2002/23 *Effects of Large Velocity Pulses on Reinforced Concrete Bridge Columns.* Greg L. Orozco and Scott A. Ashford. April 2002.

PEER 2002/22 *Characterization of Large Velocity Pulses for Laboratory Testing.* Kenneth E. Cox and Scott A. Ashford. April 2002.

PEER 2002/21 *Fourth U.S.-Japan Workshop on Performance-Based Earthquake Engineering Methodology for Reinforced Concrete Building Structures*. December 2002.

PEER 2002/20 *Barriers to Adoption and Implementation of PBEE Innovations.* Peter J. May. August 2002.

PEER 2002/19 *Economic-Engineered Integrated Models for Earthquakes: Socioeconomic Impacts.* Peter Gordon, James E. Moore II, and Harry W. Richardson. July 2002.

PEER 2002/18 *Assessment of Reinforced Concrete Building Exterior Joints with Substandard Details.* Chris P. Pantelides, Jon Hansen, Justin Nadauld, and Lawrence D. Reaveley. May 2002.

PEER 2002/17 *Structural Characterization and Seismic Response Analysis of a Highway Overcrossing Equipped with Elastomeric Bearings and Fluid Dampers: A Case Study.* Nicos Makris and Jian Zhang. November 2002.

PEER 2002/16 *Estimation of Uncertainty in Geotechnical Properties for Performance-Based Earthquake Engineering.* Allen L. Jones, Steven L. Kramer, and Pedro Arduino. December 2002.

PEER 2002/15 *Seismic Behavior of Bridge Columns Subjected to Various Loading Patterns.* Asadollah Esmaeily-Gh. and Yan Xiao. December 2002.

PEER 2002/14 *Inelastic Seismic Response of Extended Pile Shaft Supported Bridge Structures.* T.C. Hutchinson, R.W. Boulanger, Y.H. Chai, and I.M. Idriss. December 2002.

PEER 2002/13 *Probabilistic Models and Fragility Estimates for Bridge Components and Systems.* Paolo Gardoni, Armen Der Kiureghian, and Khalid M. Mosalam. June 2002.

PEER 2002/12 *Effects of Fault Dip and Slip Rake on Near-Source Ground Motions: Why Chi-Chi Was a Relatively Mild M7.6 Earthquake.* Brad T. Aagaard, John F. Hall, and Thomas H. Heaton. December 2002.

PEER 2002/11 *Analytical and Experimental Study of Fiber-Reinforced Strip Isolators*. James M. Kelly and Shakhzod M. Takhirov. September 2002.

PEER 2002/10 *Centrifuge Modeling of Settlement and Lateral Spreading with Comparisons to Numerical Analyses***.** Sivapalan Gajan and Bruce L. Kutter. January 2003.

PEER 2002/09 *Documentation and Analysis of Field Case Histories of Seismic Compression during the 1994 Northridge, California, Earthquake.* Jonathan P. Stewart, Patrick M. Smith, Daniel H. Whang, and Jonathan D. Bray. October 2002.

PEER 2002/08 *Component Testing, Stability Analysis and Characterization of Buckling-Restrained Unbonded Braces™.* Cameron Black, Nicos Makris, and Ian Aiken. September 2002.

PEER 2002/07 *Seismic Performance of Pile-Wharf Connections.* Charles W. Roeder, Robert Graff, Jennifer Soderstrom, and Jun Han Yoo. December 2001.

PEER 2002/06 *The Use of Benefit-Cost Analysis for Evaluation of Performance-Based Earthquake Engineering Decisions.* Richard O. Zerbe and Anthony Falit-Baiamonte. September 2001.

PEER 2002/05 *Guidelines, Specifications, and Seismic Performance Characterization of Nonstructural Building Components and Equipment*. André Filiatrault, Constantin Christopoulos, and Christopher Stearns. September 2001.

PEER 2002/04 *Consortium of Organizations for Strong-Motion Observation Systems and the Pacific Earthquake Engineering Research Center Lifelines Program: Invited Workshop on Archiving and Web Dissemination of Geotechnical Data, 4–5 October 2001*. September 2002.

PEER 2002/03 *Investigation of Sensitivity of Building Loss Estimates to Major Uncertain Variables for the Van Nuys Testbed.* Keith A. Porter, James L. Beck, and Rustem V. Shaikhutdinov. August 2002.

PEER 2002/02 *The Third U.S.-Japan Workshop on Performance-Based Earthquake Engineering Methodology for Reinforced Concrete Building Structures*. July 2002.

PEER 2002/01 *Nonstructural Loss Estimation: The UC Berkeley Case Study.* Mary C. Comerio and John C. Stallmeyer. December 2001.

PEER 2001/16 *Statistics of SDF-System Estimate of Roof Displacement for Pushover Analysis of Buildings.* Anil K. Chopra, Rakesh K. Goel, and Chatpan Chintanapakdee. December 2001.

PEER 2001/15 *Damage to Bridges during the 2001 Nisqually Earthquake.* R. Tyler Ranf, Marc O. Eberhard, and Michael P. Berry. November 2001.

PEER 2001/14 *Rocking Response of Equipment Anchored to a Base Foundation.* Nicos Makris and Cameron J. Black. September 2001.

PEER 2001/13 *Modeling Soil Liquefaction Hazards for Performance-Based Earthquake Engineering.* Steven L. Kramer and Ahmed-W. Elgamal. February 2001.

PEER 2001/12 *Development of Geotechnical Capabilities in OpenSees.* Boris Jeremi . September 2001.

PEER 2001/11 *Analytical and Experimental Study of Fiber-Reinforced Elastomeric Isolators*. James M. Kelly and Shakhzod M. Takhirov. September 2001.

PEER 2001/10 *Amplification Factors for Spectral Acceleration in Active Regions.* Jonathan P. Stewart, Andrew H. Liu, Yoojoong Choi, and Mehmet B. Baturay. December 2001.

PEER 2001/09 *Ground Motion Evaluation Procedures for Performance-Based Design.* Jonathan P. Stewart, Shyh-Jeng Chiou, Jonathan D. Bray, Robert W. Graves, Paul G. Somerville, and Norman A. Abrahamson. September 2001.

PEER 2001/08 *Experimental and Computational Evaluation of Reinforced Concrete Bridge Beam-Column Connections for Seismic Performance*. Clay J. Naito, Jack P. Moehle, and Khalid M. Mosalam. November 2001.

PEER 2001/07 *The Rocking Spectrum and the Shortcomings of Design Guidelines.* Nicos Makris and Dimitrios Konstantinidis. August 2001.

PEER 2001/06 *Development of an Electrical Substation Equipment Performance Database for Evaluation of Equipment Fragilities*. Thalia Agnanos. April 1999.

PEER 2001/05 *Stiffness Analysis of Fiber-Reinforced Elastomeric Isolators.* Hsiang-Chuan Tsai and James M. Kelly. May 2001.

PEER 2001/04 *Organizational and Societal Considerations for Performance-Based Earthquake Engineering.* Peter J. May. April 2001.

PEER 2001/03 *A Modal Pushover Analysis Procedure to Estimate Seismic Demands for Buildings: Theory and Preliminary Evaluation.* Anil K. Chopra and Rakesh K. Goel. January 2001.

PEER 2001/02 *Seismic Response Analysis of Highway Overcrossings Including Soil-Structure Interaction.* Jian Zhang and Nicos Makris. March 2001.

PEER 2001/01 *Experimental Study of Large Seismic Steel Beam-to-Column Connections.* Egor P. Popov and Shakhzod M. Takhirov. November 2000.

PEER 2000/10 *The Second U.S.-Japan Workshop on Performance-Based Earthquake Engineering Methodology for Reinforced Concrete Building Structures.* March 2000.

PEER 2000/09 *Structural Engineering Reconnaissance of the August 17, 1999 Earthquake: Kocaeli (Izmit), Turkey.* Halil Sezen, Kenneth J. Elwood, Andrew S. Whittaker, Khalid Mosalam, John J. Wallace, and John F. Stanton. December 2000.

PEER 2000/08 *Behavior of Reinforced Concrete Bridge Columns Having Varying Aspect Ratios and Varying Lengths of Confinement.* Anthony J. Calderone, Dawn E. Lehman, and Jack P. Moehle. January 2001.

PEER 2000/07 *Cover-Plate and Flange-Plate Reinforced Steel Moment-Resisting Connections.* Taejin Kim, Andrew S. Whittaker, Amir S. Gilani, Vitelmo V. Bertero, and Shakhzod M. Takhirov. September 2000.

PEER 2000/06 *Seismic Evaluation and Analysis of 230-kV Disconnect Switches.* Amir S. J. Gilani, Andrew S. Whittaker, Gregory L. Fenves, Chun-Hao Chen, Henry Ho, and Eric Fujisaki. July 2000.

PEER 2000/05 *Performance-Based Evaluation of Exterior Reinforced Concrete Building Joints for Seismic Excitation.* Chandra Clyde, Chris P. Pantelides, and Lawrence D. Reaveley. July 2000.

PEER 2000/04 *An Evaluation of Seismic Energy Demand: An Attenuation Approach.* Chung-Che Chou and Chia-Ming Uang. July 1999.

PEER 2000/03 *Framing Earthquake Retrofitting Decisions: The Case of Hillside Homes in Los Angeles.* Detlof von Winterfeldt, Nels Roselund, and Alicia Kitsuse. March 2000.

PEER 2000/02 *U.S.-Japan Workshop on the Effects of Near-Field Earthquake Shaking.* Andrew Whittaker, ed. July 2000.

PEER 2000/01 *Further Studies on Seismic Interaction in Interconnected Electrical Substation Equipment.* Armen Der Kiureghian, Kee-Jeung Hong, and Jerome L. Sackman. November 1999.

PEER 1999/14 *Seismic Evaluation and Retrofit of 230-kV Porcelain Transformer Bushings*. Amir S. Gilani, Andrew S. Whittaker, Gregory L. Fenves, and Eric Fujisaki. December 1999.

PEER 1999/13 *Building Vulnerability Studies: Modeling and Evaluation of Tilt-up and Steel Reinforced Concrete Buildings.* John W. Wallace, Jonathan P. Stewart, and Andrew S. Whittaker, editors. December 1999.

PEER 1999/12 *Rehabilitation of Nonductile RC Frame Building Using Encasement Plates and Energy-Dissipating Devices.* Mehrdad Sasani, Vitelmo V. Bertero, James C. Anderson. December 1999.

PEER 1999/11 *Performance Evaluation Database for Concrete Bridge Components and Systems under Simulated Seismic Loads.* Yael D. Hose and Frieder Seible. November 1999.

PEER 1999/10 *U.S.-Japan Workshop on Performance-Based Earthquake Engineering Methodology for Reinforced Concrete Building Structures.* December 1999.

PEER 1999/09 *Performance Improvement of Long Period Building Structures Subjected to Severe Pulse-Type Ground Motions*. James C. Anderson, Vitelmo V. Bertero, and Raul Bertero. October 1999.

PEER 1999/08 *Envelopes for Seismic Response Vectors.* Charles Menun and Armen Der Kiureghian. July 1999.

PEER 1999/07 *Documentation of Strengths and Weaknesses of Current Computer Analysis Methods for Seismic Performance of Reinforced Concrete Members.* William F. Cofer. November 1999.

PEER 1999/06 *Rocking Response and Overturning of Anchored Equipment under Seismic Excitations.* Nicos Makris and Jian Zhang. November 1999.

PEER 1999/05 *Seismic Evaluation of 550 kV Porcelain Transformer Bushings.* Amir S. Gilani, Andrew S. Whittaker, Gregory L. Fenves, and Eric Fujisaki. October 1999.

PEER 1999/04 *Adoption and Enforcement of Earthquake Risk-Reduction Measures.* Peter J. May, Raymond J. Burby, T. Jens Feeley, and Robert Wood.

PEER 1999/03 *Task 3 Characterization of Site Response General Site Categories*. Adrian Rodriguez-Marek, Jonathan D. Bray, and Norman Abrahamson. February 1999.

PEER 1999/02 *Capacity-Demand-Diagram Methods for Estimating Seismic Deformation of Inelastic Structures: SDF Systems*. Anil K. Chopra and Rakesh Goel. April 1999.

PEER 1999/01 *Interaction in Interconnected Electrical Substation Equipment Subjected to Earthquake Ground Motions.* Armen Der Kiureghian, Jerome L. Sackman, and Kee-Jeung Hong. February 1999.

PEER 1998/08 *Behavior and Failure Analysis of a Multiple-Frame Highway Bridge in the 1994 Northridge Earthquake.* Gregory L. Fenves and Michael Ellery. December 1998.

PEER 1998/07 *Empirical Evaluation of Inertial Soil-Structure Interaction Effects.* Jonathan P. Stewart, Raymond B. Seed, and Gregory L. Fenves. November 1998.

PEER 1998/06 *Effect of Damping Mechanisms on the Response of Seismic Isolated Structures.* Nicos Makris and Shih-Po Chang. November 1998.

PEER 1998/05 *Rocking Response and Overturning of Equipment under Horizontal Pulse-Type Motions.* Nicos Makris and Yiannis Roussos. October 1998.

PEER 1998/04 *Pacific Earthquake Engineering Research Invitational Workshop Proceedings, May 14–15, 1998: Defining the Links between Planning, Policy Analysis, Economics and Earthquake Engineering.* Mary Comerio and Peter Gordon. September 1998.

PEER 1998/03 *Repair/Upgrade Procedures for Welded Beam to Column Connections.* James C. Anderson and Xiaojing Duan. May 1998.

PEER 1998/02 *Seismic Evaluation of 196 kV Porcelain Transformer Bushings.* Amir S. Gilani, Juan W. Chavez, Gregory L. Fenves, and Andrew S. Whittaker. May 1998.

PEER 1998/01 *Seismic Performance of Well-Confined Concrete Bridge Columns.* Dawn E. Lehman and Jack P. Moehle. December 2000.

ONLINE REPORTS

The following PEER reports are available by Internet only at http://peer.berkeley.edu/publications/peer_reports.html

PEER 2009/107 *Experimental and Computational Evaluation of Current and Innovative In-Span Hinge Details in Reinforced Concrete Box-Girder Bridges: Part 2: Post-Test Analysis and Design Recommendations.* Matias A. Hube and Khalid M. Mosalam. December 2009.

PEER 2009/106 *Shear Strength Models of Exterior Beam-Column Joints without Transverse Reinforcement.* Sangjoon Park and Khalid M. Mosalam. November 2009.

PEER 2009/105 *Reduced Uncertainty of Ground Motion Prediction Equations through Bayesian Variance Analysis.* Robb Eric S. Moss. November 2009.

PEER 2009/104 *Advanced Implementation of Hybrid Simulation.* Andreas H. Schellenberg, Stephen A. Mahin, Gregory L. Fenves. November 2009.

PEER 2009/103 *Performance Evaluation of Innovative Steel Braced Frames.* T. Y. Yang, Jack P. Moehle, and Božidar Stojadinović. August 2009.

PEER 2009/102 *Reinvestigation of Liquefaction and Nonliquefaction Case Histories from the 1976 Tangshan Earthquake.* Robb Eric Moss, Robert E. Kayen, Liyuan Tong, Songyu Liu, Guojun Cai, and Jiaer Wu. August 2009.

PEER 2009/101 *Report of the First Joint Planning Meeting for the Second Phase of NEES/E-Defense Collaborative Research on Earthquake Engineering.* Stephen A. Mahin et al. July 2009.

PEER 2008/104 *Experimental and Analytical Study of the Seismic Performance of Retaining Structures.* Linda Al Atik and Nicholas Sitar. January 2009.

PEER 2008/103 *Experimental and Computational Evaluation of Current and Innovative In-Span Hinge Details in Reinforced Concrete Box-Girder Bridges. Part 1: Experimental Findings and Pre-Test Analysis.* Matias A. Hube and Khalid M. Mosalam. January 2009.

PEER 2008/102 *Modeling of Unreinforced Masonry Infill Walls Considering In-Plane and Out-of-Plane Interaction.* Stephen Kadysiewski and Khalid M. Mosalam. January 2009.

PEER 2008/101 *Seismic Performance Objectives for Tall Buildings.* William T. Holmes, Charles Kircher, William Petak, and Nabih Youssef. August 2008.

PEER 2007/101 *Generalized Hybrid Simulation Framework for Structural Systems Subjected to Seismic Loading.* Tarek Elkhoraibi and Khalid M. Mosalam. July 2007.

PEER 2007/100 *Seismic Evaluation of Reinforced Concrete Buildings Including Effects of Masonry Infill Walls.* Alidad Hashemi and Khalid M. Mosalam. July 2007.